

Alma Mater Studiorum – Università di Bologna

DOTTORATO DI RICERCA IN  
CHIMICA

Ciclo XXVII

**Settore Concorsuale di afferenza:** 03/B1

**Settore Scientifico disciplinare:** CHIM 03/B

**Biomimetic Scaffolds for the Controlled Release of Bioactive  
Molecules for Tissue Engineering Applications**

**Presentata da:** Dott.ssa Silvia Minardi

**Coordinatore Dottorato**

**Prof. Aldo Roda**

**Relatore**

**Prof. Norberto Roveri**

**Co-Relatori**

**Dott.sa Anna Tampieri**

**Dott. Ennio Tasciotti**

**Prof.sa Simona Fermani**

**Esame finale anno 2015**



# ACKNOWLEDGMENTS

I would like to thank all of the people that have helped me reach this important goal. These years have been decisive both from a career and personal stand point and I would have never made it without the support of my advisors and colleagues. Firstly, I would like to thank Dr. Anna Tampieri, who trained me since the early stage of my undergraduate studies. She encouraged me to pursue research as a profession and she believed in me, offering me great opportunities for growth and professional development. I would also like to thank all of my colleagues at the Institute of Science and Technology for Ceramics for their help and support, and in particular Dr. Monica Sandri. She has been a great mentor for all these years. I thank Director, Dr. Alida Bellosi for her support and for her appreciation of my work and accomplishments. Secondly, I would like to thank Dr. Ennio Tasciotti and Dr. Mauro Ferrari for mentoring, supporting and most importantly for also believing in me and my potential. They helped me reach my best, by demanding the maximum from myself and by pushing my limits. They all contributed in making me become the researcher I am now. I also would like to thank Dr. Francesca Taraballi and Dr. Bruna Corradetti. They have been great mentors, colleagues and friends. They profoundly impacted my research and the way I look at the regenerative medicine field.

I will be never able to properly express with words how grateful I am to all of those who believed in me and offered me the opportunity to do research. I hope I was able to properly convey my gratitude not only in my words but in my actions, by putting all my efforts and dedication into what I have done these past years. Professionally, this has been my most significant experience but I look forward to upcoming challenges.

# ABSTRACT

The temporospatial controlled delivery of growth factors is crucial to trigger the desired healing mechanisms in target tissues. The uncontrolled release of growth factors has been demonstrated to cause severe side effects in its surrounding tissues. Thus, the first working hypothesis was to tune and optimize a newly developed multiscale delivery platform based on a nanostructured silicon particle core (pSi) and a poly (dl-lactide-co-glycolide) acid (PLGA) outer shell. Both components of the resulting composite microspheres (PLGA-pSi) contributed to control the release kinetics of proteins. In a murine subcutaneous model, the platform was demonstrated to be fully tunable for the temporal and spatial control release of the payload. PLGA-pSi was able to retain the payload for weeks, thus avoiding the initial burst release found in most of the current drug delivery systems.

The ideal scaffold for regenerative medicine should concurrently mimic the structure of the original tissue from the nanoscale up to the macroscale and recapitulate the biochemical composition of the extracellular matrix (ECM) in space and time. Thus, a multiscale approach was followed in a multicompartiment collagen scaffold, to selectively integrate different sets of PLGA-pSi loaded with reporter proteins. Through the preservation of the structural cues of the functionalized collagen scaffold at the nanoscale and microscale, its macroscopic features (pore size, porosity, and swelling) were not altered. Additionally, the spatial confinement of the microspheres allowed the release of the reporter proteins in each of the layers of the scaffold. Finally, the staged and zero-order release kinetics enabled the temporal biochemical patterning of the scaffold. The versatile manufacturing of each component of the scaffold resulted in the ability to customize it to better mimic the architecture and composition of the tissues and biological systems.

However, the clearance of delivery systems from implants is currently a limiting step in the development of biomaterials functionalized with delivery systems for tissue engineering applications. Thus, the last step of this PhD project was to test if by fully embedding PLGA microspheres in a highly structured and fibrous collagen-based scaffold (camouflaging), it was possible to prevent their early detection and clearance by macrophages. It was further studied whether such a camouflaging strategy was efficient in reducing the production of key inflammatory molecules, while preserving the release kinetics of the payload of the PLGA microspheres. Results demonstrated that the camouflaging allowed for a 10-fold decrease in the number of PLGA microspheres internalized by macrophages, suggesting that the 3D scaffold operated by cloaking the PLGA microspheres. When the production of key inflammatory cytokines induced by the scaffold was assessed, macrophages' response to the PLGA microspheres-integrated scaffolds resulted in a response similar to that observed in the control (not functionalized scaffold) and the release kinetic of a reporter protein was preserved. This data suggested that the platform herein proposed is an efficient system to camouflage delivery systems in 3D collagen-based scaffolds, preventing their early detection and internalization by macrophages, thus contributing to preserve the release kinetics of their payload.

In summary, this PhD thesis consisted of the development of 3D biomimetic scaffolds integrated with nanostructured carriers of bioactive molecules, able to escape early macrophage response, ultimately allowing for the spatial and temporal control over the release kinetics of their payload, for tissue engineering applications.

# CONTENTS

## 1. INTRODUCTION

- 1.1. Mimicry of the extracellular matrix composition and its functions
- 1.2. The extracellular matrix: a modulator of cell activity in tissues
- 1.3. Artificial extracellular matrices for tissue engineering applications
- 1.4. Surface modifications of biomaterials
  - 1.4.1. Integrin adhesion sites
  - 1.4.2. Growth factors
  - 1.4.3. Molecules and artificial ECM: new players in immune-modulation
- 1.5. Biomimicry of the biochemical gradients occurring in the regenerative process
- 1.6. Control over growth factor release
  - 1.6.1. Polymeric vectors
  - 1.6.2. Silica-based vectors
  - 1.6.3. Composite vectors
- 1.7. References

## 2. ANALYTICAL METHODS

- 2.1. Microscopy
  - 2.1.1. Scanning electron microscopy (SEM)
    - 2.1.1.1. Detection of secondary electrons
    - 2.1.1.2. Resolution of the SEM
  - 2.1.2. Fluorescence microscopy
    - 2.1.2.1. Principles of Fluorescence
    - 2.1.2.2. Excitation and emission
    - 2.1.2.3. Fluorophores
    - 2.1.2.4. Fluorescence microscope
    - 2.1.2.5. Confocal laser microscope
- 2.2. Physical-chemical techniques
  - 2.2.1. Fourier transform infrared spectroscopy (FTIR)
  - 2.2.2. Inductively coupled plasma (ICP)
  - 2.2.3. Thermo-gravimetric Analysis (TGA)
- 2.3. Biomolecular techniques
  - 2.3.1. Principles of the Flow Cytometry
  - 2.3.2. RNA extraction and quantitative polymerase chain reaction (RT-PCR)
- 2.4. References

## 3. COMPOSITE NANOSTRUCTURED CARRIERS FOR BIOACTIVE MOLECULES

- 3.1. Introduction
- 3.2. Materials and methods
- 3.3. Results and Discussion
- 3.4. Conclusions
- 3.5. References

#### 4. MULTISCALE PATTERNING OF BIOMIMETIC SCAFFOLDS

4.1. Introduction

4.2. Materials and methods

4.3. Results and Discussion

4.4. Conclusions

4.5. References

#### 5. CAMOUFLAGING OF DELIVERY SYSTEMS IN 3D BIOMIMETIC SCAFFOLDS

5.1. Introduction

5.2. Materials and methods

5.3. Results

5.4. Discussion

5.5. Conclusions

5.6. References

#### 6. CONCLUSIONS

## CHAPTER 1

# INTRODUCTION

Tissue engineering allows restoring or favoring the recovery of damaged tissues and organs, and it has been envisioned the possibility to reduce the need for organ replacement [1]. Even though fewer than five engineered tissues have been approved by the Food and Drug Administration (FDA), more than 70 companies are spending a total of \$600 million per year to develop new products (2). There are still many technical challenges to overcome before we create “off-the-shelf” tissues that represent the translation of scientific discoveries into treatments for millions of patients. The successful large-scale production of engineered tissues requires an adequate source of healthy expandable cells, the optimization of scaffolds, and the creation of bioreactors, which mimic the environment of the body and that are amenable to scale-up. Additional challenges include the preservation of the product so that it has a long shelf-life and the successful use of various approaches to prevent tissue rejection [1].

Innovative regenerative approaches and devices can be designed by taking inspiration from nature, which surrounds us with a multitude of organisms endowed with extraordinary performances. The shape of organisms, animal coat patterns and seashells are becoming more often an inspiring source. Material scientists have been vastly learning from Nature; for example structures found on water lilies, on butterfly wings or marine organism’s skeleton could find application to construct water-repellant materials, photonic structures or optical fibers [2]. Moreover, biomaterials found in nature not only have very interesting properties but are also inspiring in the way they are made.

Biomimicry is a term used to describe different kinds of therapeutic/biomedical approaches: mimicking nature form or function, organization and biomolecular working mechanism are just a few examples of this new research field [3]. Mimicking nature’s form or function can be applied as a paradigm in the tissue engineering applications.

### **1.1. Mimicry of the extracellular matrix composition and its functions**

The final goal of tissue engineering is to create neo-tissues similar in architecture, function and compatibility to native human structures [4]. Although this approach is very promising, many challenges have to be addressed to achieve effective tissue regeneration through the reproduction of complex mechanisms of living system [5]. Observation and understanding of the fundamentals operating in native tissue represents the starting point to develop biohybrid artificial substitutes. Inside a tissue, cells of different phenotypes are interconnected by a complex network of macromolecules comprising of proteins and polysaccharides secreted by the cells themselves. This natural environment refers to the extracellular matrix (ECM) that has the role to structurally and functionally organize the overall tissue.

### **1.2. The extracellular matrix: a modulator of cell activity in tissues**

The ECM serves as a channel for cell-cell communication. It is enriched with a number of cell surface receptors (e.g. integrins, laminin, syndecans) and structural proteins (e.g. collagens, laminins, fibronectin, vitronectin and elastin, which allow adhesion, migration, proliferation and differentiation [6]. Artificial two- and three-dimensional extracellular scaffolds are typically employed by tissue-engineering to reproduce a native functional tissue and thereby improve the recovery of the patient and tissue regeneration [7]. Such an artificial environment, meant to support different processes in tissue formation, the ECM should ideally: *i*) provide structural support for cells residing in that tissue to attach, grow, migrate and respond to signals; *ii*) give the tissue its structural and mechanical properties associated with the tissue functions; *iii*) provide bioactive cues to the residing cells; *iv*) act as a reservoir of growth factors

(GF); v) provide a degradable environment to allow neovascularization and remodeling in response to developmental, physiological and pathological challenges (e.g., homeostasis and wound healing) [8]. Because of the tight connection between the cytoskeleton and the ECM achieved through cell surface receptors, cells sense and respond to the mechanical properties of their environment by converting mechanical signals into chemical signals [9, 10]. Consequently, the biophysical properties of ECM influence various cell functions, including adhesion and migration. Moreover, the fibrillar structure of matrix components have been demonstrated to alter cell behavior by bringing about adhesion ligand clustering [11]. Structural ECM features, such as fibrils and pores, are often of a size compatible with cellular processes involved in migration, which may influence the strategy by which cells migrate through the ECM [12].

### 1.3. Artificial extracellular matrices for tissue engineering applications

The principles of biomimicry are based on strict adherence to the proper replication of natural science as a medium for promoting cellular repair. This coupled with control over the chemical and physical cues of the scaffold will provide the proper environment for cells to integrate and proliferate with the surrounding recipient tissue site. Demonstrating control over the platform for cell growth is important to achieving multi-functionality [13]. In order to create an artificial extracellular matrix a wide range of options exist (natural, synthetic and hybrid materials).

- *Natural materials* have biological activity and biocompatibility. The degradation products of these kinds of materials are natural metabolic products as sugars, aminoacids or minerals that reduce the possibility of cytotoxicity and inflammation [14]. They can be grouped in 3 classes: i) ceramics and ceramics composites (shells, bones, material with mineral component) ii) biopolymer and biopolymer composit (ligament and silk) iii) cellular materials (feathers, wood, cancellous bone).
- *Biomimetic Synthetic materials* represent biologically multifunctional hydrogel-based structures, synthesized or not under physiological-like conditions [15, 16], that mimic natural ECMs at the biochemical and biophysical level such as poly( $\epsilon$ -caprolacton (PCL), poly(lactic-co-glycolic) acid (PGLA), and Polyethylene glycol (PEG).
- *Hybrid materials* are systems composed by at least two distinct classes of material (synthetic and biological), for example, synthetic polymers and proteins domains. The combination results in new materials that possess novel properties [17].

Although natural biomaterials have proved effective in many basic and clinical applications [18] synthetic materials more effectively control their physical and chemical properties and can be further modified through biochemical means [19].

### 1.4. Surface modifications of biomaterials

For the successful design of materials to serve as artificial ECMs, knowledge of molecular interactions that occur within the tissues and between the cells and the ECM is required [20-22] (Figure 1.1). The composition, structure, and manufacturing methods could affect the structural and mechanical properties of the tailored scaffold and the *in vivo* degradation [23]. Attempts to determine synthetic material surface modifications and to improve the modulation of cell-material interactions have led to the alteration of physicochemical features of biomaterials like chemistry [24] or topography [25-27]. Current methods of biomaterial functionalization include specific surface coatings and the incorporation of bioactive molecules such as adhesion sites, growth factors, anti-inflammatory mediators or drugs, either alone or combined [28, 29]. Biomaterial surface functionalization can be performed either by physical or by wet chemical treatments. Physical modifications include electron-beam or UV-radiation-induced coupling of molecules [8] [6], surface-radical-induced coupling of molecules, and functionalization by non-polymerizing plasma-generated species. Each of these approaches has specific advantages and disadvantages concerning the variability, selectivity, and stability of the obtained functionalization, as well as the question of polymer structure retention or destruction. At present, most functionalization approaches result in surfaces that exhibit a mix of different functional groups [9-13]. It is notable that

plasma activation offers a convenient way to alter the surface properties, such as bioactivity and hydrophilicity, or hydrophobicity, while retaining the favorable bulk properties such as biostability, or biodegradability [14, 19].

Taking into account the multifunctional and the nature of biological components, the major challenge into this direction is a chemical one: the need to proceed through bio-orthogonal reactions and under the benign reaction conditions that would preserve and respect the functionality and structure of biological building blocks. In 2001, Sharpless and coworkers [17] introduced the concept of “click chemistry” that

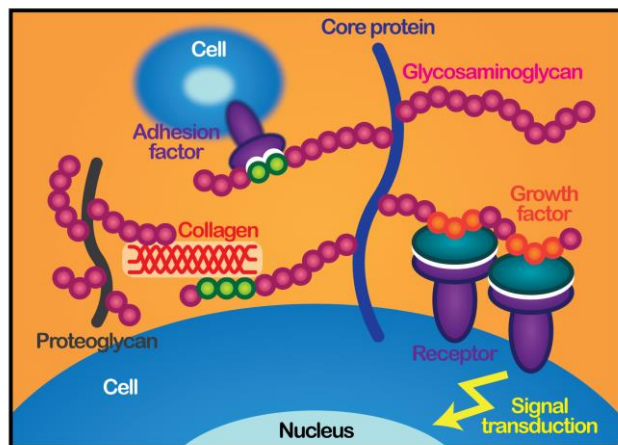


**Figure 1.1 – Schematic of the interaction between the extra cellular matrix and cells.**

successively had an wide impact on the chemical community driving the design of new generation of synthetic biomaterials [30]. These versatile reactions represent a formidable way to engineer hydrogel networks, decorated 2D cell culture surfaces and 3D scaffold. It also provides control over the conformation of the protein or peptide immobilized, thereby maximizing its bioactivity. Finally, the evolution of click-chemistry with the Diels–Alder Click Immobilization is the new era of “reagent-free” click reaction that does not require catalyst, photoinitiator, or radical initiation [31-33].

#### 1.4.1. Integrin adhesion sites

The knowledge of cell adhesion molecules (CAMs) is already being widely investigated [34].

Integrins are proteins known to be involved in the process of cell adhesion, motility, growth, shape and differentiation [35]. The functionalization of biomaterials with short sequences derived from ECM proteins has been shown to improve cell-specific adhesion and function. The most commonly used peptides are derived from proteins like fibronectin (e.g. RGD, KQAGDV, REDV and PHSRN), laminin (e.g. IKLLI, LRE, LRGDN, PDGSR, IKVAV, LGTIPG, and YIGSR), collagen (e.g. DGEA, GFOGER) and elastin (e.g. VAPG). The most widely used is the arginine-glycine-aspartate (RGD) sequence, a ubiquitous receptor adhesion motif found in most ECM proteins [30]. RGD modified surfaces have been used in a variety of applications such as engineering neuronal tissue [36], improving human embryonic stem cells growth in vitro [30] and increasing the biocompatibility of orthopedic materials [37]. Regarding the integrin domain functionalization some key aspects need to be taken into account. The density and *presentation* of these peptides have been reported to highly affect the overall cellular functions [38, 39] such as cell proliferation, gene expression and differentiation [30]. This effect can be attributed to the variation in adhesion strength between the cells and the substrate. Moreover, spacer sequences (commonly polyethylene glycol) must be long enough, depending of the exposed signal in order) [40] to prevent steric hindrance and to allow for maximal receptor binding, but they must also be short enough to allow for synergistic interactions. The presence of spacers allows for the peptide to present to the cell in a more stable conformation and effectively interact with several receptors [41]. To avoid this limitation, some researchers have explored functionalization using recombinant fragments of native ECM proteins to maintain the native folding of the protein, to retain the same binding motif conformation and orientation and also to inhibit antigenicity.

#### 1.4.2. Growth factors

Cellular functions are not solely controllable by promoting adhesion and direct interaction with integrins and other cell surface receptors. The induction of a specific growth factor’s response is crucial to effectively modulating cell activity. Biodegradable coatings that locally release incorporated growth factors (i.e. Bone Morphogenic Protein-2 (BMP-2), IGF and TGF- $\beta$ ) have been successfully tested to stimulate fracture healing and to improve biomaterial performance [42]. However, emerging approaches have focused on controlling growth factor release kinetics in order to decrease the effective dose and

potential side effects [43]. Sponges [44], hydrogels [45], pastes [46, 47], putties, particulates and various micro- and nano- carriers [45] have been used to successfully deliver growth factors over long timescales. A more sophisticated approach is to exploit the potential of the ECM to regulate the release and functions of growth factors. Artificial ECMs have been developed by functionalizing collagen matrices with glycosaminoglycans (GAGs) and proteoglycans (PGs) [48] to produce a material able to recreate the in vivo environment.

#### 1.4.3. Molecules and artificial ECM: new players in immune-modulation

In tissue engineering biomaterial implantation is usually accompanied by the injury provoked by the surgical procedure. Tissue or organ injury initiates an inflammatory response to the biomaterial starting with the formation of a provisional matrix [31, 49]. The ability of the immune system to correctly resolve the entire wound healing phases is important in determining the final success of the implanted biomaterials. As such, another crucial role of the ECM is regulating and integrating different and consecutive key processes during the wound healing: hemostasis, inflammation, proliferation and remodeling of the injured tissue.

During hemostasis, platelets are activated by signals from damaged vascular tissue that induce clot formation. In this phase, there is a formation of a provisional matrix consisting of fibrin and entrapped erythrocytes [49]. Additionally, the secretion of chemokines initiates the recruitment of neutrophils, macrophages, fibroblasts, and resident cells [50]. During the early phases of inflammation, neutrophils are the first cells to be recruited and to arrive at the wound site. They start to phagocytose all the foreign material, bacteria, or dead cells around the wound site while secreting biomolecular cytokines to recruit macrophages. Pro-inflammatory macrophages (M1 phenotype) secrete cytokines and chemokines that promote the further recruitment of other leukocytes to the site of injury [51]. Macrophages then change to a more reparative phenotype (M2 phenotype, also called “alternatively activated”) in order to remove apoptotic neutrophils, thus leading to the resolution of the inflammatory phase [50, 52], and, ultimately, to the remodeling phase. The proliferation process involves cellular proliferation, angiogenesis, and new ECM deposition. These are largely mediated via cytokines secreted by macrophages, T lymphocytes, and other cells within the wound site [52]. Finally the remodeling phase is characterized by the degradation and remodeling of the newly deposited ECM, which is mediated by metalloproteinase (MMP) and tissue inhibitor of metalloproteinase (TIMP). This generally results in scar tissue formation or maturation [50-53].

In particular, the foreign body reaction (FBR), composed of macrophages and foreign body giant cells, has been shown to play a critical role in the successful performance of the artificial ECM and mediates the rejection of the implant [31]. For this particular event the biomaterials surface plays the most important role. In fact, in the very early process of implantation, blood/material interactions occur with protein adsorption to the biomaterial surface and development of a blood-based transient provisional matrix that forms on and around the biomaterial. On the contrary, the appropriate functionalization of the biomaterials to be implanted can help in inducing a newly described mechanism that switched macrophages from a detrimental (inflammatory, M1) to a beneficial (regenerative, M2) phenotype [32, 33]. This process, known as “macrophage polarization” can thereby influence macrophages consequent behavior, such as phagocytosis and cytokines secretion. Significant efforts have focused on modifying material properties using various anti-inflammatory polymeric surface coatings to generate more biocompatible implants. The specific features of any synthetic biomaterials are able to tune the formation of giant cells. These multinucleate macrophages can be found at biomaterial surfaces even years following implantation. Recent studies have demonstrated that altering the properties of the bulk materials it is possible to influence the preferential polarization of macrophages [54, 55]. Indeed, natural derived biomaterials elicit a different immune response due to their native structure and surface, as well as the presence of natural ligands that promote constructive tissue remodeling. This anabolic process has been directly linked to the ability of material to polarize macrophage phenotypes [56, 57]. This suggests that biomaterial design strategies able to control the macrophage phenotype may improve the regenerative medicine applications.

A better understanding of the context-specific biological mechanisms, which underlie the macrophage response and macrophage polarization, is essential for the development of biomimetic strategies for appropriate functional tissue remodeling responses.

Different strategies of coatings of anti-inflammatory molecules have been exploited in order to release drugs by passive mechanism [58-60] or by enzymatic secondary reaction [61-63]. As an example of passive mechanism, dexamethasone, a synthetic glucocorticoid hormone, has been used as an anti-inflammatory agent and has been shown to locally reduce the inflammation of the surrounding tissues [64, 65]. Another example of bio-inspired materials can be demonstrated by coating of superoxide dismutase (scavenger enzyme with anti-inflammatory properties) covalently attached to a polyethylene surface to reduce neutrophil recruitment [66]. To achieve the desired in vivo response appropriate coatings need to be designed.

Tunable, immune-modulatory materials may be able to actively direct cell behavior and activity surrounding the implant, thereby encouraging more desirable interactions.

### **1.5. Biomimicry of the biochemical gradients occurring in the regenerative process**

Several issues affect the therapeutic efficacy of GFs, including their short protein half-life in vivo, side-effects caused by the multiple or high doses administered to reach the desirable concentration in the cell, and possible denaturation of the protein during manipulation, and these should be carefully considered in the design of GF-based therapeutics [67]. Most therapeutic proteins (e.g. GFs, cytokines) that are administered in their native form and without any protection are susceptible to biodegradation, resulting in insufficient amounts of those proteins at the active site, or resulting in the generation of inactive variants [67]. In the search for methods that can overcome these disadvantages, encapsulation of a GF in a delivery system has been demonstrated to be very promising for GF-based therapeutics. This technology, known as localized delivery, is frequently the only feasible strategy if a locally controlled concentration of a GF is necessary, and it has found wide spread use in wound healing and tissue regeneration.

Nanomedicine has been offering numerous innovative possibilities also in this regenerative strategies [68]. However, of the diverse array of particles developed in laboratories, only a few have made their way to the clinic [69]. The ideal carrier for tissue engineering applications should be biocompatible, biodegradable, present a high surface area to accommodate a high amount of molecules and also modifiable to tune the release [67]. Herein, we have been focusing on the advances in molecules and protein release to create temporal and spatial patterns of molecules and GFs to mimic the biochemical gradients of the natural healing process.

### **1.6. Control over growth factor release**

The action of GFs is typically concentration dependent [70]. Thus, GFs release has to be precisely controlled. A plethora of nanostructured particulate technologies have been developed, aiming at delivering proteins [71], peptides [72], drugs [73], and genetic materials [74], in a controlled fashion in the site to be regenerated [68, 75, 76].

#### **1.6.1. Polymeric vectors**

Polymeric materials are frequently used to allow controlled, sustained, and localized delivery of proteins. Polymer delivery vehicles allow to control the kinetics and dose of protein release while also protecting the protein from degradation until release [68].

At the end of 1980s it was clear that tissue engineering could benefit of a controlled delivery of GFs and the number and complexity of delivery systems tremendously rose [77]. Several delivery systems prepared from gelatin and collagen were developed as implants [78]. Another material which has been greatly exploited is alginate, to synthesize beads ionically crosslinked [79, 80]. Furthermore, injectable gelatin microspheres were developed by the group of Tabata [81, 82]. In mid-1990s, research further focused on the design of new delivery systems based on biodegradable microspheres. In particular, polylactic acid and poly(lactic-co-glycolic acid) (PLA and PLGA) generated tremendous interest due to their excellent biocompatibility as well as the possibility to tailor their biodegradability by varying

composition (lactide/glycolide ratio) [83, 84], molecular weight and chemical structure (i.e. capped and uncapped end-groups) [77]. In particular, FDA approval of PLGA use in humans led to the availability of copolymers characterized by a wide range of *in vivo* life-times, ranging from 3 weeks to over 1 year [60]. Drug microencapsulation within PLGA copolymers, in form of micro- and nanoparticles, was regarded as a powerful mean to achieve sustained release for long time-frames and, in the case of labile molecules, such as proteins, effectively protect the molecule from *in vivo* degradation occurring at the administration site. Protein encapsulation in PLGA microspheres is a challenging task due to stability issues occurring during microsphere-processing, shelf-life and protein release [60]. Techniques to entrap protein in PLGA microspheres feature partly competing and partly complementary characteristics [85], and are all joined by the common aim of realizing experimental conditions as mild as possible. Fabrication methods actively used for physical encapsulation of growth factors include solvent casting and particulate leaching, freeze drying, phase separation, melt molding, phase emulsion, *in situ* polymerization and gas foaming [71]. A key issue is minimizing exposure of factors to harsh conditions during processing in order to protect the activity of the biomolecules [85].

Currently, the synthesis of PLGA follows well established protocols that provide the flexibility of producing PLGA particles with various size, shape, surface chemistry and also nanostructured enclosures [86, 87]. Moreover, PLGA is hydro-soluble, and not immunogenic. Some of these carriers have also the unique ability to co-encapsulate multiple molecules and control the release of each agent in a temporal fashion, or to trigger the release by responding to environmental changes, such as pH, temperature, light, and mechanical stress [6]. However, the preservation of proteins' stability during particles' fabrication still remains a concern.

#### 1.6.2. Silica-based vectors

A successful approach to preserve protein stability and at the same time allowing for an efficient protein loading has been proposed by De Rosa et al., who tested mesoporous silica particles (pSi) for high loading of proteins, and an agarose coating to further increase protein stability in the carrier [88]. pSi have been widely used for tissue engineering and drug delivery *in virtue* of its biodegradable and biocompatible nature [89, 90]. For therapeutic delivery, pSi has been administered orally [91], intravenously [92], or injected percutaneously and intraperitoneally in humans for brachytherapy without notable side effects [93]. A wide variety of therapeutic and imaging agents have been successfully loaded into and released from pSi particles including antibiotics [94], hormones [95], proteins [96], liposomes [17] and carbon nanotubes [97], showing the great versatility of this material as a delivery system. As a scaffold, pSi is suitable for directing the growth of neuronal cells [98] and for stimulating mineralization in bone tissue engineering [99, 100]. pSi structure and the idea of using it in nanotechnology applications came mimicking the structure of diatoms shell, which is characterized by a regular structure and high surface area [101, 102]. The size and shape as well as the porosity and pore size of the pSi particles can be engineered and tightly controlled during manufacturing [103], in order to provide a material with constant and uniform physical features at the micro- and nanometer scale and to control degradation time and kinetics as well as biodistribution and bioaccumulation [104, 105]. Additionally, their surface can be functionalized to be linked to scaffold or to control the release kinetics of the payload [88, 106]. Bovine serum albumin (BSA) and BMP-2 were also loaded into pSi particles to examine *in vitro* release kinetics of the proteins [106]. Furthermore, pSi itself has a regenerative potential: it is osteoinductive (it has the capacity to stimulate primitive stem cells or immature bone cells to grow and mature, forming healthy bone tissue) and also osteoconductive (it can serve as a scaffold on which bone cells can attach and grow so that the bone healing response is lead towards the graft site) [107]. The osteoconductivity of pSi can be controlled by altering the interfacial chemistry and micro-structure of the pores. The range of pore size and structure affords the identification of the preferred morphology for osteoblast adhesion, growth, protein matrix synthesis and mineralization.

Several coating strategies were also developed to avoid the burst release of proteins from the pores and to achieve a sustained and tunable release over the course of weeks [106, 108].

### 1.6.3. Composite vectors

The importance of GFs in the regulation of various cell processes, and the need to carefully regulate GF presentation, suggests that sophisticated approaches to their delivery will be crucial to affect desired cellular responses [109]. As discussed above, PLGA has been extensively used for its several advantages. However, PLGA release rates (as well as for pSi) are characterized by an initial burst release that partially hinders the ability to control the timed delivery of payloads [110, 111]. Also, the by-products of PLGA degradation decrease the pH of the surrounding micro-environment resulting in the inherent destabilization or denaturation of the protein payload [112]. In order to address these issues, Fan et al. introduced a composite delivery platform composed of a pSi core encapsulated in a PLGA shell (PLGA-pSi) [106]. The authors demonstrated that silicon nanoparticles had no immunogenic or toxic effects and that both the PLGA and the pSi component were fully biodegradable [113]. The use of pSi in combination with PLGA enabled the double controlled delivery of molecules, resulting in the extension of the therapeutic window and prevented the acidification of the system during the degradation process resulting in better stabilization of the payload and in a better *in vivo* therapeutic outcome [106, 114]. Compared with pSi, a larger quantity of biomolecules could be loaded and stored into the PLGA-pSi composite microparticles.

Recently, Bhattacharyya et al. also proposed a PEG-coated mesoporous silica nanoparticles (MSN) with incorporated trypsin inhibitor (a model protein molecule for growth factors) [115]. Due to the goal of incorporating large protein molecules the pore size of the as-synthesized MSNs was expanded by a hydrothermal treatment prior to payload incorporation. *In vitro* release from the MSNs without the thin polymer film shows an initial burst followed by continuous release. In the case of polymer-coated MSNs the initial burst release was completely suppressed and approximate zero order release was achieved for 4 weeks.

## 1.7. References

1. Griffith, L.G. and G. Naughton, *Tissue engineering--current challenges and expanding opportunities*. science, 2002. **295**(5557): p. 1009-1014.
2. Lopez, P.J., et al., *Mimicking biogenic silica nanostructures formation*. Current Nanoscience, 2005. **1**(1): p. 73-83.
3. Cramer, M., *Biomimicry: Innovation inspired by nature-Benyus, JM*, 1997, BOWKER MAGAZINE GROUP CAHNERS MAGAZINE DIVISION 249 W 17TH ST, NEW YORK, NY 10011.
4. Weber, B., et al. *Tissue engineering on matrix: future of autologous tissue replacement*. in *Seminars in immunopathology*. 2011. Springer.
5. Sreejalekshmi, K.G. and P.D. Nair, *Biomimeticity in tissue engineering scaffolds through synthetic peptide modifications—Altering chemistry for enhanced biological response*. Journal of Biomedical Materials Research Part A, 2011. **96**(2): p. 477-491.
6. Daley, W.P., S.B. Peters, and M. Larsen, *Extracellular matrix dynamics in development and regenerative medicine*. Journal of cell science, 2008. **121**(3): p. 255-264.
7. Bosman, F.T. and I. Stamenkovic, *Preface to extracellular matrix and disease*. The Journal of Pathology, 2003. **200**(4): p. 421-422.
8. Kim, B.-S. and D.J. Mooney, *Development of biocompatible synthetic extracellular matrices for tissue engineering*. Trends in biotechnology, 1998. **16**(5): p. 224-230.
9. Galbraith, C.G. and M.P. Sheetz, *Forces on adhesive contacts affect cell function*. Current opinion in cell biology, 1998. **10**(5): p. 566-571.
10. Geiger, B., et al., *Transmembrane crosstalk between the extracellular matrix and the cytoskeleton*. Nature Reviews Molecular Cell Biology, 2001. **2**(11): p. 793-805.
11. Maheshwari, G., et al., *Cell adhesion and motility depend on nanoscale RGD clustering*. Journal of cell science, 2000. **113**(10): p. 1677-1686.
12. Friedl, P., *Prespecification and plasticity: shifting mechanisms of cell migration*. Current opinion in cell biology, 2004. **16**(1): p. 14-23.
13. Hollister, S.J., *Scaffold design and manufacturing: from concept to clinic*. Advanced Materials, 2009. **21**(32-33): p. 3330-3342.
14. Wegst, U. and M. Ashby, *The mechanical efficiency of natural materials*. Philosophical Magazine, 2004. **84**(21): p. 2167-2186.
15. Nuttelman, C.R., et al., *Macromolecular monomers for the synthesis of hydrogel niches and their application in cell encapsulation and tissue engineering*. Progress in polymer science, 2008. **33**(2): p. 167-179.
16. Lutolf, M. and J. Hubbell, *Synthetic biomaterials as instructive extracellular microenvironments for morphogenesis in tissue engineering*. Nature Biotechnology, 2005. **23**(1): p. 47-55.
17. Kopeček, J. and J. Yang, *Smart Self-Assembled Hybrid Hydrogel Biomaterials*. Angewandte Chemie International Edition, 2012. **51**(30): p. 7396-7417.
18. Ha, T.L.B. and T.M. Quan, *Naturally Derived Biomaterials: Preparation and Application*. 2013.
19. Zhu, J., *Bioactive modification of poly (ethylene glycol) hydrogels for tissue engineering*. Biomaterials, 2010. **31**(17): p. 4639-4656.
20. Stevens, M.M. and J.H. George, *Exploring and engineering the cell surface interface*. Science, 2005. **310**(5751): p. 1135-1138.
21. Hynes, R.O., *Integrins: versatility, modulation, and signaling in cell adhesion*. Cell, 1992. **69**(1): p. 11-25.
22. Adams, J.C. and F.M. Watt, *Regulation of development and differentiation by the extracellular matrix*. DEVELOPMENT-CAMBRIDGE-, 1993. **117**: p. 1183-1183.
23. Badylak, S.F., D.O. Freytes, and T.W. Gilbert, *Extracellular matrix as a biological scaffold material: structure and function*. Acta biomaterialia, 2009. **5**(1): p. 1-13.
24. Scotchford, C.A., et al., *Protein adsorption and human osteoblast-like cell attachment and growth on alkythiol on gold self-assembled monolayers*. Journal of biomedical materials research, 2002. **59**(1): p. 84-99.
25. Chen, S., et al., *Characterization of topographical effects on macrophage behavior in a foreign body response model*. Biomaterials, 2010. **31**(13): p. 3479-3491.

26. Dalby, M., et al., *In vitro reaction of endothelial cells to polymer demixed nanotopography*. *Biomaterials*, 2002. **23**(14): p. 2945-2954.
27. Schulte, V.A., et al., *Surface topography induces fibroblast adhesion on intrinsically nonadhesive poly (ethylene glycol) substrates*. *Biomacromolecules*, 2009. **10**(10): p. 2795-2801.
28. Franz, S., et al., *Immune responses to implants—A review of the implications for the design of immunomodulatory biomaterials*. *Biomaterials*, 2011. **32**(28): p. 6692-6709.
29. Boonthekul, T. and D.J. Mooney, *Protein-based signaling systems in tissue engineering*. *Current opinion in biotechnology*, 2003. **14**(5): p. 559-565.
30. Rahmany, M.B. and M. Van Dyke, *Biomimetic approaches to modulate cellular adhesion in biomaterials: A review*. *Acta biomaterialia*, 2012.
31. Anderson, J.M., *Biological responses to materials*. *Annual Review of Materials Research*, 2001. **31**(1): p. 81-110.
32. Collier, T. and J. Anderson, *Protein and surface effects on monocyte and macrophage adhesion, maturation, and survival*. *Journal of biomedical materials research*, 2002. **60**(3): p. 487-496.
33. Shen, M., et al., *Effects of adsorbed proteins and surface chemistry on foreign body giant cell formation, tumor necrosis factor alpha release and procoagulant activity of monocytes*. *Journal of Biomedical Materials Research Part A*, 2004. **70**(4): p. 533-541.
34. Hynes, R.O. and Q. Zhao, *The evolution of cell adhesion*. *The Journal of cell biology*, 2000. **150**(2): p. F89-F96.
35. Siebers, M., et al., *Integrins as linker proteins between osteoblasts and bone replacing materials. A critical review*. *Biomaterials*, 2005. **26**(2): p. 137-146.
36. Subramanian, A., U.M. Krishnan, and S. Sethuraman, *Development of biomaterial scaffold for nerve tissue engineering: Biomaterial mediated neural regeneration*. *J Biomed Sci*, 2009. **16**(1): p. 108.
37. Navarro, M., et al., *Biomaterials in orthopaedics*. *Journal of the Royal Society Interface*, 2008. **5**(27): p. 1137-1158.
38. Massia, S. and J. Hubbell, *Human endothelial cell interactions with surface-coupled adhesion peptides on a nonadhesive glass substrate and two polymeric biomaterials*. *Journal of biomedical materials research*, 1991. **25**(2): p. 223-242.
39. Roberts, C., et al., *Using mixed self-assembled monolayers presenting RGD and (EG) 3OH groups to characterize long-term attachment of bovine capillary endothelial cells to surfaces*. *Journal of the American Chemical Society*, 1998. **120**(26): p. 6548-6555.
40. Schmidt, D.R. and W.J. Kao, *Monocyte activation in response to polyethylene glycol hydrogels grafted with RGD and PHSRN separated by interpositional spacers of various lengths*. *Journal of Biomedical Materials Research Part A*, 2007. **83**(3): p. 617-625.
41. Taraballi, F., et al., *Glycine-spacers influence functional motifs exposure and self-assembling propensity of functionalized substrates tailored for neural stem cell cultures*. *Frontiers in neuroengineering*, 2010. **3**.
42. Schmidmaier, G., et al., *Collective review: Bioactive implants coated with poly (D, L-lactide) and growth factors IGF-I, TGF- $\beta$ 1, or BMP-2 for stimulation of fracture healing*. *Journal of long-term effects of medical implants*, 2006. **16**(1).
43. Suárez-González, D., et al., *Controllable mineral coatings on PCL scaffolds as carriers for growth factor release*. *Biomaterials*, 2012. **33**(2): p. 713-721.
44. Takahashi, Y., M. Yamamoto, and Y. Tabata, *Enhanced osteoinduction by controlled release of bone morphogenetic protein-2 from biodegradable sponge composed of gelatin and  $\beta$ -tricalcium phosphate*. *Biomaterials*, 2005. **26**(23): p. 4856-4865.
45. Yamamoto, M., Y. Takahashi, and Y. Tabata, *Controlled release by biodegradable hydrogels enhances the ectopic bone formation of bone morphogenetic protein*. *Biomaterials*, 2003. **24**(24): p. 4375-4383.
46. Kempen, D.H., et al., *Retention of in vitro and in vivo BMP-2 bioactivities in sustained delivery vehicles for bone tissue engineering*. *Biomaterials*, 2008. **29**(22): p. 3245-3252.
47. Li, R., et al., *rhBMP-2 injected in a calcium phosphate paste ( $\alpha$ -BSM) accelerates healing in the rabbit ulnar osteotomy model*. *Journal of orthopaedic research*, 2003. **21**(6): p. 997-1004.
48. Rammelt, S., et al., *Coating of titanium implants with collagen, RGD peptide and chondroitin sulfate*. *Biomaterials*, 2006. **27**(32): p. 5561-5571.
49. Clark, R.A., *Fibrin and wound healing*. *Annals of the New York Academy of Sciences*, 2001. **936**(1): p. 355-367.
50. Werner, S. and R. Grose, *Regulation of wound healing by growth factors and cytokines*. *Physiological reviews*, 2003. **83**(3): p. 835-870.

51. Barrientos, S., et al., *Growth factors and cytokines in wound healing*. Wound Repair and Regeneration, 2008. **16**(5): p. 585-601.
52. Adamson, R., *Role of macrophages in normal wound healing: an overview*. J Wound Care, 2009. **18**(8): p. 349-351.
53. Mantovani, A., et al., *The chemokine system in diverse forms of macrophage activation and polarization*. Trends in immunology, 2004. **25**(12): p. 677-686.
54. Brown, B.N., et al., *Macrophage phenotype as a predictor of constructive remodeling following the implantation of biologically derived surgical mesh materials*. Acta biomaterialia, 2012. **8**(3): p. 978-987.
55. Bota, P., et al., *Biomaterial topography alters healing in vivo and monocyte/macrophage activation in vitro*. Journal of Biomedical Materials Research Part A, 2010. **95**(2): p. 649-657.
56. Badylak, S.F., et al., *Macrophage phenotype as a determinant of biologic scaffold remodeling*. Tissue Engineering Part A, 2008. **14**(11): p. 1835-1842.
57. Brown, B.N., et al., *Macrophage phenotype and remodeling outcomes in response to biologic scaffolds with and without a cellular component*. Biomaterials, 2009. **30**(8): p. 1482-1491.
58. Benkirane-Jessel, N., et al., *Control of Monocyte Morphology on and Response to Model Surfaces for Implants Equipped with Anti-Inflammatory Agent*. Advanced Materials, 2004. **16**(17): p. 1507-1511.
59. Schultz, P., et al., *Polyelectrolyte multilayers functionalized by a synthetic analogue of an anti-inflammatory peptide,  $\alpha$ -MSH, for coating a tracheal prosthesis*. Biomaterials, 2005. **26**(15): p. 2621-2630.
60. Anderson, J.M. and M.S. Shive, *Biodegradation and biocompatibility of PLA and PLGA microspheres*. Advanced drug delivery reviews, 1997. **28**(1): p. 5-24.
61. Lutolf, M.P., et al., *Cell-Responsive Synthetic Hydrogels*. Advanced Materials, 2003. **15**(11): p. 888-892.
62. Zisch, A.H., et al., *Cell-demanded release of VEGF from synthetic, biointeractive cell ingrowth matrices for vascularized tissue growth*. The FASEB journal, 2003. **17**(15): p. 2260-2262.
63. Bae, M., et al., *Metalloprotease-specific poly (ethylene glycol) methyl ether-peptide-doxorubicin conjugate for targeting anticancer drug delivery based on angiogenesis*. Drugs under experimental and clinical research, 2003. **29**(1): p. 15-24.
64. Norton, L., et al., *Vascular endothelial growth factor and dexamethasone release from nonfouling sensor coatings affect the foreign body response*. Journal of Biomedical Materials Research Part A, 2007. **81**(4): p. 858-869.
65. Patil, S.D., F. Papadimitrakopoulos, and D.J. Burgess, *Concurrent delivery of dexamethasone and VEGF for localized inflammation control and angiogenesis*. Journal of controlled release, 2007. **117**(1): p. 68-79.
66. Udipi, K., et al., *Modification of inflammatory response to implanted biomedical materials in vivo by surface bound superoxide dismutase mimics*. Journal of biomedical materials research, 2000. **51**(4): p. 549-560.
67. Balasubramanian, V., et al., *Protein delivery: from conventional drug delivery carriers to polymeric nanoreactors*. Expert opinion on drug delivery, 2010. **7**(1): p. 63-78.
68. Shi, J., et al., *Nanotechnology in drug delivery and tissue engineering: from discovery to applications*. Nano letters, 2010. **10**(9): p. 3223-3230.
69. Peer, D., et al., *Nanocarriers as an emerging platform for cancer therapy*. Nat. Nanotechnol., 2007. **2**(12): p. 751-60.
70. Tayalia, P. and D.J. Mooney, *Controlled growth factor delivery for tissue engineering*. Adv Mater, 2009. **21**(32-33): p. 3269-85.
71. Lee, K., E.A. Silva, and D.J. Mooney, *Growth factor delivery-based tissue engineering: general approaches and a review of recent developments*. Journal of The Royal Society Interface, 2011. **8**(55): p. 153-170.
72. Amidi, M., et al., *Chitosan-based delivery systems for protein therapeutics and antigens*. Advanced drug delivery reviews, 2010. **62**(1): p. 59-82.
73. Ranade, V.V. and J.B. Cannon, *Drug delivery systems*. 2011: CRC press.
74. Srinivas, R., S. Samanta, and A. Chaudhuri, *Cationic amphiphiles: promising carriers of genetic materials in gene therapy*. Chem. Soc. Rev., 2009. **38**(12): p. 3326-3338.
75. Grattoni, A., et al., *Nanotechnologies and regenerative medical approaches for space and terrestrial medicine*. Aviat Space Environ Med, 2012. **83**(11): p. 1025-36.
76. Malmsten, M., *Inorganic nanomaterials as delivery systems for proteins, peptides, DNA, and siRNA*. Current Opinion in Colloid & Interface Science, 2013.

77. Quaglia, F., *Bioinspired tissue engineering: the great promise of protein delivery technologies*. Int J Pharm, 2008. **364**(2): p. 281-97.
78. Buckley, A., et al., *Sustained release of epidermal growth factor accelerates wound repair*. Proceedings of the National Academy of Sciences, 1985. **82**(21): p. 7340-7344.
79. Downs, E.C., et al., *Calcium alginate beads as a slow-release system for delivering angiogenic molecules In Vivo and In Vitro*. Journal of cellular physiology, 1992. **152**(2): p. 422-429.
80. Lee, K.Y., et al., *Controlled growth factor release from synthetic extracellular matrices*. Nature, 2000. **408**(6815): p. 998-1000.
81. Tabata, Y. and Y. Ikada, *Vascularization effect of basic fibroblast growth factor released from gelatin hydrogels with different biodegradabilities*. Biomaterials, 1999. **20**(22): p. 2169-75.
82. Tabata, Y., et al., *Neovascularization effect of biodegradable gelatin microspheres incorporating basic fibroblast growth factor*. J Biomater Sci Polym Ed, 1999. **10**(1): p. 79-94.
83. Borselli, C., et al., *Bioactivation of collagen matrices through sustained VEGF release from PLGA microspheres*. Journal of Biomedical Materials Research Part A, 2010. **92A**(1): p. 94-102.
84. Ungaro, F., et al., *Microsphere-integrated collagen scaffolds for tissue engineering: Effect of microsphere formulation and scaffold properties on protein release kinetics*. Journal of Controlled Release, 2006. **113**(2): p. 128-136.
85. Freitas, S., H.P. Merkle, and B. Gander, *Microencapsulation by solvent extraction/evaporation: reviewing the state of the art of microsphere preparation process technology*. Journal of controlled release, 2005. **102**(2): p. 313-332.
86. Cheng, J., et al., *Formulation of functionalized PLGA-PEG nanoparticles for in vivo targeted drug delivery*. Biomaterials, 2007. **28**(5): p. 869-876.
87. Müller, M., et al., *Surface modification of PLGA microspheres*. Journal of Biomedical Materials Research Part A, 2003. **66A**(1): p. 55-61.
88. De Rosa, E., et al., *Agarose surface coating influences intracellular accumulation and enhances payload stability of a nano-delivery system*. Pharm Res, 2011. **28**(7): p. 1520-30.
89. Martinez, J.O., et al., *Evaluation of Cell Function Upon Nanovector Internalization*. Small, 2012.
90. Canham, L.T., *Bioactive Silicon Structure Fabrication Through Nanoetching Techniques* Advanced Materials, 1995. **7**: p. 1033-1037.
91. Canham, L.T., *Nanoscale semiconducting silicon as a nutritional food additive* Nanotechnology, 2007. **18**: p. 185704.
92. Martin, F.J., et al., *Acute Toxicity of Intravenously Administered Microfabricated Silicon Dioxide Drug Delivery Particles in Mice: Preliminary Findings*. Drugs in R&D, 2005. **6**(2): p. 71-81.
93. Anthony Soon-Whatt, G., et al., *A novel approach to brachytherapy in hepatocellular carcinoma using a phosphorous<sup>32</sup> (32P) brachytherapy delivery device—a first-in-man study*. International journal of radiation oncology, biology, physics, 2007. **67**(3): p. 786-792.
94. Murphy, M.B., et al., *A multifunctional nanostructured platform for localized sustained release of analgesics and antibiotics*. European Journal of Pain Supplements, 2011. **5**(S2): p. 423-432.
95. Foraker, A.B., et al., *Microfabricated Porous Silicon Particles Enhance Paracellular Delivery of Insulin Across Intestinal Caco-2 Cell Monolayers*. Pharmaceutical Research, 2003. **20**(1): p. 110-116.
96. Prestidge, C.A., et al., *Loading and release of a model protein from porous silicon powders*. physica status solidi (a), 2007. **204**(10): p. 3361-3366.
97. Tasciotti, E., et al., *Mesoporous silicon particles as a multistage delivery system for imaging and therapeutic applications*. Nat Nano, 2008. **3**(3): p. 151-157.
98. Mayne, A.H., et al., *Biologically Interfaced Porous Silicon Devices*. physica status solidi (a), 2000. **182**(1): p. 505-513.
99. Whitehead, M.A., et al., *High-Porosity Poly(ε-Caprolactone)/Mesoporous Silicon Scaffolds: Calcium Phosphate Deposition and Biological Response to Bone Precursor Cells*. Tissue Engineering Part A, 2008. **14**(1): p. 195-206.
100. Whitehead, M.A., et al., *Accelerated calcification in electrically conductive polymer composites comprised of poly(ε-caprolactone), polyaniline, and bioactive mesoporous silicon*. Journal of Biomedical Materials Research Part A, 2007. **83A**(1): p. 225-234.
101. Losic, D., J.G. Mitchell, and N.H. Voelcker, *Diatomaceous Lessons in Nanotechnology and Advanced Materials*. Advanced Materials, 2009. **21**(29): p. 2947-2958.
102. Vrieling, E.G., et al., *Diatom silicon biomineralization as an inspirational source of new approaches to silica production*. Journal of biotechnology, 1999. **70**(1-3): p. 39-51.

103. Decuzzi, P., et al., *Size and shape effects in the biodistribution of intravascularly injected particles*. Journal of Controlled Release, 2010. **141**(3): p. 320-327.
104. Chiappini, C., et al., *Tailored porous silicon microparticles: fabrication and properties*. ChemPhysChem, 2010. **11**(5): p. 1029-35.
105. Martinez, J.O., et al., *Short and long term, in vitro and in vivo correlations of cellular and tissue responses to mesoporous silicon nanovectors*. Small, 2013. **9**(9-10): p. 1722-33.
106. Fan, D., et al., *Mesoporous Silicon-PLGA Composite Microspheres for the Double Controlled Release of Biomolecules for Orthopedic Tissue Engineering*. Advanced Functional Materials, 2012. **22**(2): p. 282-293.
107. Sun, W., et al., *Porous silicon as a cell interface for bone tissue engineering*. physica status solidi (a), 2007. **204**(5): p. 1429-1433.
108. De Rosa, E., et al., *Agarose surface coating influences intracellular accumulation and enhances payload stability of a nano-delivery system*. Pharmaceutical research, 2011. **28**(7): p. 1520-1530.
109. Shi, J., et al., *Nanotechnology in drug delivery and tissue engineering: from discovery to applications*. Nano Lett, 2010. **10**(9): p. 3223-30.
110. Habraken, W.J.E.M., et al., *PLGA microsphere/calcium phosphate cement composites for tissue engineering: in vitro release and degradation characteristics*. Journal of Biomaterials Science, Polymer Edition, 2008. **19**(9): p. 1171-1188.
111. Allison, S.D., *Analysis of initial burst in PLGA microparticles*. Expert Opinion on Drug Delivery, 2008. **5**(6): p. 615-628.
112. van de Weert, M., W.E. Hennink, and W. Jiskoot, *Protein Instability in Poly(Lactic-co-Glycolic Acid) Microparticles*. Pharmaceutical Research, 2000. **17**(10): p. 1159-1167.
113. Park, J.-H., et al., *Biodegradable luminescent porous silicon nanoparticles for in vivo applications*. Nat Mater, 2009. **8**(4): p. 331-336.
114. Murphy, M., et al., *Multi-Composite Bioactive Osteogenic Sponges Featuring Mesenchymal Stem Cells, Platelet-Rich Plasma, Nanoporous Silicon Enclosures, and Peptide Amphiphiles for Rapid Bone Regeneration*. Journal of Functional Biomaterials, 2011. **2**(2): p. 39-66.
115. Bhattacharyya, S., H. Wang, and P. Ducheyne, *Polymer-coated mesoporous silica nanoparticles for the controlled release of macromolecules*. Acta Biomaterialia, 2012. **8**(9): p. 3429-3435.

# ANALITICAL METHODS

## 2.1. Microscopy

### 2.1.1. Scanning electron microscopy (SEM)

The scanning electron microscope (SEM) is a type of electron microscope that creates various images by focusing a high energy beam of electrons onto the surface of a sample and detecting signals from the interaction of the incident electrons with the sample's surface [1]. The type of signals gathered in a SEM vary and can include secondary electrons, characteristic x-rays, and back scattered electrons (Fig. 2.1) [2]. In a SEM, these signals come not only from the primary beam impinging upon the sample, but from other interactions within the sample near the surface. The SEM is capable of producing high-resolution images of a sample surface in its primary use mode, secondary electron imaging. Due to the manner in which this image is created, SEM images have great depth of field yielding a characteristic three-dimensional appearance useful for understanding the surface structure of a sample. This great depth of field and the wide range of magnifications are the most familiar imaging mode for specimens in the SEM. Characteristic x-rays are emitted when the primary beam causes the ejection of inner shell electrons from the sample and are used to tell the elemental composition of the sample. The back-scattered electrons emitted from the sample may be used alone to form an image or in conjunction with the characteristic x-rays as atomic number contrast clues to the elemental composition of the sample. In a typical SEM, thermo-ionic electrons are emitted from a tungsten cathode and are accelerated towards an anode (Fig. 2.2) [3]. Tungsten is used because it has the highest melting point and lowest vapour pressure of all metals, thereby allowing it to be heated for electron emission. The electron beam, which typically has an energy ranging from a few hundred eV to 100 keV, is focused by one or two condenser lenses into a beam with a very fine focal spot sized 0.4 nm to 5 nm. The beam passes through pairs of scanning coils or pairs of deflector plates in the electron optical column, typically in the objective lens, which deflect the beam horizontally and vertically so that it scans in a raster fashion over a rectangular area of the sample surface. When the primary electron beam interacts with the sample, the electrons lose energy by repeated scattering and absorption within a teardrop-shaped volume of the specimen known as the interaction volume, which extends from less than 100 nm to around 5  $\mu\text{m}$  into the surface. The size of the interaction volume depends on the electrons' landing energy, the atomic number of the specimen and the specimen's density. The energy exchange between the electron beam and the sample results in the emission of electrons and electromagnetic radiation, which can be detected to produce an image, as described below.

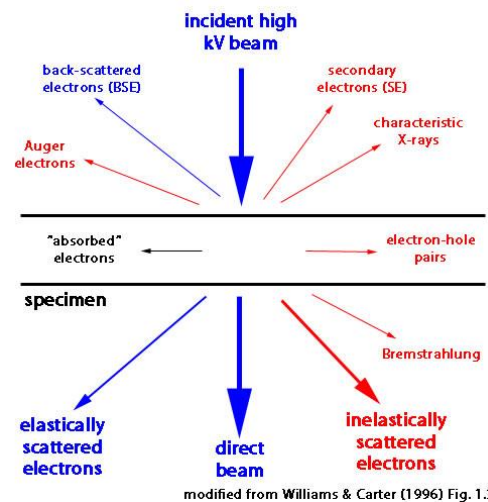


Figure 2.1 - Signals produced by the interaction of the electron beam with the sample.

#### 2.1.1.1. Detection of secondary electrons

The most common imaging mode monitors low energy (<50 eV) secondary electrons. Due to their low energy, these electrons originate within a few nanometers from the surface. The electrons are detected by a scintillator-photomultiplier device and the resulting signal is rendered into a two-dimensional intensity distribution that can be viewed and saved as a digital image. This process relies on a raster-scanned primary beam. The brightness of the signal depends on the number of secondary electrons reaching the detector. If the beam enters the sample perpendicular to the surface, then the activated region is uniform about the axis of the beam and a certain number of electrons "escape" from within the sample. As the angle of incidence increases, the "escape" distance of one side of the beam will decrease, and more secondary electrons will be emitted. Thus steep surfaces and edges tend to be brighter than flat surfaces, which results in images with a well-defined, three-dimensional appearance. Using this technique, resolutions less than 100 nm are possible.

#### 2.1.1.2. Resolution of the SEM

The spatial resolution of the SEM depends on the size of the electron spot, which in turn depends on both the wavelength of the electrons and the magnetic electron-optical system which produces the scanning beam. The resolution is also limited by the size of the interaction volume, or the extent to which the material interacts with the electron beam. The spot size and the interaction volume both might be large compared to the distances between atoms, so the resolution of the SEM is not high enough to image individual atoms, as is possible in the shorter wavelength (i.e. higher energy) transmission electron microscope (TEM). The SEM has compensating advantages, though, including the ability to image a comparatively large area of the specimen; the ability to image bulk materials (not just thin films or foils); and the variety of analytical modes available for measuring the composition and nature of the specimen. The equipment employed in this study was a FEI Quanta 400 ESEM FEG, FEI, Hillsboro, OR.

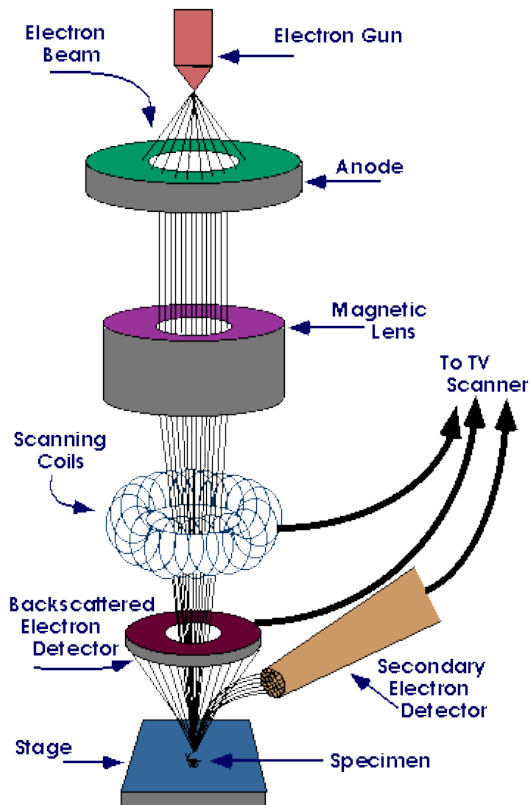


Figure 2.2 - Scheme of a Scanning Electron Microscope.

### 2.1.2. Fluorescence microscopy

#### 2.1.2.1. Principles of Fluorescence

The technique of fluorescence microscopy has become an essential tool in biology and the biomedical sciences, as well as in materials science due to attributes that are not readily available in other contrast modes with traditional optical microscopy. The application of an array of fluorochromes has made it possible to identify cells and sub-microscopic cellular components with a high degree of specificity amid non-fluorescing material. In fact, the fluorescence microscope is capable of revealing the presence of a single molecule. Through the use of multiple fluorescence labeling and different probes can simultaneously identify several target molecules simultaneously [4].

#### 2.1.2.2. Excitation and emission

Fluorescence microscopy requires that the objects of interest fluoresce, thus requires the use of fluorochromes, that are essentially dyes, which accept light energy (e.g. from a laser) at a given wavelength and re-emit it at a

longer wavelength. These two processes are called excitation and emission. Fluorescence is the emission of light that occurs within nanoseconds after the absorption of light that is typically of shorter wavelength.

In details, light is a form of electromagnetic energy that travels in waves. These waves have both frequency and length, the latter of which determines the color of light. The light that can be visualized by the human eye represents a narrow wavelength band (380–700 nm) between ultraviolet (UV) and infrared (IR) radiation. When light is absorbed by a fluorochrome, its electrons become excited and move from a resting state to a maximal energy level called the excited electronic singlet state. The amount of energy required will differ for each fluorochrome. This state only lasts for 1–10 nanoseconds because the fluorochrome undergoes internal conformational change and, in doing so, releases some of the absorbed energy as heat. The electrons subsequently fall to a lower, more stable, energy level called the relaxed electronic singlet state. As electrons steadily move back from here to their ground state they release the remaining energy (emission) as fluorescence. The difference between the exciting and emitted wavelengths, known as the Stokes shift, is the critical property that makes fluorescence so powerful [4, 5].

### 2.1.2.3. Fluorophores

Molecules that are used by virtue of their fluorescent properties are called fluorophores. Fluorochromes are stains that attach themselves to visible or sub-visible structures, are often highly specific in their attachment targeting. The outermost electron orbitals in the fluorophore molecule determine both its efficiency as a fluorescent compound and the wavelengths of absorption and emission. When fluorescent compounds in their so-called 'ground state' absorb light energy (photons), alterations in the electronic, vibrational and rotational states of the molecule can occur. The absorbed energy sometimes moves an electron into a different orbital that is on average farther away from the nucleus. Whereas many organic substances have intrinsic fluorescence (autofluorescence), and a few are useful for specific labeling of components in biological systems, the typical approach to fluorescence microscopy is to take advantage of synthesized compounds that have some degree of conjugated double bonds. Such compounds often have ring structures (aromatic molecules) with pi bonds that easily distribute outer orbital electrons over a wide area. In general, the more conjugated bonds in the molecule, the lower the excited energy requirement and the longer the wavelength (redder) the exciting light can be. The emitted light is shifted in the same direction [5].

### 2.1.2.4. Fluorescence microscope

The preferred illumination approach in modern fluorescence microscopes is epi-illumination. In this configuration the microscope objective not only has the familiar role of imaging and magnifying the specimen, but also serves as the condenser that illuminates it. The advantage of this approach over transmission, fluorescence microscopes (in which the exciting light comes through the condenser and the emission is collected by the objective) is that whereas the excitation of the fluorophore is equivalent in both epi- and transmitted microscopes, only the small percentage of the exciting light that is reflected off the sample needs to be blocked in the return light path in the epi-illumination mode. The main technical hurdle with this approach is that the exciting light and fluorescence emission overlap in the light path requiring a special kind of beam splitter, a dichroic mirror, to separate the excitation from the emission. The dichroic beam splitter mirror is designed to be used in light paths at 45°. In ordinary fluorescence microscopes, the dichroic reflects shorter wavelength light originating from the light source and transmits the longer wavelengths of the emitted fluorescence. Each dichroic is designed to have a transition from reflection to transmission that resides between the excitation and emission peaks of the fluorophore it is designed to be used with [5, 6].

There are several different strategies for fluorescence illumination. Traditionally the intensities needed for comfortable viewing by eye or rapid camera exposure come from arc lamps. Mercury and xenon arc lamps are expensive, potentially dangerous, and require special lamp houses and power supplies. These two types of arc lamps differ in several important ways. Depending on your requirements xenon or mercury is the better choice. Xenon has the advantage of being relatively even in the coverage of wavelengths throughout the UV, visible and near infrared. Mercury, however, is a spectrally peaky light source with several extremely intense lines [5]. An Eclipse Ti-U was used in this PhD project (NIKON).

#### 2.1.2.5. Confocal laser microscope

Confocal microscopy offers several advantages over conventional optical microscopy, including shallow depth of field, elimination of out-of-focus glare, and the ability to collect serial optical sections from thick specimens. In the biomedical sciences, a major application of confocal microscopy involves imaging either fixed or living cells and tissues that have usually been labeled with one or more fluorescent probes.

Confocal imaging involves serially scanning the specimen to create computer-generated optical sections down to 250 nm thickness using visible light. These optical sections may be stacked to provide a 3-D digital reconstruction of the specimen. Since the resolution possible in the laser scanning confocal microscope (LSCM) is somewhat better than in the conventional widefield optical microscope, but still considerably less than that of the transmission electron microscope, it has in some ways bridged the gap between the two more commonly used techniques [7].

In a conventional widefield microscope, the entire specimen is bathed in light from a mercury or xenon source, and the image can be viewed directly by eye or projected directly onto an image capture device or photographic film. In contrast, the method of image formation in a confocal microscope is fundamentally different. The illumination is achieved by scanning one or more focused beams of light, usually from a laser, across the specimen. The images produced by scanning the specimen in this way are called optical sections. This terminology refers to the noninvasive method by which the instrument collects images, using focused light rather than physical means to section the specimen. The confocal approach has facilitated much more useful imaging of living specimens, enabled the automated collection of three-dimensional (z-series) data, and improved the images obtained of specimens using multiple labeling [7].

The basic optics of the optical microscope have remained fundamentally unchanged for decades because the final resolution achieved by the instrument is governed by the wavelength of light, the objective lens, and the properties of the specimen itself. The dyes used to add contrast to specimens, and other technology associated with the methods of optical microscopy, have improved significantly over the past 20 years.

There are currently two alternative methods to confocal microscopy that are in use for producing optical sections: deconvolution and multiphoton imaging. They differ technically, but like confocal methods, are based on the conventional optical microscope. Deconvolution uses computer-based algorithms to calculate and remove out-of-focus information from fluorescence images. Due to more efficient algorithms and much faster mini computers, this technique has become a practical option for imaging. Multiphoton microscopy uses the same scanning system as the c, but does not require the pinhole aperture at the detector. The pinhole is unnecessary because the laser excites the fluorochrome label only at the point of focus, eliminating the out-of-focus emission. An additional benefit in the imaging of living tissues is that photobleaching is reduced in the specimen due to the reduced energy absorbed from the laser beam. The conventional optical microscope forms the basis around which the LSCM is built. Instead of a tungsten or mercury lamp, a laser is used as a light source, and is combined with a sensitive photomultiplier tube (PMT) detector, and a computer to control the scanning mirrors or other scanning devices and to facilitate the collection and display of images. Following acquisition the images are stored on digital media and may be analyzed by any of the numerous image processing software packages available using either the microscope system computer or a second computer [7]. In this study a Nikon A1 confocal laser microscope was used (NIKON).

## 2.2. Physical-chemical analysis

### 2.2.1. Fourier transform infrared spectroscopy (FTIR)

FTIR is the subset of spectroscopy that deals with the infrared region of the electromagnetic spectrum.

The infrared portion of the electromagnetic spectrum is divided into three regions; the near-, mid- and far-infrared, named for their relation to the visible spectrum. The far-infrared, approximately 400-10  $\text{cm}^{-1}$  (1000–30  $\mu\text{m}$ ), lying adjacent to the microwave region, has low energy and may be used for rotational spectroscopy. The mid-infrared, approximately 4000-400  $\text{cm}^{-1}$  (30–1.4  $\mu\text{m}$ ) may be used to study the fundamental vibrations and associated rotational-vibrational structure. The higher energy near-IR, approximately 14000-4000  $\text{cm}^{-1}$  (1.4–0.8  $\mu\text{m}$ ) can excite overtone or harmonic vibrations.

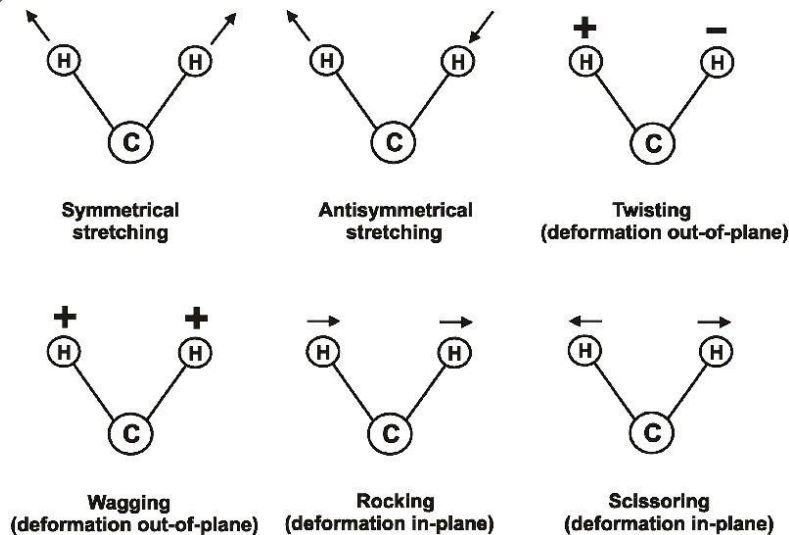


Figure 2.3 - Possible vibrations detected by infrared spectroscopy.

Infrared spectroscopy exploits the fact that molecules have specific frequencies at which they rotate or vibrate corresponding to discrete energy levels (Fig. 2.3) [8]. These resonant frequencies are determined by the shape of the molecular potential energy surfaces the masses of the atoms and, by the coupling of vibrational and electronic interactions in the molecule.

Thus, the resonant frequencies can be in a first approach related to the strength of the bond, and the mass of the atoms at either end of it. Thus, the frequency of the vibrations can be associated with a particular bond type and can be used for the characterization of very complex mixtures.

The infrared spectra of a sample is collected by passing a beam of infrared light through the sample. Examination of the transmitted light reveals how much energy was absorbed at each wavelength (see Fig. 2.4).

This can be done with a monochromatic beam, which changes in wavelength over time, or by using a Fourier transform instrument to measure all wavelengths at once. From this, a transmittance or absorbance spectrum can be produced, showing at which IR wavelengths the sample absorbs. Analysis of these absorption characteristics reveals details about the molecular structure of the sample. The method employed for sample preparation is to grind a quantity of the sample with potassium bromide finely (to remove scattering effects from large crystals), which is used also as a reference. This powder mixture is then crushed in a mechanical die press to form a translucent pellet through which the beam of the spectrometer can pass.

A reference is used for two reasons:

- This prevents fluctuations in the output of the source affecting the data;
- This allows the effects of the solvent to be cancelled out (the reference is usually pure solvent).

The equipment employed in the present work was a Thermo Nicolet-Avatar 320 FT-IR.

### 2.2.2. Inductively coupled plasma (ICP)

Inductively Coupled Plasma Optical Emission Spectrometry (ICP-OES) is a type of emission spectroscopy that uses a plasma (e.g. inductively coupled plasma) to produce excited atoms that emit electromagnetic radiation at a wavelength characteristic of a particular element. The intensity of the radiation is proportional to the concentration of the element, which is obtained through a previous calibration obtained with opportune standard solutions. An inductively coupled plasma (ICP) for spectrometry is sustained in a torch that consists of three concentric tubes, usually made of quartz. The end of this torch is placed inside an induction coil supplied with a radio-frequency electric current. A flow of argon gas is introduced between the two outermost tubes of the torch and an electrical spark is applied for a short time to introduce free electrons into the gas stream. These electrons

interact with the radio-frequency magnetic field of the induction coil and are accelerated first in one direction, then the other, as the field changes at high frequency. The accelerated electrons collide with argon atoms, and sometimes a collision causes an argon atom to part with one of its electrons. The released electron is in turn accelerated by the rapidly-changing magnetic field. The process continues until the rate of release of new electrons in collisions is balanced by the rate of recombination of electrons with argon ions (atoms that have lost an electron). This produces a ‘fireball’ that consists mostly of argon atoms with a rather small fraction of free electrons and argon ions. The samples to be analyzed are firstly solubilized and then introduced into the hot region through an atomizer. The temperature of the plasma is very high, of the order of 10,000 K,

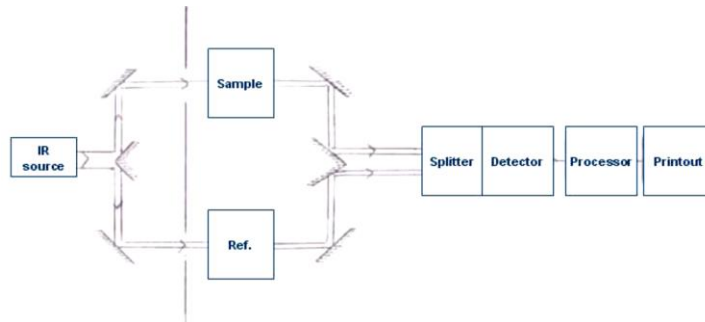


Figure 2.4 - Scheme of equipment for infrared spectroscopy.

### 2.2.3. Thermo-gravimetric Analysis (TGA)

Thermogravimetric Analysis or TGA is a type of testing that is performed on samples to determine changes in weight in relation to change in temperature. Such analysis relies on a high degree of precision in three measurements: weight, temperature, and temperature change. As many weight loss curves look similar, the weight loss curve may require transformation before results may be interpreted. A derivative weight loss curve can be used to tell the point at which weight loss is most apparent.

The analyzer usually consists of a high-precision balance with a pan loaded with the sample. The sample is placed in a small electrically heated oven with a thermocouple to accurately measure the temperature. The atmosphere may be purged with an inert gas to prevent oxidation or other undesired reactions. A computer is used to control the instrument. Analysis is carried out by raising the temperature gradually and plotting weight against temperature. After the data is obtained, curve smoothing and other operations may be done such as to find the exact points of inflection. A Q600 instrument was used in this study (TA instruments).

## **2.3. Biomolecular techniques**

### **2.3.1. Principles of the Flow Cytometry**

One of the fundamentals of flow cytometry is the ability to measure the properties of individual particles. When a sample in solution is injected into a flow cytometer, the particles are randomly distributed in three-dimensional space. The sample must therefore be ordered into a stream of single particles that can be interrogated by the detection system of the machine. This process is managed by the fluidics system. Essentially, the fluidics system consists of a central channel/core through which the sample is injected, enclosed by an outer sheath that contains faster flowing fluid. As the sheath fluid moves, it creates a massive drag effect on the narrowing central chamber. This alters the velocity of the central fluid whose flow front becomes parabolic with greatest velocity at its center and zero velocity at the wall. The effect creates a single file of particles and is called hydrodynamic focusing. Under optimal conditions (laminar flow) the fluid in the central chamber will not mix with the sheath fluid.

After hydrodynamic focusing, each particle passes through one or more beams of light. Light scattering or fluorescence emission (if the particle is labeled with a fluorochrome) provides information about the particle's properties. The laser and the arc lamp are the most commonly used light sources in modern flow cytometry.

Lasers produce a single wavelength of light (a laser line) at one or more discrete frequencies (coherent light). Arc lamps tend to be less expensive than lasers and exploit the color emissions of an ignited gas within a sealed tube. However, this produces unstable incoherent light of a mixture of wavelengths, which needs subsequent optical filtering. Light that is scattered in the forward direction, typically up to 20° offset from the laser beam's axis, is collected by a lens known as the forward scatter channel (FSC). The FSC intensity roughly equates to the particle's size and can also be used to distinguish between cellular debris and living cells. Light measured approximately at a 90° angle to the excitation line is called side scatter. The side scatter channel (SSC) provides information about the granular content within a particle. Both FSC and SSC are unique for every particle, and a combination of the two may be used to differentiate different cell types in a heterogeneous sample.

Fluorescence measurements taken at different wavelengths can provide quantitative and qualitative data about fluorochrome-labeled cell surface receptors or intracellular molecules such as DNA and cytokines. Flow cytometers use separate fluorescence (FL-) channels to detect light emitted. The number of detectors will vary according to the machine and its manufacturer. Detectors are either silicon photodiodes or photomultiplier tubes (PMTs).

The specificity of detection is controlled by optical filters, which block certain wavelengths while transmitting (passing) others. There are three major filter types. Long pass filters allow through light above a cut-off wavelength, short pass permit light below a cut-off wavelength and band pass transmit light within a specified narrow range of wavelengths (termed a band width). When a filter is placed at a 45° angle to the oncoming light it becomes a dichroic filter/mirror. As the name suggests, this type of filter performs two functions, first, to pass specified wavelengths in the forward direction and, second, to deflect blocked light at a 90° angle. To detect multiple signals simultaneously, the precise choice and order of optical filters will be an important consideration.

When light hits a photodetector a small current (a few microamperes) is generated. Its associated voltage has an amplitude proportional to the total number of light photons received by the detector. This voltage is then amplified by a series of linear or logarithmic amplifiers, and by analog to digital convertors (ADCs), into electrical signals large enough (5–10 volts) to be plotted graphically. Log amplification is normally used for fluorescence studies because it expands weak signals and compresses strong signals, resulting in a distribution that is easy to display on a histogram. Linear scaling is preferable where there is not such a broad range of signals e.g. in DNA analysis. The measurement from each detector is referred to as a parameter e.g. forward scatter, side scatter or fluorescence. The data acquired in each parameter are known as the events and refer to the number of cells displaying the physical feature or marker of interest. The speed of flow sorting depends on several factors including particle size and the rate of droplet formation. A typical nozzle is between 50–70 µm in diameter and, depending on the jet velocity from it, can produce 30,000–100,000 droplets per second, which is ideal for accurate sorting. Higher jet velocities risk the nozzle becoming blocked and will also decrease the purity of the preparation. A BD LSRFortessa™ flow cytometer was used in this study.

### **2.3.2. RNA extraction and quantitative polymerase chain reaction (RT-PCR)**

To determine the nature of the cells used in this study at a molecular level, a set of Reverse Transcription-Polymerase Chain Reaction (RT-PCR) analysis was performed. Total RNA was isolated from cells using TRIZOL® Reagent (Invitrogen, Carlsbad, CA), according to the protocol indicated by the manufacturer. RNA concentration and purity were measured using a NanoDrop Spectrophotometer (NanoDrop ND1000, Wilmington, DE, USA). To avoid false-positive results attributable to the amplification of contaminating genomic DNA, total RNA was treated with DNase (Sigma). For the evaluation of stemness, RNA was isolated from AECs at passages P0, P1, P3 and P5. In order to examine the differentiation potential, RNA was extracted from both cells subjected to differentiation induction and control cells (negative controls). Moreover, total RNA was isolated from adult tissues (bone tissue, adipose tissue and spinal cord) and was used as positive controls for the expression of the differentiation markers. Retrotranscription is a reaction that allows obtaining a DNA strand (cDNA) complementary to the RNA isolated. For this purpose, four elements are needed: RNA of interest, deoxyribonucleotides (dNTPs) as building blocks of cDNA, an oligonucleotide able to pair with a portion of the RNA strand and the enzyme retrotranscriptase, able to synthesize DNA starting from an RNA strand. Complementary DNA (cDNA) was synthesized from 500 ng of total RNA using the iScript retrotranscription kit (Bio-Rad Laboratories, Hercules, CA) at the following conditions:

- 25 ° C for 5 minutes;
- 42 ° C for 30 minutes;
- 85 ° C for 5 minutes.

The PCR reaction allows amplifying specific sequences of the cDNA obtained through retrotranscription. The efficiency of this reaction depends on several aspects, such as the ability of primers – forward and reverse – to specifically recognise the binding site on cDNA, the annealing temperature of primers and the concentration of MgCl<sub>2</sub>. The cDNA double strand is subjected to denaturation at high temperatures (95°C). When the two strands are separate, primers must pair with them in a specific and selective way, searching for their complementary sequence on cDNA. This phase is known as annealing and it can be efficient, stable and specific only at a specific temperature value (the annealing temperature), which depends only on the primer sequence. When temperature is too low, non-specific interactions can be favoured, generating unspecific results. Moreover, it is important to evaluate the buffer molarity and the MgCl<sub>2</sub> concentration: in effect, too high concentrations of MgCl<sub>2</sub> bestow a certain viscosity to the sample, causing non-specific results. On the contrary, a too low concentration reduces the efficiency of the reaction. Finally, MgCl<sub>2</sub> concentration has to be chosen in regard to the concentrations of template, dNTPs and primers; all these elements possess phosphate groups, which interact with Mg<sup>+</sup> ions, making them less available for the enzyme. PCR reaction was performed using the “Taq DNA Polymerase recombinant” commercial kit (Invitrogen Life Technologies, 10342-053). The enzyme is purified from a modified *Escherichia coli* strain able to express the gene of *Thermus aquaticus* DNA polymerase. This DNA polymerase is thermostable, so it can synthesize DNA at high temperatures. The amplification reaction consists of the repetition of three steps, for a number of cycles which depends on the target sequence and on the exponential amplification: 1) Denaturation of the double helix; 2) Annealing of the primers to the cDNA strand; 3) Extension of the double helix by the DNA polymerase activity. All the amplification reactions were performed using a T1 Thermocycler (Biometra). The PCR reaction was performed in a reaction mix (20 µl) composed of: (i) 10x PCR Buffer: 2 µl; (ii) 25 mM MgCl<sub>2</sub>: 1.6 µl; (iii) 10 mM Deoxynucleotide Mix: 0.4 µl; (iv) 10 µM Forward Primer: 0.8 µl; (v) 10 µM Reverse Primer: 0.8 µl; (vi) Taq DNA Polymerase: 0.2 µl; (vii) cDNA: 1 µl; (viii) Water: 13.2 µl.

The conditions of the amplification reaction were:

- Initial denaturation: 94°C for 2 minutes;
- Denaturation: 94°C for 30 seconds;
- Annealing: X°C (temperature depending on the melting temperature of primers) for 30 seconds
- Extension: 72°C for 30 seconds
- Final elongation: 72°C for 10 minutes

Denaturation, annealing and extension steps were repeated 32 times.

## 2.4. References:

1. Joy, D.C., Scanning Electron Microscopy, in Materials Science and Technology. 2006, Wiley-VCH Verlag GmbH & Co. KGaA.
2. <http://sites.bio.indiana.edu/~cryo/efem.html>.
3. <http://www.purdue.edu/ehps/rem/rs/sem.htm>.
4. <http://www.microscopyu.com/articles/fluorescence/fluorescenceintro.html>.
5. Lichtman, J.W. and J.-A. Conchello, Fluorescence microscopy. Nature methods, 2005. 2(12): p. 910-919.
6. Petty, H.R., Fluorescence microscopy: established and emerging methods, experimental strategies, and applications in immunology. Microscopy research and technique, 2007. 70(8): p. 687-709.
7. <http://www.nikoninstruments.com/Learn-Explore/Techniques/Confocal>.
8. Nawrocka, A. and J. Lamorska, Determination of Food Quality by Using Spectroscopic Methods. Advances in Agrophysical Research, 2013: p. 347-367.

# COMPOSITE NANOSTRUCTURED CARRIERS FOR BIOACTIVE PROTEINS

### 3.1. Introduction

Nanomedicine represents a powerful tool to treat a variety of diseases and recently has become a primary strategy in different applications of tissue engineering [1]. In regenerative medicine, it has become clear that bioactive molecules, such as growth factors (GF) and cytokines, play the crucial role in orchestrating tissue regeneration [2]. Such process is led by both the cells of the immune systems (e.g. macrophages) [3] and progenitor ones (e.g. mesenchymal stem cells) [4], and have been all exploited as therapeutic targets [5]. To deliver the bioactive molecules at the proper time and for the right window of time is necessary to trigger the different stages of the regeneration in a temporally controlled fashion [6]. This ensures the right consecution of cell functions necessary to start the healing process (e.g. cell migration, growth, differentiation) [7]. The ideal delivery system should be fully tunable, to allow the design of virtually infinite possible release kinetics. Furthermore, it should allow for the encapsulation of high amount of GF, while preserving their functionality during fabrication. Although a plethora of carriers for the release of bioactive molecules have been proposed over the past decade, none of these platforms displayed neither the ideal zero-order release kinetic [8, 9], nor the ability to confine the payload in the target defect for the necessary period of time to allow regeneration [10]. The initial burst release represents a limiting factor in the clinical use of carriers for the release of therapeutic molecules, and unfortunately characterizes most of the currently available delivery systems [11]. In fact, this does not allow for the control over the daily dose of molecule to be released and it has been shown to cause major side effects [11]. A notorious controversy spurred over the release of GF in tissue engineering applications, when Medtronic developed INFUSE®, a collagen sponge impregnated with a solution of recombinant human Bone Morphogenic Protein-2 for bone augmentation. Although the market leader for years, this product has been associated with several disruptive patients' complications (e.g. osteolysis, heterotopic ossification and even cancer) [12, 13]. Thus, the ideal carrier should concurrently confine and retain the biomolecules over time, to preserve the physiology of the surrounding tissues. Poly(lactic-co-glycolic acid) (PLGA) has been proven a material of election for the fabrication of delivery systems, such as microspheres, due to its versatile properties [14-16]. It is approved by Food and Drug Administration and European Medicines Agency for applications of drug delivery due to its biodegradability, biocompatibility and as it also preserves the GF from degradation. Nano-structured porous silicon particles (pSi) have been widely used in the drug delivery field [17], for a multitude of applications, ranging from cancer therapy to tissue engineering, where they revealed to be also osteoconductive [18, 19]. The main peculiarities of pSi particles is that size, shape, porosity and pore size can be finely tailored during manufacturing [20]. The ability of customizing the structure of the particles allows controlling their biodistribution, bioaccumulation, degradation time and also the kinetics. A further degree of control can be done on the particles surface: it can in fact be functionalized to include various drugs and control cellular uptake [21]. The highly porous and interconnected structure of the pSi particles is suitable to load not only small molecules but also proteins and larger payloads. pSi have been efficiently incorporated in a wide range of synthetic polymers in the attempt to introduce a further level of control on the release of the payload [22, 23].

Recently, our group developed a PLGA-pSi composite carrier which revealed of great interest in the field of tissue engineering as it was demonstrated to allow for the release of high amounts of proteins, while preserving

their functionality [24]. Herein, we investigated the influence of both copolymer ratio and size of pSi encapsulated, over the release profiles of a reporter protein Bovine Serum Albumine (BSA-FITC).

## 3.2. Materials and methods

### 3.2.1. Silicon Particles Fabrication and surface modification

Discoidal pSi particles of 1, 3 and 7  $\mu\text{m}$  in diameter and 400 nm thickness, or hemispherical particles of 3  $\mu\text{m}$  in diameter and 600 nm thickness were fabricated by photolithography and electrochemical porosification of

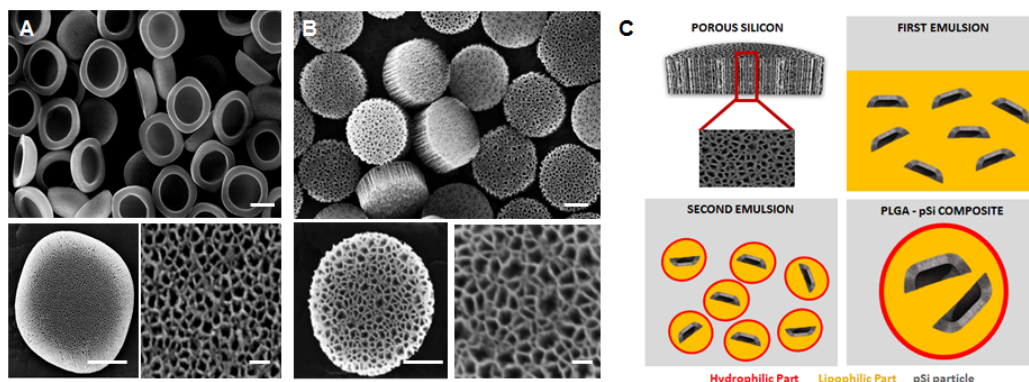


**Figure 3.1 - SEM micrographs of hemispherical (A) and discoidal (B) pSi microparticles; scale bar 1  $\mu\text{m}$ . Schematic describing the main steps of PLGA-pSi synthesis (C).**

patterned silicon wafers, allowing for precise control over particle size and shape, as previously reported [23, 25]. pSi were oxidized as extensively described elsewhere [23, 26]. The surface of the pSi particles was modified with (3-Aminopropyl)triethoxysilane (APTES) (Sigma-Aldrich) as previously described [23, 25]. pSi

morphology was evaluated by scanning electron microscopy (SEM). Particles were dispersed in deionized (DI) water, and a drop was deposited on metal stubs. Samples were coated with 3 nm of Pt/Pb and imaged at a voltage of 7 KV (FEI Quanta 400 ESEM FEG, FEI, Hillsboro, OR). Subsequently,  $2 \times 10^8$  oxidized particles have been suspended and mixed in 1 ml of 4% APTES in Isopropyl alcohol (IPA) solution and 10% DI in IPA. Particles have been mixed at 1300 rpm for 2 h with a thermomixer set at 37  $^{\circ}\text{C}$  and then moved to a vacuum oven for annealing at 60  $^{\circ}\text{C}$  overnight. pSi were labeled with 4',6-diamidino-2-phenylindole (DAPI).

### 3.2.2. Preparation of PLGA-pSi

pSi were encapsulated in PLGA particles via double-emulsion method [20]. Several sets of PLGA-pSi composites were created, varying pSi content (2.5, 5 and 10 wt%), pSi shape (hemispherical or discoidal), pSi size (1, 3 or 7  $\mu\text{m}$ ). Also, different PLGA coatings have been created, by using the copolymer 50:50, 75:25 or 85:15.  $2 \times 10^8$  APTES-modified pSi particles were suspended in 1 ml of different solutions of PLGA (LACTEL), previously dissolved in dichloromethane (DCM) (100 mg/ml) (Sigma-Aldrich). PLGA outer shell was fluorescently labelled by adding Rhodamine B (Sigma) into the PLGA in DCM solution, at a concentration of 1mg/ml. The organic phase was then emulsified with 3ml of 2.5% poly (vinyl alcohol) (PVA) (Fisher Scientific) (25 mg/ml) at 3000 rpm for 6 minutes. The emulsion was dropped into 40 ml of a 1% aqueous solution of PVA (10 mg/ml). The resulting phase has been stirred overnight to allow DCM evaporation; particles were then washed three times with DI water and collected via centrifugation for lyophilization and long term storage.

### 3.2.3. Characterization of PLGA-pSi

Full encapsulation of pSi microparticles in the PLGA microspheres was assessed by optical microscopy. The effect of pSi content, shape and size, and PLGA copolymer ratio on PLGA-pSi size was investigated by measuring the diameter of the microspheres by an automated measuring tool of the software NIS element (Nikon). The zeta potential of the silicon particles, prior to encapsulation in the PLGA shell was analyzed using a Zetasizer nano ZS (Malvern Instruments Ltd., Southborough, MA), as previously described [27]. APTES-modified pSi and the resulting PLGA-pSi microspheres were analyzed by Fourier Transformed Infrared spectroscopy (FTIR). Briefly, a KBr pellet was made by mixing KBr to freeze-dried PLGA-pSi. The KBr chip was analyzed by a

Nicolet 6700 spectrometer (Thermo Scientific). The pSi content in the composite microspheres was characterized by thermogravimetric analysis (TGA), while the thermal properties of PLGA-pSi were evaluated by Differential Scanning Calorimetry (DSC) through the Q600 TG-DSC apparatus (TA instruments).

### 3.2.4. Loading of FITC-BSA into APTES-modified pSi particles and encapsulation in PLGA shell

In order to load the selected reporter protein, APTES modified pSi particles were suspended in 500  $\mu$ L of solution of FITC-BSA (Sigma–Aldrich) in DI (10 mg/ml). The suspension was incubated in physiological-like conditions (PBS, 37°C, under mild agitation). Centrifugation at 4000 rpm for 5 minutes allowed the isolation of the particles. The collected supernatant has been used to estimate the amount of protein absorbed by mass difference using a spectrophotometer

SpectraMax M2 (Molecular Devices) at 493/518 nm. The FITC-BSA loaded particles were then lyophilized overnight. FITC-BSA loaded pSi were encapsulated in PLGA shell, as described above. BSA loading was also evaluated by imaging PLGA-pSi by an A1 confocal laser microscopy (Nikon).

### 3.2.5. Evaluation of FITC-BSA in vitro release

$2 \times 10^8$  FITC-BSA loaded PLGA/pSi microspheres were divided in three aliquots, after dispersing in PBS (1.5 ml): each sample contained approximately  $7 \times 10^7$  particles suspended in 0.5 ml of PBS. Samples were collected, at established time intervals, for 1 month. Each sample was centrifuged (4000 rpm; 5 min), and 10% of the supernatant (0.05 ml) was collected and replaced with fresh PBS. The release of FITC-BSA from the different formulations of PLGA-pSi was quantified by a spectrophotometer at 493/518 nm. Samples were collected and analyzed at defined time points, up to 1 month.

### 3.2.6. Biocompatibility study

J774 macrophages were utilized for this study (ATCC). Briefly, murine J774 macrophages were cultured according to vendor's protocols (ATCC), in HG-DMEM supplemented with 10% FBS, 1% penicillin (100 UI/ml)-streptomycin (100 mg/ml), and 0.25 mg/ml amphotericin B. J774 cells were subcultured by plating them into 96-wells plates at a density of 5000 cells/cm<sup>2</sup> (Millipore). After 24h, cells were treated with PLGA-pSi with PLGA 50:50, 75:25 and 85:15, and fabricated with all sizes of pSi (1  $\mu$ m, 3  $\mu$ m and 7  $\mu$ m). Five different concentrations of microspheres were tested, ranging between 0.1 and 10  $\mu$ g/ml. Viability was evaluated at 72h, in triplicate. Cell interaction with PLGA-pSi was initially evaluated by SEM and samples were prepared for imaging as previously described (FEI Quanta 400 ESEM FEG, FEI, Hillsboro, OR) [28]. Samples were vacuum dried and coated with Pt/Pb and imaged by SEM under a voltage of 8 KV (Hummer 6.2 Sputtering System; Anatech Ltd.,

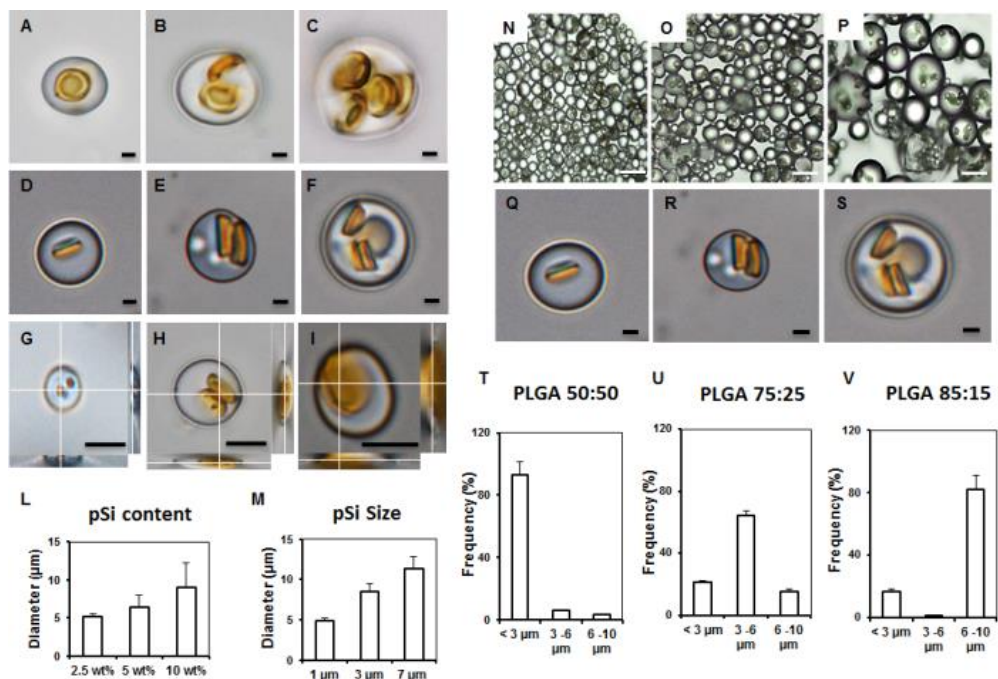


**Figure 3.1 - Images of the different formulations of PLGA-pSi by optical microscopy (bright field). PLGA-pSi fabricated with increasing amount of hemispherical pSi (A, B, C) and discoidal pSi (D, E, F); scale bar 1  $\mu$ m. PLGA-pSi made with discoidal pSi of increasing diameter (G, H, I; scale bar 5  $\mu$ m), and bar graphs reporting about the effect of such factors on the overall size of the resulting PLGA-pSi (L, M). Image of PLGA-pSi prepared with 50:50, 75:25 and 85:15 PLGA copolymer ratios (N, O, P respectively; scale bar 20  $\mu$ m), and their magnification (Q, R, S). Size distribution of the resulting sets of PLGA-pSi (T, U, V); scale bar 1  $\mu$ m.**

Union City, California). The toxicity of the different formulations and concentrations of PLGA-pSi described above was evaluated by MTT assay, according to manufacturer's protocol (Life Technology).

### 3.2.7. Subcutaneous injection

28 BALB/c mice (8 to 12 weeks old) were housed and fed in the animal room at The Houston Methodist Research Institute (Houston, Texas) for 48 hours prior to the experiment. The study protocols were approved by the Institutional Animal Care and Use Committee (IACUC) and performed following GMP standards. All efforts were made to minimize the number of animals used for experiments and their suffering. Animals were anaesthetized with 2–3 % isoflurane in 100 % oxygen at a flow rate of 1 L/min. A  $1 \times 1 \text{ cm}^2$  area of skin was carefully shaved and sterilized. Mice were injected at a dorsal subcutaneous site with 50  $\mu\text{L}$  of a PLGA-pSi suspension in PBS. Seven animals per each time point were used. In each animal two injections were performed: one as a control (PBS only) and one with the PLGA-pSi suspension. Mice were euthanized at 2h and 3, 7 and 14 days, by  $\text{CO}_2$  inhalation and subsequent cervical dislocation

### 3.2.8. *in vivo* release study

One mouse per each time point was imaged by Intravital microscopy (IV), prior to be euthanized, to follow the *in vivo* release of the reporter protein. Briefly, the skin was gently dissected, flipped and imaged at three wavelengths: 610 nm for PLGA microsphere (labeled with Rhodamine B), 460 nm for pSi particles (labeled with DAPI) and 516 nm for FITC-BSA. Region of interest were created with a specific tool of the software NIS-Element (Nikon) to evaluate the diffusion of BSA from the microspheres, and to verify the confinement of the carriers over 2 weeks.

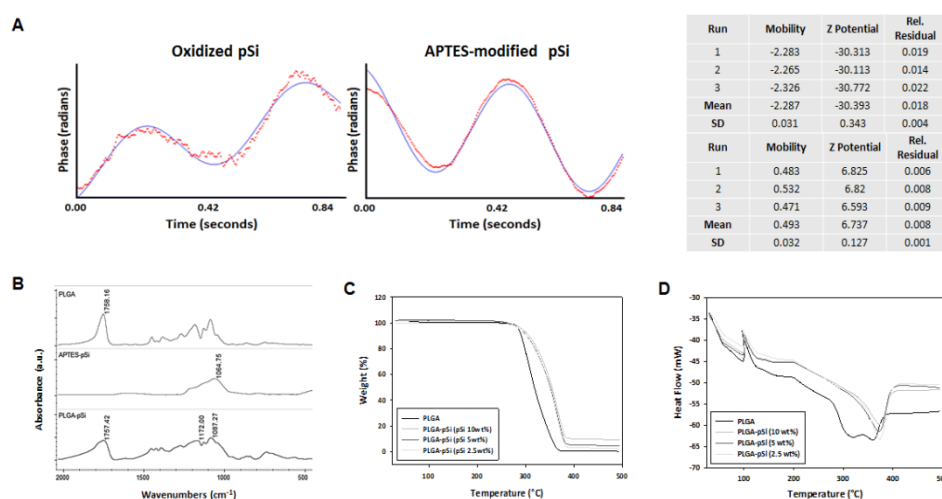


Figure 2.3 - Zeta potential (A), FTIR (B) and TG-DSC analysis.

### 3.2.9. *in vivo* degradation of PLGA-pSi

Three subcutaneous pouches of PLGA microspheres were collected and fixed for SEM images in 2.5% glutaraldehyde and prepared for SEM evaluation, by dehydration in increasing concentration of ethanol (EtOH), as described elsewhere [29]. Samples were sputter coated with 25 nm of Pt/Pb and imaged with a voltage of 10 kV, to evaluate the *in vivo* degradation of the carriers.

### 3.2.10. Biodistribution

After imaging of the pouches, organs were collected and homogenized in 20% EtOH in 1M NaOH and incubated under mild agitation for 24 hours at room temperature, to further verify confinement of the microspheres. Weighted organs (lungs, liver, kidneys, spleen) and PLGA-pSi pouches were then centrifuged at 5000 rpm for 30 minutes and supernatant was collected, filtered using 0.45  $\mu\text{m}$  nylon centrifugal filter microfuge tubes (VWR) and diluted with DI for elemental analysis by ICP-OES (Varian 720 ES, Varian Inc., Walnut Creek, CA) as previously described [30].

### 3.2.11. Histological evaluation

At each time point, one control and one PLGA-pSi pouch were collected and fixed in Optimal Cutting Temperature compound (O.C.T.) (Tissue Tek, SAKURA) for histology. Briefly, samples were cut 10  $\mu\text{m}$  thick, and sections were washed twice in fresh xylene for 8-10 min and rehydrated sequentially with decreasing ethanol concentrations (100%, 95%, 90%, 80%, 70%) and DI water (8-10 min for each step). Histological visualization of collagenous connective tissue fibers in tissue sections was achieved using a commercial available kit for Trichrome Stain (Abcam; ab150686), according to the manufacturer's instructions. The air-dried slides were then mounted with Cytoseal XYL (Thermo Scientific) mounting medium and then analyzed by Nikon Histological Microscope.

### 3.2.11. Statistical analysis

Statistics were calculated with Prism GraphPad software. Statistics for experiments was performed using a Two-Way ANOVA followed by a Tukey's multiple comparison test. In all cases \* was used for  $p < 0.05$ , \*\* for  $p < 0.01$ , and \*\*\* for  $p < 0.001$ , and \*\*\*\* for  $p < 0.0001$ . All experiments were performed at least in triplicates. Data is presented as mean  $\pm$  SD.

## 3.3. Results and Discussion

### 3.3.1. Evaluation of the morphology and size distribution of PLGA-pSi

The ability to finely control the shape and size of a carrier for bioactive molecules is crucial to ensure a tight control over the physic-chemical properties of the system, its loading efficiency and ultimately its control over the release kinetics of the payload. In this study, we investigated the tunability of a composite carrier based on a pSi core and an outer polymeric shell. Both components are fully tunable and can be tailored to address any release need. The main aim of this study was to assess the full tailorability of the PLGA-pSi composite microspheres and to elucidate the role of several fundamental variables during the synthesis (e.g. size and amount of pSi, copolymer ratio of PLGA).

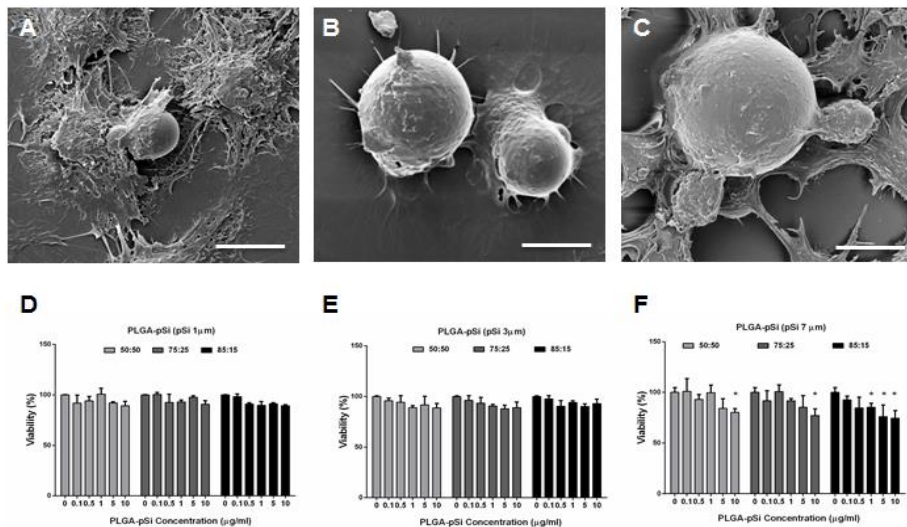


**Figure 3.3 - Viability of J774 macrophages when incubated with increasing concentrations of the different PLGA-pSi formulations, by MTT analysis (A, B, C). SEM images showing the interaction of J774 macrophages with PLGA-pSi (D, E, F); scale bar 5  $\mu\text{m}$ . Biodistribution study of Si in the organs respect to the pouch (G).**

resulted scalable and reproducible, giving pSi of uniform shape and size, which is key to ensure control over the loading and release of the payload.

However, it has been extensively demonstrated that pSi degradation in biological conditions results very fast and thus not compatible with tissue engineering applications [31]. A modified double emulsion method was followed to fully encapsulate the pSi in the PLGA microspheres (Figure 3.1C), creating composite microspheres, overcoming this limitation and prolongs the release of the payload. PLGA was chosen to synthesize the outer shell of the composite microspheres, as it is commercially available in a wide range of copolymer ratios,

molecular weights and viscosities, which influence the degradation rate of the polymer *in vitro* and *in vivo*, by modulating its hydrophilic properties, thus also fully tailorable [32, 33].

Thus, our composite delivery systems has the advantage that can be fully customized to match the user needs, but also that by merging pSi and PLGA (a inorganic and organic phase), it is possible to obtain a more stable platform when exposed to the fluctuation of the microenvironment of tissues [8, 34-36]. Furthermore, it was demonstrated that the two phases degrade in byproducts that act as a buffer, producing a neutral pH, thus avoiding protein degradation [24].

By varying pSi content during the synthesis (2.5, 5 and 10 wt%) we observed an increase in the mean diameter of the resulting PLGA-pSi composite microspheres: 5.103 ( $\pm 0.373$ )  $\mu\text{m}$  for the 2.5wt% pSi in PLGA, 6.435 ( $\pm 1.494$ )  $\mu\text{m}$  for the 5wt% pSi in PLGA and 9.013 ( $\pm 3.230$ )  $\mu\text{m}$  for the 10% pSi in PLGA (Figure 3.2 A, B, C). We also attempted the same study with discoidal pSi particles, and we observed a size distribution pattern increasing similarly to PLGA-pSi prepared with hemispherical pSi (Figure 3.2 D, E, F). Similarly, by utilizing discoidal pSi of increasing diameter (1, 3 and 7  $\mu\text{m}$ ) also the mean size of the resulting microspheres increased accordingly (Figure 3.2 G, H, I). The mean diameter of all the above mentioned formulations of PLGA-pSi are reported in the bar graphs in figure 2 L and M.

Finally, discoidal pSi were used to synthesize PLGA-pSi with 3 different copolymer ratios: 50:50, 75:25 and 85:15. At higher copolymer ratios the overall size of PLGA-pSi increased (Figure 3.2 N, O, P) and resulted in a higher content of pSi particles (Figure 3.2 Q, R, S). PLGA-pSi fabricated with 50:50 and 85:15 copolymers displayed a superior size distribution respect to that made with 75:25 PLGA, which appeared including 3 distinct subpopulations of microspheres, and thus resulting to be less reproducible.

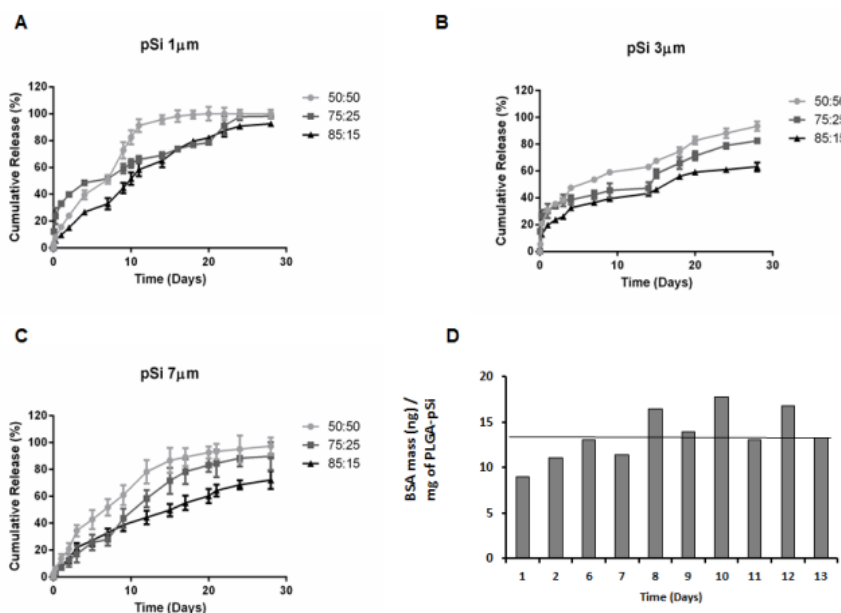


**Figure 3.4 - Cumulative release of FITC-BSA from the different formulations of PLGA-pSi (A, B, C). Amount of BSA (ng) released daily from PLGA-pSi with formulation PLGA 85:15/pSi 1  $\mu\text{m}$ .**

### 3.3.2. Physicochemical characterization of PLGA-pSi

In order to diminish the hydrophobicity of the particles and enhance their loading efficiency, particles surface was firstly oxidized by etching [37]. This steps allowed for the introduction of hydroxyl groups on the surface of the silicon particles, and to allow for the addition of amine groups by surface modification with APTES. Zeta potential analysis showed a mean surface charge of 6.737 mV after APTES modification, versus the initial value of -30.39 mV (Figure 3.3 A). The capacity of FITC-BSA (and bioactive proteins) to be loaded onto the pSi particles is affected by the surface characteristics. BSA, in fact, had a negative charge and the electrostatic interaction between amine groups of APTES and acidic moieties of BSA intensified the ability of FITC-BSA to be loaded into the pores of pSi particles.

PLGA-pSi were also characterized by FTIR spectroscopy. The analysis showed a broadening of peaks corresponding to the stretching of Amide I ( $1750\text{--}1735\text{ cm}^{-1}$ ), suggesting the ionic interaction of the carbonyl groups on the surface of the PLGA with the amine groups of APTES-modified pSi (Figure 3.3 C).

Finally, TGA analysis was performed for PLGA-pSi 85:15 with different amount of pSi (2.5, 5 and 10wt %). Results are shown in Figure 3 D. pSi content for the three formulations resulted in the 2.674 wt%, 2.660 wt% and 7.427 wt%, respectively. From DSC analysis it was observed an increase in the  $T_m$  of PLGA-pSi respect to empty PLGA microspheres (used as a control) of approximately  $15^\circ\text{C}$ , proving the existence of a chemical interaction between pSi and the polymer. Also among the three formulations of PLGA-pSi, the heat flow value of those endothermic reactions resulted progressively decreased at higher contents of pSi.

### 3.3.3. Evaluation of FITC-BSA release kinetics *in vitro*

The temporal control over the release of the payload is fundamental to guarantee the proper therapeutic effect, for the necessary window of time. In fact, the tight regulation of the dose of bioactive molecule released daily allows avoiding side effects due to overdoses or the progression of the pathological state due to an insufficient amount of drug.

The release of FITC-BSA was assessed over a month. What resulted evident from the release study was that the increase of the copolymer ratio of the PLGA coating, enabled for the progressive reduction of the initial burst release (Figure 3.4), and a slower release rate. This was probably due also to the fact that the FITC-BSA was found secured in correspondence of the pSi core, and thus protected from the environment, avoiding burst release (Supplementary figure 1).

Also, we found that the bigger the size of the pSi microspheres utilized in the preparation of the PLGA-pSi, the slower was the release of the reporter protein.

However, using progressively bigger sizes of pSi, we observed higher variability in the amount of protein released daily. The daily release of FITC-BSA for the formulation PLGA-pSi 85:15/pSi  $1\ \mu\text{m}$  resulted the most consistent (approximately 12 ng/day), and it is reported in figure 4 D.

The main goal of this study was the ability to fully tailor the PLGA-pSi to accomplish a temporal and spatial control over the release of proteins *in vivo*. Thus, as a proof of concept, we chose this PLGA-pSi formulation (PLGA 85:15/pSi  $1\ \mu\text{m}$ ) as the most reproducible in terms of size and control over the release (lower standard deviations), as well as characterized by no initial burst release.

### 3.3.4. Biocompatibility

Macrophages have been demonstrated to be one of the first type of immune cells to intervene at the site of injury [38]. Thus, we simulated the *in vitro* response to the PLGA-pSi by incubating murine macrophages with increasing concentrations of PLGA-pSi of different formulations.

Macrophages' viability resulted not significantly compromised by increasing concentrations of PLGA-pSi (both made with 1 and  $3\ \mu\text{m}$  pSi) (Figure 3.5 A, B). We observed that with PLGA-pSi made with  $7\ \mu\text{m}$  pSi, their

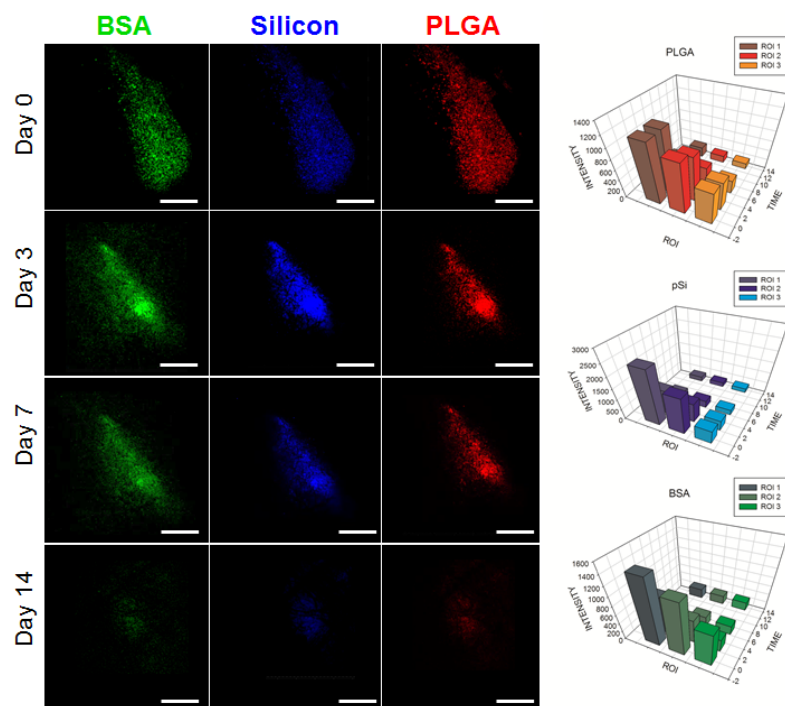


**Figure 3.5 - Fluorescence images acquired by intravital microscopy to evaluate the *in vivo* release over 2 weeks. PLGA shell is represented in red , pSi in blue and BSA in green. Scale bar 1 mm.**

viability slightly decreased by increasing the amount of PLGA-pSi in the media, but remained above 80% (Figure 3.5 C). Macrophages' interaction with PLGA-pSi of different sizes is depicted in Figures 3.5 D, E and F, which show cells engulfing PLGA-pSi or surrounding them when bigger than their size (approximately 8-10  $\mu\text{m}$  in diameter).

### 3.3.5. *in vivo* spatially controlled release

Ultimately, we wanted to assess if the ability to control the spatial and temporal control over the release of FITC-BSA accomplished *in vitro*, was preserved *in vivo*. The release of the reporter protein was followed over 14 days, in the mouse subcutaneous model. In figure 3.6 A are presented the images acquired by IV. The panel shows that both PLGA (red) and pSi (blue) signals overlap for all the window of time considered. This was further demonstrated by the fluorescence intensity plot, in which the fluorescence signals of the three components of the carrier not only overlap, but it shows that the outer layer of the system is the PLGA (red), the middle one is pSi (blue) and the inner component is the FITC-BSA (green). Concerning FITC-BSA, it is possible to identify a slight diffusion of the protein outside the area where PLGA-pSi were localized. However, the BSA diffused in the immediate surroundings of the microspheres (distributed over an area of 1.148  $\text{cm}^2$ ) over a maximum area of 4.778  $\text{cm}^2$ , thus demonstrating the ability of PLGA-pSi to retain FITC-BSA at the earliest time point, avoiding the initial burst release, as characterized *in vitro*.

After IV, the pouch was also imaged by SEM, to better evaluate the morphology and degradation of PLGA-pSi. Figure 7 depicts the microspheres after injection, at day 3, 7 and 14. At all time points it is possible to identify PLGA-pSi microspheres, as indicated by the white arrows.

If internalized by phagocytes (see paragraph 3.3.4), PLGA-pSi would be cleared out and transported to the spleen, or the kidney, for example. Thus, we finally evaluated the spatial control over the payload by evaluating the confinement of pSi in the pouch.

ICP analysis of the content of Si in mice's organs showed that at day 1 more than 85% of Si was found in the site of injection, while progressively decreasing over a month (54% at 14 days and 18% at 30 days), mirroring the sustained release of the protein *in vitro*.

After IV, the pouch was also imaged by SEM, to better evaluate the morphology and degradation of PLGA-pSi. Figure 3.7 depicts the microspheres after injection, at day 3, 7 and 14. At all time points it is possible to identify PLGA-pSi microspheres, as indicated by the white arrows.

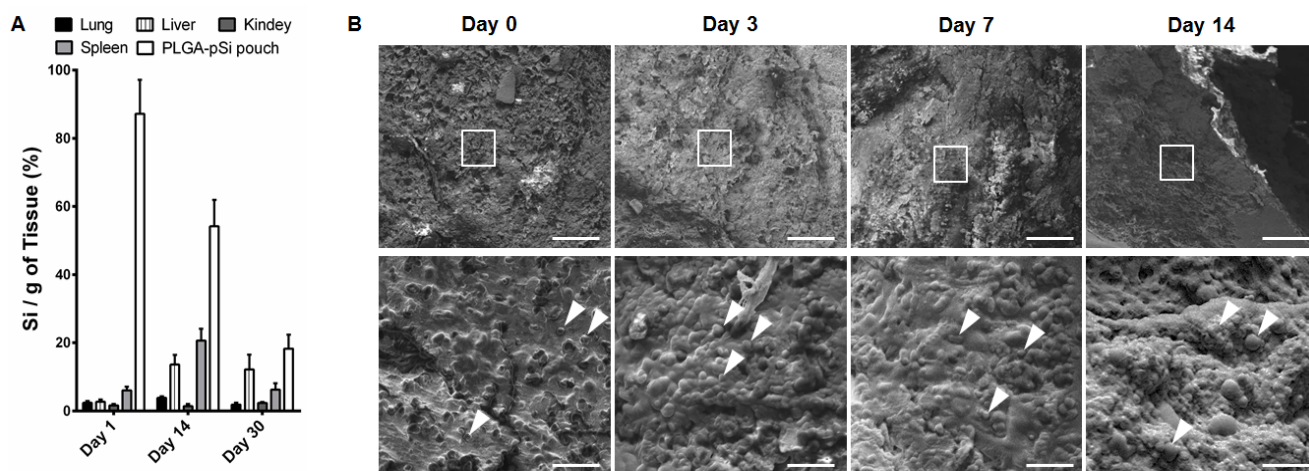


Figure 3.6 -- SEM micrographs of the microspheres found in the pouches at day 0, 3, 7 and 14 after injection in the mouse subcutaneous model. Scale bar panels A-D 100  $\mu\text{m}$ , E-F 30  $\mu\text{m}$ .

### 3.3.6. Histology

Panel in figure 3.8 shows the pouch up to 14 days after injection, compared to the control. The images of the controls immediately after injection (of PBS), presented fibers and a minor accumulation of cells, which resolved over the two weeks evaluated. In the pouches injected with PLGA-pSi, at day 0 it was observed the accumulation of fibers (blue) and of a few cells, similarly to what was found in the control samples. Within two weeks the outer polymeric shell (labelled with Rhodamine B), started to slowly degrade, and release part of the dye, as it can be noticed by the more intense red color of the slides. All together these data confirm the controlled process of degradation of PLGA-pSi *in vivo*, which reflected in a slow and sustained release of the reporter protein, within the pouch.

### 3.4. Conclusions

In summary, we have demonstrated the full tunability of PLGA-pSi composite microspheres. This kind of composite carrier combines the advantages of mesoporous structures to be loaded with high amount of proteins, due to their high surface area, and the plasticity and tailorability of polymers. In this study the formulation which accomplished the most controlled and sustained release was tested *in vivo*, to demonstrate the temporal and spatial control over the release of the payload. However, depending on the application, it is possible to envision the use of other formulations, and also the combined use of multiple formulations of PLGA-pSi. They also result greatly advantageous by being injectable, which would allow for an easy administration of a molecule of interest, once a month, while showing low toxicity. These results assessed *in vivo* that PLGA-pSi represent a robust, reproducible and scalable platform to be translated in the clinic, for applications of tissue regeneration.

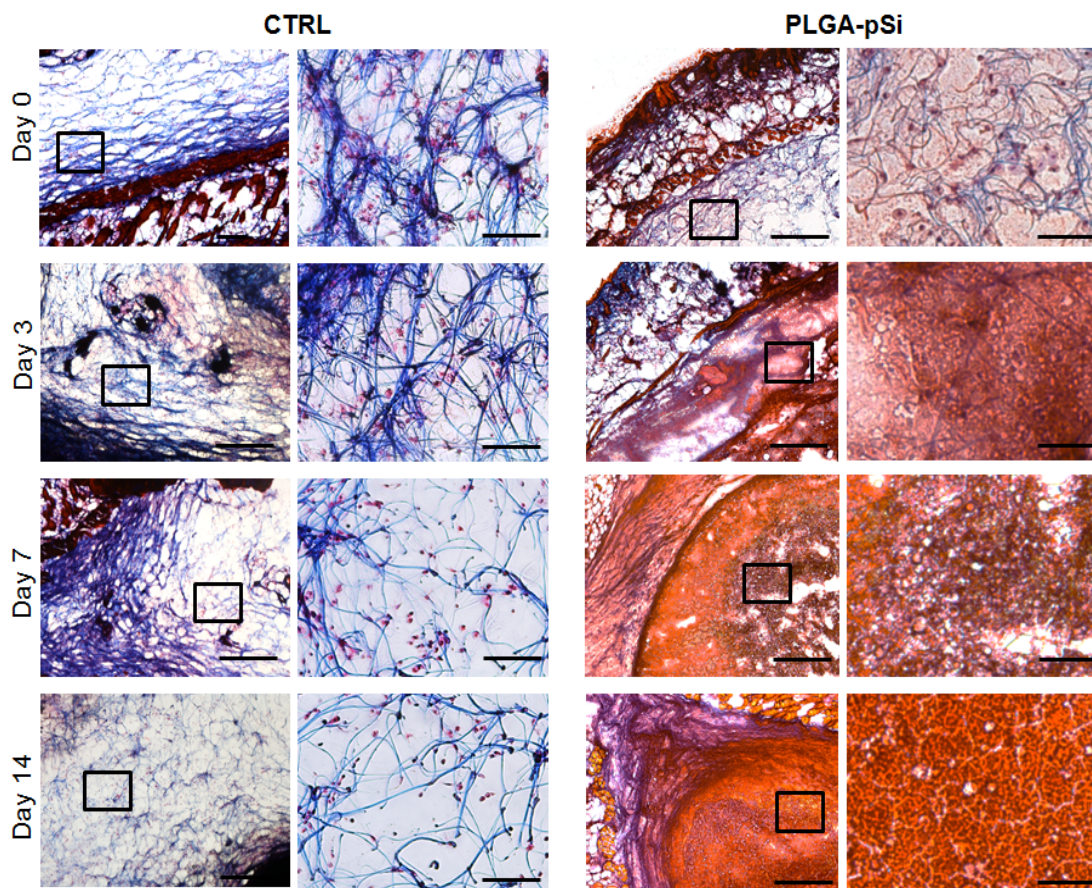


Figure 3.7 - Histological evaluation of the pouches at day 0, 3, 7 and 14 after injection of PLGA-pSi in the mouse subcutaneous model. Scale bar 20  $\mu$ m.

### 3.5. References

1. Chaudhury, K., et al., *Regenerative nanomedicine: current perspectives and future directions*. International journal of nanomedicine, 2014. **9**: p. 4153.
2. Lee, K., E.A. Silva, and D.J. Mooney, *Growth factor delivery-based tissue engineering: general approaches and a review of recent developments*. Journal of The Royal Society Interface, 2011. **8**(55): p. 153-170.
3. Mantovani, A., et al., *Macrophage plasticity and polarization in tissue repair and remodelling*. The Journal of pathology, 2013. **229**(2): p. 176-185.
4. Law, S. and S. Chaudhuri, *Mesenchymal stem cell and regenerative medicine: regeneration versus immunomodulatory challenges*. American journal of stem cells, 2013. **2**(1): p. 22.
5. Reya, T., et al., *Stem cells, cancer, and cancer stem cells*. nature, 2001. **414**(6859): p. 105-111.
6. Swami, A., et al., *Nanoparticles for targeted and temporally controlled drug delivery*, in *Multifunctional Nanoparticles for Drug Delivery Applications*. 2012, Springer. p. 9-29.
7. Stroncek, J.D. and W.M. Reichert, *Overview of wound healing in different tissue types*. Indwelling neural implants: strategies for contending with the in vivo environment, 2008.
8. Makadia, H.K. and S.J. Siegel, *Poly lactic-co-glycolic acid (PLGA) as biodegradable controlled drug delivery carrier*. Polymers, 2011. **3**(3): p. 1377-1397.
9. Huang, X. and C.S. Brazel, *On the importance and mechanisms of burst release in matrix-controlled drug delivery systems*. Journal of Controlled Release, 2001. **73**(2): p. 121-136.
10. Vallet-Regí, M., et al., *Drug confinement and delivery in ceramic implants*. Drug metabolism letters, 2007. **1**(1): p. 37-40.
11. Yeo, Y. and K. Park, *Control of encapsulation efficiency and initial burst in polymeric microparticle systems*. Archives of pharmacal research, 2004. **27**(1): p. 1-12.
12. Epstein, N.E., *Complications due to the use of BMP/INFUSE in spine surgery: the evidence continues to mount*. Surgical neurology international, 2013. **4**(Suppl 5): p. S343.
13. Epstein, N.E., *Pros, cons, and costs of INFUSE in spinal surgery*. Surgical neurology international, 2011. **2**.
14. Bouissou, C., et al., *The influence of surfactant on PLGA microsphere glass transition and water sorption: remodeling the surface morphology to attenuate the burst release*. Pharmaceutical research, 2006. **23**(6): p. 1295-1305.
15. Jain, R.A., *The manufacturing techniques of various drug loaded biodegradable poly (lactide-co-glycolide)(PLGA) devices*. Biomaterials, 2000. **21**(23): p. 2475-2490.
16. Ruhe, P.Q., et al., *rhBMP-2 release from injectable poly (DL-lactic-co-glycolic acid)/calcium-phosphate cement composites*. The Journal of Bone & Joint Surgery, 2003. **85**(suppl\_3): p. 75-81.
17. Tasciotti, E., et al., *Mesoporous silicon particles as a multistage delivery system for imaging and therapeutic applications*. Nat Nanotechnol, 2008. **3**(3): p. 151-157.
18. Sun, W., et al., *Nano-to Microscale Porous Silicon as a Cell Interface for Bone-Tissue Engineering*. Advanced materials, 2007. **19**(7): p. 921-924.
19. Sun, W., et al., *Nano- to Microscale Porous Silicon as a Cell Interface for Bone-Tissue Engineering*. Advanced materials, 2007. **19**(7): p. 921-924.
20. Chiappini, C., et al., *Tailored porous silicon microparticles: fabrication and properties*. ChemPhysChem, 2010. **11**(5): p. 1029-1035.
21. Decuzzi, P., et al., *Size and shape effects in the biodistribution of intravascularly injected particles*. Journal of Controlled Release, 2010. **141**(3): p. 320-327.
22. Martinez, J.O., et al., *Engineering multi-stage nanovectors for controlled degradation and tunable release kinetics*. Biomaterials, 2013. **34**(33): p. 8469-8477.
23. Fan, D., et al., *Mesoporous Silicon-PLGA Composite Microspheres for the Double Controlled Release of Biomolecules for Orthopedic Tissue Engineering*. Adv. Funct. Mater., 2012. **22**(2): p. 282-293.
24. Fan, D., et al., *Mesoporous Silicon-PLGA Composite Microspheres for the Double Controlled Release of Biomolecules for Orthopedic Tissue Engineering*. Advanced Functional Materials, 2012. **22**(2): p. 282-293.
25. Chiappini, C., et al., *Tailored Porous Silicon Microparticles: Fabrication and Properties*. ChemPhysChem, 2010. **11**(5): p. 1029-1035.
26. De Rosa, E., et al., *Agarose surface coating influences intracellular accumulation and enhances payload stability of a nano-delivery system*. Pharm Res, 2011. **28**(7): p. 1520-30.

27. De Rosa, E., et al., *Agarose surface coating influences intracellular accumulation and enhances payload stability of a nano-delivery system*. *Pharmaceutical research*, 2011. **28**(7): p. 1520-1530.
28. Taraballi, F., et al., *Potential Avoidance of Adverse Analgesic Effects Using a Biologically "Smart" Hydrogel Capable of Controlled Bupivacaine Release*. *Journal of pharmaceutical sciences*, 2014.
29. Minardi, S., et al., *Multiscale Patterning of a Biomimetic Scaffold Integrated with Composite Microspheres*. *Small*, 2014.
30. Decuzzi, P., et al., *Size and shape effects in the biodistribution of intravascularly injected particles*. *Journal of Controlled Release*, 2010. **141**(3): p. 320-327.
31. Minardi, S., et al., *Multiscale Patterning of a Biomimetic Scaffold Integrated with Composite Microspheres*. *Small*, 2014. **10**(19): p. 3943-3953.
32. Kinam, P. and J.M. Randall, *Controlled Drug Delivery*. ACS Symposium Series. Vol. 752. 2000: American Chemical Society. 478.
33. Anderson, J.M. and M.S. Shive, *Biodegradation and biocompatibility of PLA and PLGA microspheres*. *Advanced drug delivery reviews*, 2012. **64**: p. 72-82.
34. Jain, R., et al., *Controlled drug delivery by biodegradable poly (ester) devices: different preparative approaches*. *Drug development and industrial pharmacy*, 1998. **24**(8): p. 703-727.
35. Lim, T.Y., C.K. Poh, and W. Wang, *Poly (lactic-co-glycolic acid) as a controlled release delivery device*. *Journal of Materials Science: Materials in Medicine*, 2009. **20**(8): p. 1669-1675.
36. Wischke, C. and S.P. Schwendeman, *Principles of encapsulating hydrophobic drugs in PLA/PLGA microparticles*. *International Journal of Pharmaceutics*, 2008. **364**(2): p. 298-327.
37. Tasciotti, E., et al., *Mesoporous silicon particles as a multistage delivery system for imaging and therapeutic applications*. *Nature nanotechnology*, 2008. **3**(3): p. 151-157.
38. Spiller, K.L., et al., *The role of macrophage phenotype in vascularization of tissue engineering scaffolds*. *Biomaterials*, 2014. **35**(15): p. 4477-4488.

# MULTISCALE PATTERNING OF BIOMIMETIC SCAFFOLDS

## 4.1. Introduction

The fate of a cell is determined by a complex set of biomolecules, which create the tissue-specific biochemical *milieu*, and by the nano- and micro-scale physical features that ultimately define tissues macroscopically [1]. The elucidation of the stimuli necessary to achieve proper tissue regeneration has focused scaffolds' design toward the mimicry of the chemical and structural determinants of the tissue of choice [2, 3]. A wide range of signaling molecules has been utilized to enhance the recruitment, proliferation and differentiation of autologous cells in the scaffolds. As an example, Bone Morphogenetic Protein-2 (BMP-2)[4] and Transforming Growth Factor Beta (TGF- $\beta$ ) [5], are extensively used for bone and cartilage regeneration. A plethora of biomaterials based on polysaccharides (e.g. hyaluronic acid and alginate), proteins (e.g. fibrin, gelatin, and collagens) or synthetic polymers (e.g. poly(lactic acid) (PLA), poly(lactic acid)-co-(glycolic acid) (PLGA)) have been tested for tissue engineering applications [5-7]. Collagen has attracted material scientists because it is one of the main components of human tissues. Its fibers spontaneously organize in supra-molecular networks, whose nano-topography is critical for conserving both biochemical (protein adsorption and growth factor retention) [8] and biological (cell adhesion, migration, and differentiation) mechanisms [1]. The initial strategy was to add the growth factors by directly soaking the scaffold in a solution containing the factors of choice [9]. Unfortunately, a recent controversy spurred from the adverse effects of excessive and uncontrolled release of recombinant human – BMP-2 in patients treated with collagen implants for spine fusion, brought the attention on the need to control the spatial and temporal distribution of the growth factor in the scaffold [10, 11].

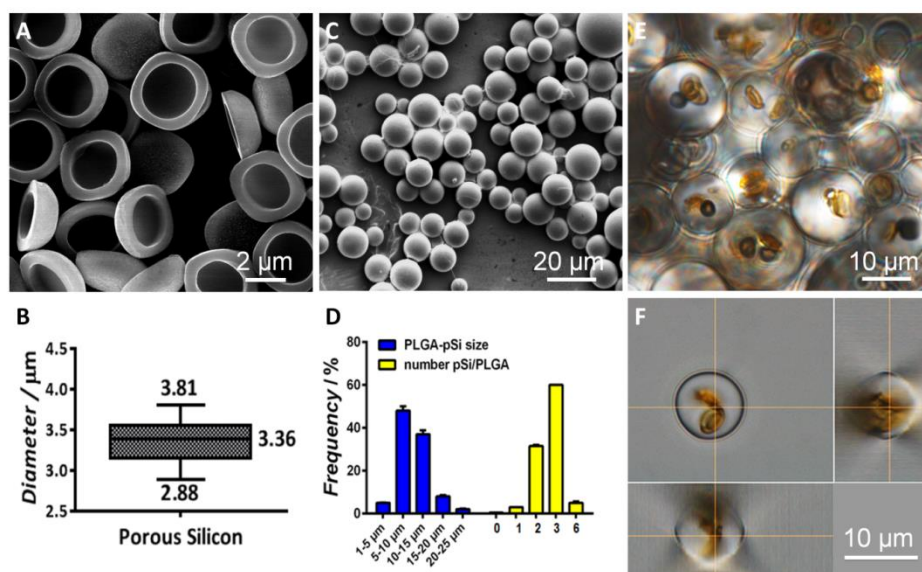


**Figure 4.1 - Characterization of PLGA-pSi microspheres. (A)** SEM image of pSi illustrating their typical quasi-hemispherical shape; **(B)** Maximum, mean, and minimum pSi size; **(C)** SEM image and **(D)** size distribution of PLGA-pSi microspheres and number of pSi per PLGA microsphere. **(E)** Optical microscope image of PLGA-pSi composite microspheres (PLGA: transparent sphere; pSi: brown hemispheres); **(F)** sliced view of a PLGA-pSi microsphere showing full integration of pSi.

To recapitulate how these growth factors are naturally presented, it is necessary to engineer scaffolds able to mimic the sequential release of multiple molecules from various intra-scaffold compartments [12, 13]. The control of the material's structure at the nano-, micro- and macro-scale is of paramount importance to ensure the optimal three dimensional (3D) release and distribution of bioactive factors [14, 15]. Nanostructured porous silicon [16] revealed a valuable material in tissue engineering for its osteoconductivity [17, 18], and to develop porous particles able to accommodate high amount of proteins [19]. Thus, pSi has been efficiently incorporated in a wide range of synthetic polymers for composite scaffolds' fabrication [20, 21], or for the development of composite delivery systems able to load, store and release multiple proteins from days to weeks and months [22, 23]. These composite delivery platforms have the advantage to be easily tunable to match their release rates to those of native tissue, and to be more stable than the scaffold in which the delivery systems were added through surface adsorption [24-26]. The lack of a tight confinement and protection of the delivery systems implies that once the scaffolds are implanted, they are exposed to the fluctuation of the microenvironment (e.g. pH, enzymatic activity, abnormal accumulation of fluid, etc) and to phagocytic cells of the immune systems which alter the composition of the scaffold and the stability of its individual components [27]. However the dispersion of particles in a microfibrillar polymer such as natural type I collagen is challenging as well as the homogenous and effective retain of the particles in the final 3D scaffold. Type I collagen has the advantage to closely resemble ECM, but its hierarchically organized fibrous structure does not allow the use of the common methods of fabrication (e.g. electrospinning, sonication), without affecting its structure, which is key for its biological functions [28]. Here we propose a systematic approach for the synthesis of multiscale fibrous type I collagen scaffolds patterned with PLGA-pSi composite microspheres for the temporal and spatial release of proteins, addressing all the current limitations. This proof of concept study shows that the integration of the delivery systems within the two layers of a collagen scaffold, allows the triple-controlled release of two reporter proteins, the spatial confinement of the microspheres and the preservation of the nano- micro- and macro-scale features of the scaffold.

## **4.2. Materials and Methods**

### *4.2.1. Silicon Particles Fabrication and Surface Modification*

Hemispherical porous silicon particles of 3.2  $\mu\text{m}$  in diameter and 600 nm thick were fabricated by photolithography and electrochemical porosification of patterned silicon wafers, allowing for precise control over particle size and shape, as previously reported [23, 29]. Silicon particles were oxidized as extensively described elsewhere [23, 30]. The surface of the pSi particles was modified with APTES (Sigma-Aldrich) as previously described [23, 29].

### *4.2.2. PLGA-pSi Optimization and Characterization*

$2 \times 10^8$  APTES modified pSi were dispersed, by sonication, in a solution of PLGA (50:50) (LACTEL) dissolved in dichloromethane (DCM) (375  $\mu\text{L}$ , 50 mg/ml) (Sigma-Aldrich). The organic phase containing the pSi was mixed with poly (vinyl alcohol) (PVA) (Fisher Scientific) (1,5 mL, 25 mg/ml) by homogenization. The emulsion was dropped into an aqueous solution (50 mL) containing PVA (5 mg/ml). The resulting suspension was stirred for 6 h to allow the evaporation of the dichloromethane, then washed three times with DI water. Empty PLGA microspheres were eliminated by differential centrifugation, as we previously implemented [23]. PLGA-pSi's morphology of the microspheres was characterized by SEM (FEI Nova NanoSEM 230). They were sputtered coated by a Plasma Sciences CrC-150 Sputtering System (Cressington 208HR), and examined under a voltage of

7 KV. Also, they were imaged through optical microscopy (Nikon Eclipse TS 100), and PLGA-pSi size distribution was measured through an automated measurement tool of the software NIS-Element (Nikon).

#### 4.2.3. Preparation of the collagen slurry

1 g of type I collagen (Sigma-Aldrich) were dissolved in an acetate buffer (pH 3.5) to reach the desired concentration (20 mg/ml) [31]. The collagen suspension was precipitated by the addition of sodium hydroxide (0.1 M) solution at pH 5.5. The collagen was washed three times with DI water. The collagen was cross-linked through dispersion for 48 h in a 1,4-butanediol diglycidyl ether (BDDGE) (Sigma-Aldrich) aqueous solution (2.5 mM), setting up the 1, 4-butanediol diglycidyl ether (BDDGE)/collagen ratio (1 wt%) [31]. The collagen was washed 3 times in DI water.

#### 4.2.4. Fabrication of CTRL, ADS and INT scaffolds

The cross-linked collagen (20 mg dry weight) was suspended in DI water (5 mL), and three groups of collagen scaffolds were fabricated: (i) CTRL; (ii) ADS; (iii) INT. To fabricate the ADS, PLGA-pSi were suspended in water (2 mg/mL) and the scaffolds were swollen in the dispersion. The same amount of particles was instead integrated during fabrication of INT, at their slurry state. The materials were freeze-dried with a controlled freezing ramp from 25 °C to -25 °C and a heating ramp from -25 °C to 25 °C in 50 min under vacuum conditions ( $P = 0.20$  mbar), and collagen scaffolds (20 mm<sup>3</sup>) were produced. Blank collagen scaffolds were used as CTRL. The evaluation of scaffolds morphology was performed through SEM. A set of fluorescently labeled PLGA-pSi were prepared for confocal laser microscopy imaging (A1 Nikon Confocal Microscope). PLGA was labeled with Rhodamine B (Sigma-Aldrich), while pSi was conjugated with Dylight488 (Invitrogen) [32]. The blending of PLGA-pSi and collagen was also validated through FTIR (Nicolet 6700 FT-IR Spectrometer).

#### 4.2.5. Pore Size, Porosity and Swelling

1 mm thick sections of the scaffolds were imaged with fluorescence microscopy (Nikon Eclipse Ti equipped with a Hamamatsu Orca Flash 2.8 digital camera), and the pore are determined via an automated measurement tool of the NIS-Element software (Nikon). The volumes of the scaffolds ( $V_s$ ) were measured from the scaffold geometry (cylinders of 5 mm in diameter and x 1 mm height). The volume of the pores was calculated by an ethanol infiltration method [33]. The volume of the pores was defined as in Equation:  $V_p = (W_e - W_0)/\rho_e$ , where  $W$  is scaffold's weight before ( $W_0$ ) and after incubation in ethanol ( $W_e$ ), and  $\rho_e$  (0.789 mg mL<sup>-1</sup>) represents the ethanol density at room temperature. The porosity of the

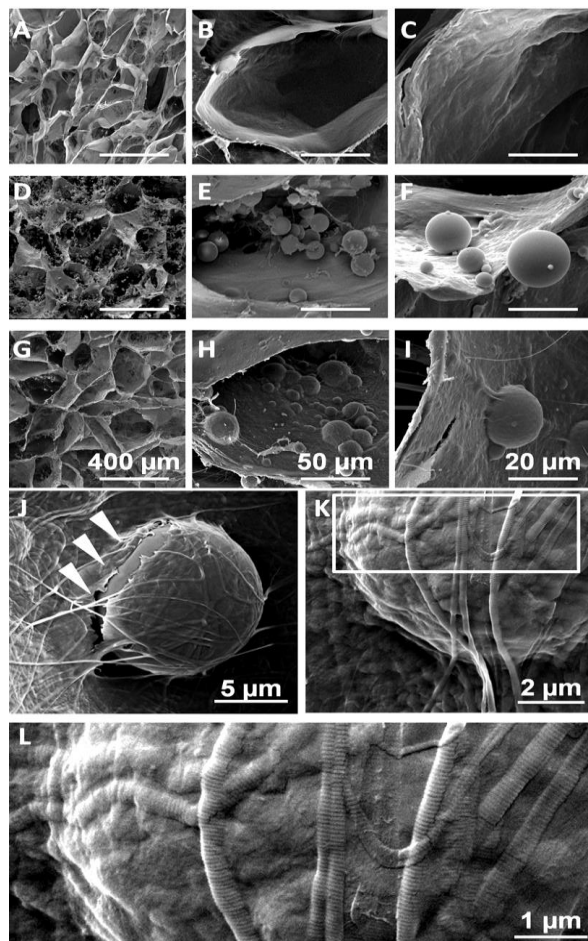


**Figure 4.2 - Scaffold integrated with PLGA-pSi microspheres. (A, B, C) Scanning electron microscopy images at different magnifications of control collagen scaffold (CTRL); (D, E, F) scaffold with PLGA-pSi adsorbed (ADS) on the surface and (G, H, I) with PLGA-pSi integrated (INT). (J) Type I collagen created a coating on the microspheres, indicated by the arrows, (K, L) while preserving collagen ultrastructure.**

scaffolds was calculated according to Equation  $P = V_p/V_s \cdot 100\%$ . To determine the PBS uptake property, the completely dried scaffolds were weighted and afterwards incubated in PBS at 37 °C. The hydrated scaffolds were taken out at the desired time intervals, wiped superficially with a filter paper to remove the surface water, and weighed (Ww). The value is expressed as means  $\pm$  SD (n = 5). The uptake ratio was defined as swelling %, as in Equation  $Sw\% = (Ww - Wd)/Wd \cdot 100$ .

#### 4.2.6. PLGA-pSi Integration Assessment

PLGA-pSi confinement stability over time was investigated incubating the CTRL, ADS and INT scaffolds (5 per group) in PSB at 37°C in mild mixing (100 rpm). Particle loss was quantified counting the fluorescently labeled microspheres (Rhodamine B) through the automated counting tool of the NIS-Element Software (Nikon) of the fluorescence microscope, collecting the PBS and substituting it with fresh one at defined time points, up to 2 weeks. Also, other 5 scaffolds, with the same formulation were used to assess PLGA-pSi distribution in ADS and INT.

#### 4.2.7. Loading of 488-BSA and 680-BSA into APTES modified pSi particles

488-BSA and 680-BSA (FITC-BSA, Sigma-Aldrich; Dylight680-BSA, Invitrogen) solutions (10 mg/mL) were prepared by dissolving the BSA powder in DI water.  $2 \times 10^8$  APTES modified particles were immersed into the 488-BSA (Sigma-Aldrich) and 680-BSA (Invitrogen) solution (500  $\mu$ L) respectively. The suspensions were mixed at 37 °C for 2 h, to allow proteins loading in the pores of the pSi. The particles were recovered by centrifugation at 4000 rpm and washed three times with PBS to remove the 488-BSA or 680-BSA adsorbed on the surface. The particles were then lyophilized overnight. The amount of protein loaded was measured by the difference between the protein concentrations of the stock solution and of the supernatant using SpectraMax M2 spectrophotometer (Molecular Devices) at 493/520 nm and 680/715 nm to quantify 488-BSA and 680-BSA, respectively.

#### 4.2.8. Loaded pSi encapsulation in PLGA-pSi

BSA-loaded pSi particles were coated with PLGA by a modified S/O/W emulsion method, as described above. Briefly,  $2 \times 10^8$  488-BSA and 680-BSA loaded pSi were dispersed, by sonication, in PLGA (50:50) (LACTEL) dissolved in DCM (375  $\mu$ L) (Sigma-Aldrich) (50 mg/ml and 200 mg/mL). Thus, two sets of PLGA-pSi with different PLGA coating were obtained as follow: 5 wt% (LD) and 20 wt% PLGA in DCM (HD). A quantitative

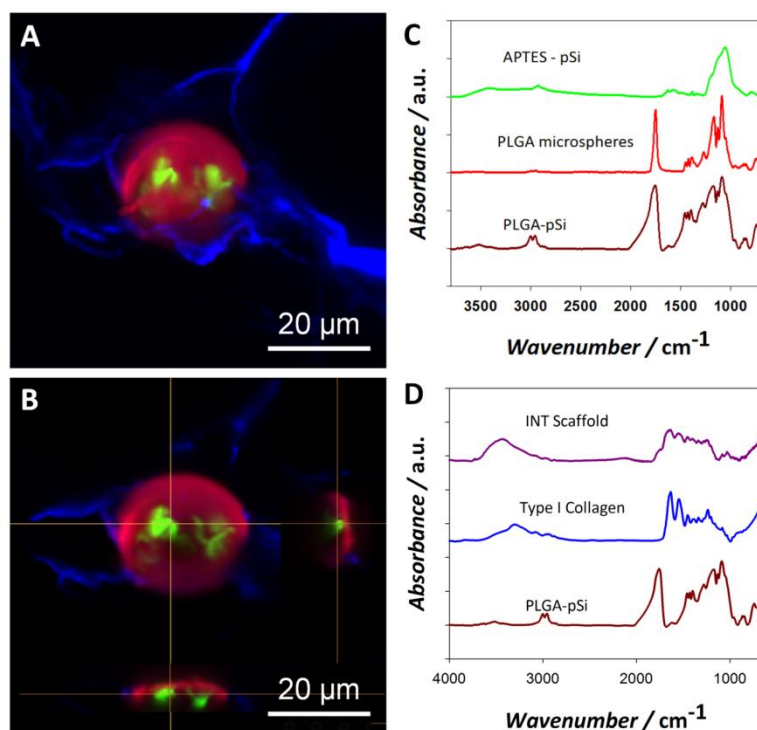


**Figure 4.3 - Qualitative analysis of PLGA-pSi blending with collagen matrix. (A) 3D reconstruction of confocal microscopy images illustrating PLGA-pSi integrated in the collagen scaffold and completely wrapped by collagen (collagen: blue; PLGA: red; pSi: green); (B) sagittal view showing pSi encapsulated within PLGA and coated by the collagen matrix. (C) FTIR patterns of the multiscale components of PLGA-pSi and (D) of the functionalized scaffold.**

characterization to assess the PLGA and pSi content in the two formulations (LD and HD) was performed via thermogravimetric analysis (TA Instruments Model Q600), with a heating ramp of 5°C/minute, from 25°C to 500°C.

#### 4.2.9. Bi-layered BSA-loaded scaffold fabrication

PLGA-pSi loaded with 488- or 680- BSA were dispersed in 1 mL of DI water and added to separate crosslinked collagen slurries (as described above), mixed and finally centrifuged at 4000 rpm in a Legend X1R Centrifuge (Thermo Scientific) for 5 minutes. Through layer-by-layer assembly the two collagen slurries were piled on to each other, in a metallic mold. Finally, a monolithic scaffold was generated through freeze-drying process as described above. Scaffold's morphology was characterized by SEM, fluorescence and confocal laser microscopy.

#### 4.2.10. Evaluation of 488- and 680- BSA in vitro Release

As a control, LD and HD were dispersed in phosphate buffer saline (PBS) (20 mL) at 37 °C. Also by-layered scaffolds ADS and INT were immersed in PBS in glass bottles as well as CTRL, at 37°C, and mixed at 100 rpm. At predetermined time intervals, the suspension was centrifuged (4500 rpm; 5 min), and 10% of the total volume of supernatant (2 mL) was collected, and replaced with fresh PBS, up to 50 days. The release was quantified by SpectraMax M2 spectrophotometer (Molecular Devices) at a wavelength of 493/520 nm and 680/715 nm to quantify 488-BSA and 680-BSA respectively. Three replicates for each experimental group were utilized.

#### 4.2.11. Statistical analysis

The number of samples used in each experiment is noted in the text of the experimental section. Dependent variables are expressed as means  $\pm$  SD. The differences in the means were tested using ANOVA and Student T-test to check for statistical significance ( $P < 0.05$ ).

### 4.3. Results and Discussion

#### 4.3.1. Nano- and Micro-Patterning of the Scaffold

Nanostructured porous silicon particles (pSi) have been chosen as the core of the delivery systems for their biocompatibility [34], controllable biodegradation [22], high porosity (51%) and thus surface area [29], that allow for the storage and preservation of high amounts of different payloads (Figure 4.1A, B) [16, 32]. The ability to

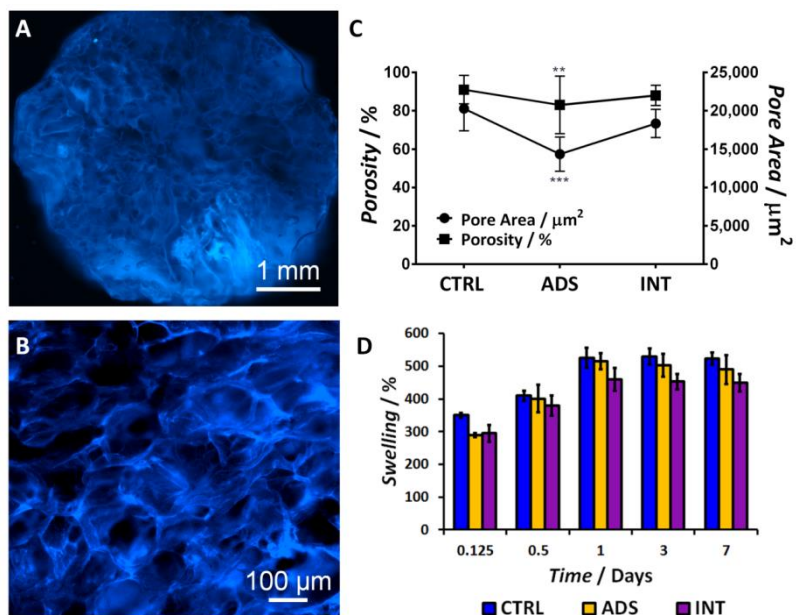


**Figure 4.4 - Characterization of blended scaffolds. (A) Fluorescent image of the entire collagen scaffold at low and (B) high magnification used for pore area calculation. (C) Porosity and pore area of scaffolds adsorbed or integrated with PLGA-pSi compared to a control scaffold. (D) Swelling characteristics comparing control, adsorbed (ADS), and integrated (INT) collagen scaffolds over time.**

tailor the physicochemical properties of porous silicon at the nano- and micro-scale confers versatility to this material [29]. Also, their preparation method allows for the fabrication of highly reproducible, monodisperse particles, favoring their loading and encapsulation [23, 30, 32]. pSi shells were fabricated with an average diameter of 3.2  $\mu\text{m}$ , 600 nm shell thickness. To improve loading efficiency, pSi surface was modified with (3-Aminopropyl)triethoxysilane (APTES) that increases its hydrophilicity by introducing amine groups on the surface of the particles [30].

#### 4.3.2. *pSi Encapsulation in PLGA Microspheres*

Although silicon revealed a valuable materials to develop delivery systems able to load, store and release multiple proteins, their degradation in physiologic conditions resulted very fast (in the order of hours) [22], and thus not compatible with tissue healing, which take place from several weeks, up to months. The creation of composites, based on pSi and polymers, contributes to enhance material stability and thus prolong release kinetics.

PLGA can be produced in different molecular weights and copolymer ratios, yielding materials with tunable degradation rates [35, 36]. To obtain the stable and efficient blending with pSi in the organic solvent and the following integration with collagen in an aqueous solution, we used the 50:50 PLGA co-polymer that resulted in the optimal surface charge and polarity. pSi were encapsulated in the PLGA shell through a modified double emulsion method [23]. The use of monodisperse pSi was key to optimize PLGA-pSi size distribution, as confirmed by scanning electron microscopy (SEM) (Figure 4.1C), where PLGA-pSi displayed an average size of  $11 \pm 3 \mu\text{m}$  in diameter (Figure 4.1D, blue data set), with sizes ranging between 3  $\mu\text{m}$  to 25  $\mu\text{m}$ , with a reduction of the size range of the 50% compared to previous reports [37]. Optical microscopy demonstrated that median number of 3 ( $\pm 0.2307$ ) pSi (Figure 4.1D, yellow data set) were encapsulated in the PLGA microsphere (Figure 4.1E, F). The overall improvement of PLGA-pSi fabrication and pSi dispersion through the microspheres was crucial to ensure a more homogenous release of payload.

#### 4.3.3. *Collagen Functionalization with PLGA-pSi*

Collagen type I was chosen because it is the most abundant structural element in connective tissues [38, 39], where its hierarchically organized structure plays a prominent role in maintaining the biologic and structural integrity of the ECM [40]. Exploiting collagen's ability to dock and blend with PLGA, we optimized a procedure to stably integrate PLGA-pSi within the scaffold's matrix. To demonstrate the spatial confinement of the microspheres in the scaffold we compared three groups: (i) blank scaffolds (CTRL); (ii) scaffolds with adsorbed PLGA-pSi microspheres (ADS), included as current standard; (iii) scaffolds with PLGA-pSi integrated in the collagen matrix (INT). Figure 4.2 illustrates the morphology and microstructure of the CTRL (Figure 4.2A, B, C), ADS (Figure 4.2D, E, F) and INT (Figure 4.2G, H, I) scaffolds. The PLGA-pSi fully integrated within the collagen matrix of INT scaffolds, while in the ADS scaffolds the microspheres were simply adsorbed on the pore walls. In fact, the collagen matrix formed a consistent coating surrounding the PLGA-pSi, as illustrated in Figure 4.2J, where a high voltage electron beam during SEM imaging was used to damage the collagen coating and expose the PLGA-pSi. The overall morphology of the scaffolds and their pore shape and size were preserved in both ADS and INT scaffolds. Similarly, PLGA-pSi did not affect the structure of the collagen fibrils which maintained the characteristic D-band of approximately 67 nm (Figure 4.2K, L) [41, 42]. Thus, herein we developed a method of scaffold functionalization with PLGA-pSi which preserves such asset, and which is also exploited as a further level of control over the temporal and spatial control over the reporter proteins.

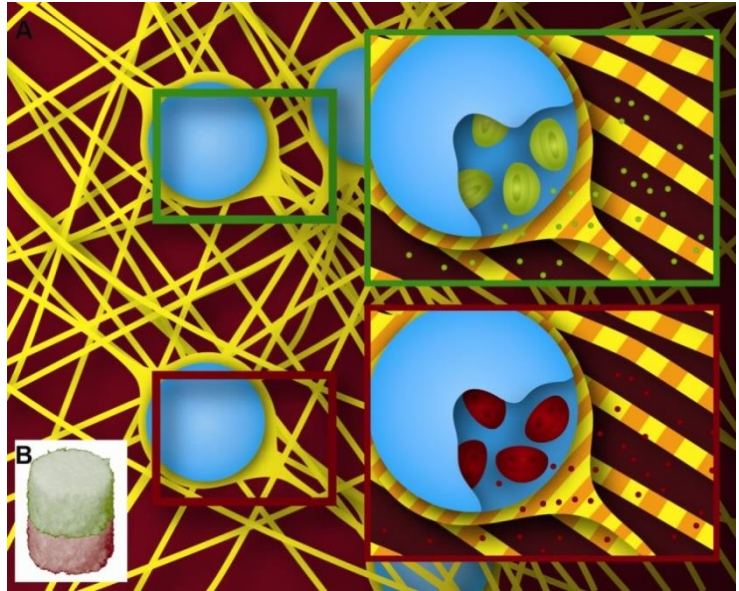
**Table 1.** Comparison of the characteristics of ADS and INT respect to their controls.

	CTRL	ADS	INT
Pore Area [ $\mu\text{m}^2$ ]	20.3·10 <sup>3</sup>	14.3·10 <sup>3</sup>	18.4·10 <sup>3</sup>
Porosity [%]	91	83	88
PLGA-pSi Diameter [ $\mu\text{m}$ ]	11 $\pm$ 3	10 $\pm$ 4	10 $\pm$ 3
Mean Distance of PLGA-pSi [ $\mu\text{m}$ ]	/	70 $\pm$ 21	46 $\pm$ 7

#### 4.3.4. Characterization of PLGA-pSi Integration in Collagen Scaffolds

To confirm the complete embedding of the PLGA-pSi within the collagen matrix, confocal laser microscopy was used to acquire Z-stacks, and reconstruct the 3D volume around the integrated microsphere (Figure 4.3A). As exposed in the orthogonal views in Figure 4.3B, the fibers of the collagen (blue) completely enclosed the PLGA-pSi (red and green, respectively). Pore wall's thickness was measured from the Z-stack acquisitions, and appeared to be in the range of 10-15  $\mu\text{m}$  in the control scaffold. By embedding PLGA-pSi of  $\sim$ 11  $\mu\text{m}$ , in the collagen matrix we provided a  $\leq$  2  $\mu\text{m}$  thick collagen coating of PLGA-pSi. Reaching a more homogenous distribution of PLGA-pSi along the pore walls, as well as the consistent thickness of the collagen coating on all microspheres, was crucial for a homogenous release from the bulk scaffold. Microspheres' blending with the collagen matrix

was analyzed through Fourier transformed infrared spectroscopy (FTIR). CTRL, INT scaffold and ADS scaffold have been all freeze dried following the same procedure, previous FTIR analysis. FTIR spectra of PLGA-pSi microspheres resembled a hybrid spectra, resulting by the addition of the peaks of pSi and PLGA, confirming the formation of a pSi-PLGA composite (Figure 4.3C). In the INT scaffolds (Figure 4.3D), a pattern with broader FTIR peaks, especially in the regions that correspond to amine groups (3500-3300  $\text{cm}^{-1}$ , stretching) [43], and carbonyl groups (1750-1735  $\text{cm}^{-1}$ , stretching) can be observed [44], suggesting the interaction of the carbonyl groups on the surface of the PLGA-pSi microspheres with the amine groups of the collagen. A moderate contribution in the broadening of the Amide I peaks of INT scaffold by physisorbed water was excluded for the absence of any broadening in the correspondent peak in CTRL. On the contrary, the Amide I peak intensity and area in the range 3000-3600  $\text{cm}^{-1}$  (OH- stretching) are comparable in both samples, and do not appear to be affected by the presence of physisorbed water. On the contrary, the FTIR spectra of ADS scaffolds displayed either the spectrum of pure type I collagen or of PLGA-pSi, depending on the spot analyzed (10 random spots were evaluated). Analysis of the mean pore size and surface area confirmed the anisotropic structure of all



**Scheme 1 - Schematic showing: (A) the setting of LD PLGA-pSi (PLGA: blue; pSi: green) and HD PLGA-pSi (pSi: red), in the collagen fibers (yellow), (B) in the bi-layered collagen scaffold.**

scaffolds (Figure 4.4A and B) [31, 45]. CTRL presented a porosity of 91%, with a mean pore area of  $20 \cdot 103 \mu\text{m}^2$ , and with a diameter in the range of 250-350  $\mu\text{m}$ . The changes in the average porosity and pore area of ADS and INT, respect to CTRL, are shown in Figure 4C. While the integration of PLGA-pSi did not result in a significant decrease of the porosity in the INT scaffolds, the pore size and porosity of ADS scaffolds were significantly different from CTRL. This discrepancy was attributed to the obstruction of the pores by the adsorbed microspheres. The swelling of both ADS and INT scaffolds was slightly lower than the control scaffold, though not significantly altered, and demonstrated that the integration of PLGA-pSi in the collagen matrix did not affect its swelling, a key feature for both the mechanical and biological properties of the scaffold (Figure 4.4D). Pore size and porosity of the scaffold were tuned during the freeze drying process through the adjustment of the freezing temperature, heating ramp, and the content of water in the collagen slurry [46].

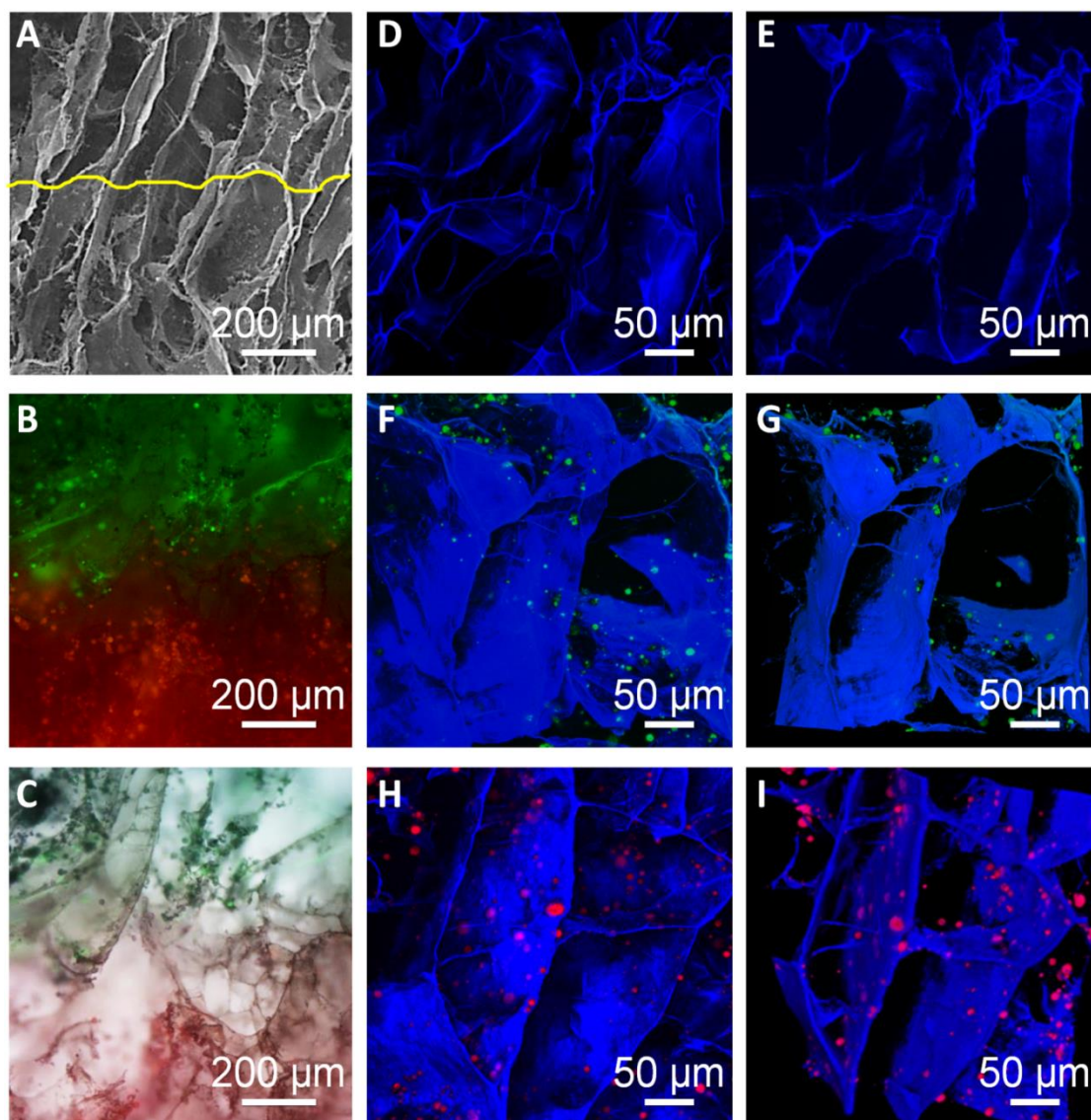


**Figure 4.5 - PLGA-pSi functionalized bi-layered scaffold. (A) SEM, (B) fluorescent and (C) bright field images, merged with fluorescence, of the interface between the two layers of the collagen scaffold functionalized with LD loaded with 488-BSA (green layer) or HD loaded with 680-BSA (red layer). (D, E) Maximum intensity projections and 3D reconstruction of CTRL, (F, G) LD INT layer and (H,I) HD INT layer, respectively.**

None of these features were affected by the incorporation of the PLGA-pSi microspheres. Confocal imaging of the scaffolds allowed the identification and characterization (e.g., diameter, distribution, and relative distance) of individual microspheres within scaffolds (NIS-Elements software, Nikon). The density of microspheres in the ADS and INT scaffolds was  $2 \cdot 10^3 (\pm 24)$  per  $\text{mm}^3$ . The type of integration did not change the size of PLGA-pSi confirming the stability of the microspheres throughout the integration process. The mean distance between PLGA-pSi was calculated automatically in ten random positions on the Z plane. For INT scaffolds, the mean distance between neighboring PLGA-pSi was 46  $\mu\text{m}$ . The moderate standard deviation supports the homogenous distribution of microspheres within the INT scaffolds. On the other hand ADS scaffolds, possibly due to the uncontrolled distribution and agglomeration of PLGA-pSi, exhibited mean distances of 70  $\mu\text{m}$ , correlating with a much higher standard deviation. All these data are summarized in Table 1. Through the tuning of the design parameters (PLGA-pSi size, density, number of PLGA-pSi per layer, mean distance between microspheres, etc.), it is possible to reverse engineer scaffolds with pre-defined parameters, to allow for the customization of scaffolds with defined geometries, release patterns and kinetics.

The stability of the integration of PLGA-pSi in the scaffold was tested comparing the retention of microspheres from ADS and INT scaffolds. After two soaking steps, ADS scaffolds lost three times more PLGA-pSi than INT (15% and 5% respectively). At two weeks 94% of PLGA-pSi was lost from the ADS scaffolds, compared to only 17 % lost from INT, exhibiting an almost 6 fold increase in retention. The role of the collagen in retaining scaffold's nano- and micro- components and features (e.g. functional groups, hierarchical architecture, pore size, swelling), ultimately preserving the entire macro-structure, enabled the stable and homogeneous confinement of PLGA-pSi. All these results confirmed that PLGA-pSi became part of the scaffold, when integrated to the collagen at the slurry state, during the last steps of fibers self-assembling. All these data together demonstrated that this approach of functionalization represents a more efficient alternative to particle adsorption in collagen sponges, which lack of any control over particles' distribution and retention.

#### 4.3.5. *Macro-patterning of the Scaffold with PLGA-pSi*

##### 4.3.5.1. Spatial Patterning of the Reporter Protein

A bi-layered scaffold for the staged release of 488-BSA and 680-BSA from each individual layer was fabricated according to Scheme 1. 488-BSA was encapsulated in a PLGA-pSi with a low-density polymer (LD) coating to achieve a faster release rate; while 680-BSA was incorporated in high-density polymers (HD) for a slower release rate. Composites were characterized also by Thermo-Gravimetric Analysis to confirm the different content of polymer and silicon. Quantification of BSA loading revealed that  $12 \pm 3 \mu\text{g}$  of 488- or 680-BSA was accommodated into 106 pSi exhibiting no appreciable loss of BSA during encapsulation with PLGA. The high loading capacity of the pSi core facilitates the prolonged release of proteins and is amenable to the concurrent loading of multiple bioactive factors. This is particularly relevant as most clinical applications require hundreds of nanograms of bioactive factors per day to achieve an effective dose [47, 48]. The structure of the bi-layered scaffold and of each layer is depicted in Figure 4.5. PLGA-pSi microspheres were completely enclosed within the collagen layer forming the pore walls. The interface between the two layers exhibited no delamination and near-perfect integration (see dotted line in Figure 4.5A). The optimized freeze-drying process led to a monolithic scaffold showing structural continuity between different layers (Figure 4.5B and C), and devoid of signs of delamination under physiological conditions. When the two layers are stacked at their slurry state the exchange of fibers between the unstructured collagen molecules allow the interweaving of the two layers. The controlled freezing and heating ramp, triggered the directional growth of water crystals from the bottom to the top of the slurry, resulting in further integration and stability of the two layers. This fabrication technique allowed for the

creation of several intra-scaffold compartments in which the confinement of the PLGA-pSi occurred in all dimensions. The ability to accomplish the 3D patterning of the scaffold is particularly relevant for applications in interface tissue engineering, where there is the need to simultaneously mimic the architecture and biochemical environments found at the interface of different but contiguous tissues [49].

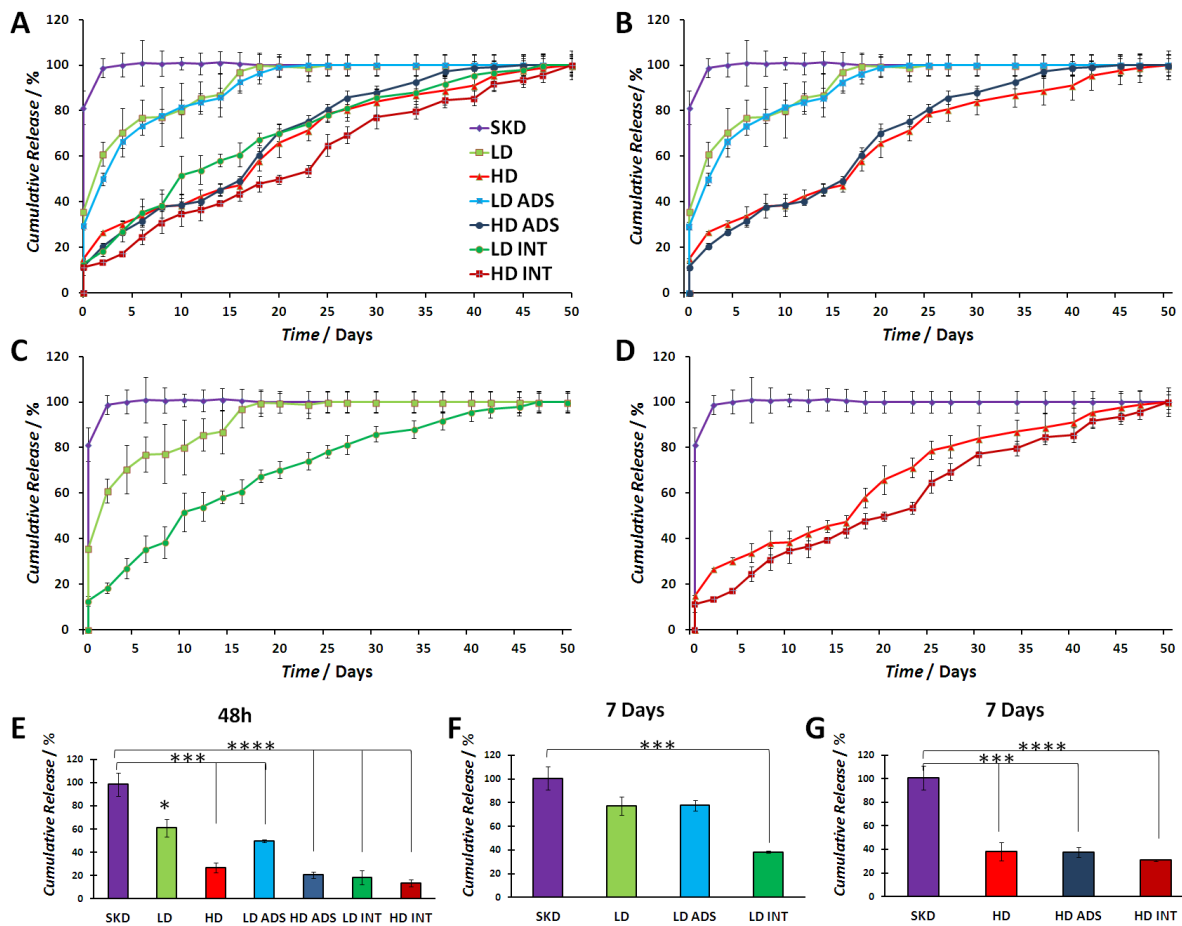


**Figure 4.6 - Release kinetics from bi-layered functionalized scaffolds. (A) Overall results of all the groups investigated. (B) Release of BSA from SKD, LD PLGA-pSi and LD PLGA-pSi ADS. (C) Comparison of BSA release from LD PLGA-pSi and INT. (D) Comparison of BSA release from HD PLGA-pSi and INT. The statistical significance between the amounts of BSA release over time per each group is marked with asterisks ( $p < 0.05$ ) for the time points at (E) 48h and (F,G) at 7 days.**

#### 4.3.5.2. Temporal Patterning of the Reporter Proteins: In Vitro Release

To investigate the contribution of the collagen scaffold to the release kinetics of BSA from LD and HD PLGA-pSi, we investigated four experimental groups: (1) LD and HD; (2) 488- and 680-BSA soaked in a bilayered collagen scaffold (SKD); (3) LD and HD adsorbed in a bi-layered (LD/HD ADS); (4) LD and HD integrated in a bi-layered scaffold (LD/HD INT). The release kinetics of each experimental group are reported in Figure 4.6A. For clarity, a single release profile was reported for SKD, as the release kinetics for 488- and 680-BSA were

almost identical. As expected, the SKD group showed a burst release, up to 80% lost within the first 12 hours. In addition, LD exhibited a considerably faster release rate compared to HD with complete release plateauing at day 18 compared to day 50 for HD samples. Similar release kinetics were found for both LD and HD and the corresponding LD/HD ADS (Figure 4.6B). The results suggested a negligible contribution of the collagen scaffold to the release kinetics when the microspheres were adsorbed on its surface. Considering the loss of PLGA-pSi from ADS, presented in the supporting information session, it is reasonable to believe that the similar release kinetics of free LD/HD and LD/HD ADS could be attributed to the massive loss of PLGA-pSi (82.5%) from the ADS scaffolds within the first two weeks. The release from LD/HD INT was significantly delayed compared to all other groups (Figure 4.6C), confirming the contribution of the collagen matrix in modulating the release kinetics by creating an additional coating layer over the microspheres. As expected, the release of BSA from HD INT scaffold exhibited a slower release rate compared to the corresponding free HD (Figure 4.6D). The quantification of the total mass of BSA released at the individual time points revealed that significant amounts of BSA were discharged by LD SKD and HD INT as early as 48 hours (5x and 7x respectively) (Figure 4.6E). After seven days, free and LD ADS demonstrated similar cumulative release (~78%), while INT released 50% and 35% of BSA from LD and HD respectively (Figure 4.6F). LD and HD INT scaffolds showed substantially different kinetics in the two layers (HD INT release rate being 50 percent slower than LD INT). While these results confirm the creation of temporal gradients of proteins, the observation that the BSA released from each layer, remained entrapped within its own layer, proved the spatial confinement of these protein regardless of their release during time. All together, these studies demonstrated that the integration of microparticles within the collagen scaffold matrix played an important role in controlling the staged release and spatial retention of two reporter proteins within the two separate compartments of the scaffold.

#### **4.4. Conclusions**

With this study we present a novel approach for the creation of multiscale biomimetic scaffold, capable of generating spatial and temporal protein patterns. The result was achieved by leveraging the natural ability of the collagen matrix to interact with PLGA-pSi microspheres, effectively constructing a simple and tunable system for various tissue engineering applications. Optimizing the synthesis of monolithic multilayered collagen scaffolds, we stably integrated PLGA-pSi within the collagen matrix without altering collagen's nano- and micro- structure. The results demonstrate that this modular approach to fabricate multi-compartment scaffolds allow for tissues mimicry at a multiscale level. At the nanoscale, the type I collagen conserved its fibrillar structure and typical D-bands appearance, while the pSi nanostructure allowed the loading and release of reporter proteins. At the microscale, the PLGA coating of pSi created a composite delivery platform for the tunable release of the reporter proteins, while the collagen coating on PLGA-pSi enabled for their spatial confinement in the scaffold. Finally, at the macroscale, all these elements combined, without altering the feature of the material, such as pore size, porosity and swelling upon PLGA-pSi integration. pSi, PLGA and collagen boundaries contributed to accomplishing the temporal patterning of the proteins in the multi-layered scaffold, through a triple controlled release, enabling for the zero-order release kinetics of reporter protein up to 50 days. The release of controlled amounts of drugs over long periods of time would favor on-scaffold regeneration while avoiding adverse effects due to the diffusion of high doses of therapeutic molecules in the tissues surrounding the scaffold. By grafting distinct sets of PLGA-pSi composites, one can envision the creation of multiple unique biochemical niches within a 3D biomimetic scaffold, while protecting the payload and the delivery system from the cellular and enzymatic attach of cells of the immune system (mainly macrophages) and from the surgical procedures (washing, debridement, bleeding, fluid aspiration) applied during the implantation of the scaffold which challenge the integrity of the material.

#### 4.5. References:

1. Stevens, M.M. and J.H. George, *Exploring and engineering the cell surface interface*. Science, 2005. **310**(5751): p. 1135-1138.
2. Oliveira, M.B., et al., *Combinatorial On-Chip Study of Miniaturized 3D Porous Scaffolds Using a Patterned Superhydrophobic Platform*. Small, 2012.
3. Lutolf, M. and J. Hubbell, *Synthetic biomaterials as instructive extracellular microenvironments for morphogenesis in tissue engineering*. Nat Biotechnol, 2005. **23**(1): p. 47-55.
4. Ben-David, D., et al., *Low dose BMP-2 treatment for bone repair using a PEGylated fibrinogen hydrogel matrix*. Biomaterials, 2013.
5. Madry, H., et al., *Transforming Growth Factor Beta-Releasing Scaffolds for Cartilage Tissue Engineering*. Tissue Eng. Pt B: Rev, 2013.
6. Jakobsen, R.B., et al., *Chondrogenesis in a hyaluronic acid scaffold: comparison between chondrocytes and MSC from bone marrow and adipose tissue*. Knee Surgery, Sports Traumatology, Arthroscopy, 2010. **18**(10): p. 1407-1416.
7. Wang, C.-C., et al., *A highly organized three-dimensional alginate scaffold for cartilage tissue engineering prepared by microfluidic technology*. Biomaterials, 2011. **32**(29): p. 7118-7126.
8. Schultz, G.S. and A. Wysocki, *Interactions between extracellular matrix and growth factors in wound healing*. Wound Repair Regen., 2009. **17**(2): p. 153-162.
9. Geiger, M., R.H. Li, and W. Friess, *Collagen sponges for bone regeneration with rhBMP-2*. Adv Drug Del Rev, 2003. **55**(12): p. 1613-1629.
10. Carragee, E.J., E.L. Hurwitz, and B.K. Weiner, *A critical review of recombinant human bone morphogenetic protein-2 trials in spinal surgery: emerging safety concerns and lessons learned*. Spine J., 2011. **11**(6): p. 471-491.
11. Burkus, J.K., et al., *Is INFUSE Bone Graft Superior to Autograft Bone? An Integrated Analysis of Clinical Trials Using the LT-CAGE Lumbar Tapered Fusion Device*. J Spinal Disord Tech, 2003. **16**(2): p. 113-122.
12. Santo, V.E., et al., *Controlled Release Strategies for Bone, Cartilage, and Osteochondral Engineering—Part II: Challenges on the Evolution from Single to Multiple Bioactive Factor Delivery*. Tissue Eng. Pt. B-Rev., 2013.
13. Choi, D.H., et al., *Dual Growth Factor Delivery Using Biocompatible Core-Shell Microcapsules for Angiogenesis*. Small, 2013.
14. Tabata, Y., *Tissue regeneration based on growth factor release*. Tissue Eng., 2003. **9**(4, Supplement 1): p. 5-15.
15. Drinnan, C.T., et al., *Multimodal release of transforming growth factor- $\beta$ 1 and the BB isoform of platelet derived growth factor from PEGylated fibrin gels*. J. Controlled Release, 2010. **147**(2): p. 180-186.
16. Tasciotti, E., et al., *Mesoporous silicon particles as a multistage delivery system for imaging and therapeutic applications*. Nat Nanotechnol, 2008. **3**(3): p. 151-157.
17. Sun, W., et al., *Nano-to Microscale Porous Silicon as a Cell Interface for Bone-Tissue Engineering*. Advanced materials, 2007. **19**(7): p. 921-924.
18. Sun, W., et al., *Nano- to Microscale Porous Silicon as a Cell Interface for Bone-Tissue Engineering*. Advanced materials, 2007. **19**(7): p. 921-924.
19. Anglin, E.J., et al., *Porous silicon in drug delivery devices and materials*. Advanced drug delivery reviews, 2008. **60**(11): p. 1266-1277.
20. Whitehead, M.A., et al., *High-porosity poly ( $\epsilon$ -caprolactone)/mesoporous silicon scaffolds: calcium phosphate deposition and biological response to bone precursor cells*. Tissue Engineering Part A, 2008. **14**(1): p. 195-206.
21. Fan, D., et al., *The role of nanostructured mesoporous silicon in discriminating in vitro calcification for electrospun composite tissue engineering scaffolds*. Nanoscale, 2011. **3**(2): p. 354-361.
22. Martinez, J.O., et al., *Engineering multi-stage nanovectors for controlled degradation and tunable release kinetics*. Biomaterials, 2013. **34**(33): p. 8469-8477.
23. Fan, D., et al., *Mesoporous Silicon-PLGA Composite Microspheres for the Double Controlled Release of Biomolecules for Orthopedic Tissue Engineering*. Adv. Funct. Mater., 2012. **22**(2): p. 282-293.
24. Spiller, K.L., et al., *A novel method for the direct fabrication of growth factor-loaded microspheres within porous nondegradable hydrogels: Controlled release for cartilage tissue engineering*. J. Controlled Release, 2012. **157**(1): p. 39-45.
25. Son, J.S., et al., *Porous hydroxyapatite scaffold with three-dimensional localized drug delivery system using biodegradable microspheres*. J Controlled Release, 2011. **153**(2): p. 133-140.

26. Wei, G., et al., *The enhancement of osteogenesis by nano-fibrous scaffolds incorporating rhBMP-7 nanospheres*. Biomaterials, 2007. **28**(12): p. 2087-2096.
27. Abbas, A.K., A.H. Lichtman, and S. Pillai, *Basic immunology: functions and disorders of the immune system*. 2012: Saunders WB.
28. Maynes, R., *Structure and function of collagen types*. 2012: Elsevier.
29. Chiappini, C., et al., *Tailored Porous Silicon Microparticles: Fabrication and Properties*. ChemPhysChem, 2010. **11**(5): p. 1029-1035.
30. De Rosa, E., et al., *Agarose surface coating influences intracellular accumulation and enhances payload stability of a nano-delivery system*. Pharm Res, 2011. **28**(7): p. 1520-30.
31. Tampieri, A., et al., *Design of graded biomimetic osteochondral composite scaffolds*. Biomaterials, 2008. **29**(26): p. 3539-46.
32. Parodi, A., et al., *Synthetic nanoparticles functionalized with biomimetic leukocyte membranes possess cell-like functions*. Nat Nanotechnol, 2012.
33. Tan, H., et al., *Gelatin/chitosan/hyaluronan scaffold integrated with PLGA microspheres for cartilage tissue engineering*. Acta Biomater., 2009. **5**(1): p. 328-337.
34. Martinez, J.O., et al., *Evaluation of Cell Function Upon Nanovector Internalization*. Small, 2013. **9**(9-10): p. 1696-1702.
35. Danhier, F., et al., *PLGA-based nanoparticles: an overview of biomedical applications*. J. Controlled Release, 2012. **161**(2): p. 505-522.
36. Anderson, J.M. and M.S. Shive, *Biodegradation and biocompatibility of PLA and PLGA microspheres*. Adv Drug Deliv Rev, 1997. **28**(1): p. 5-24.
37. Fan, D., et al., *Mesoporous Silicon-PLGA Composite Microspheres for the Double Controlled Release of Biomolecules for Orthopedic Tissue Engineering*. Advanced Functional Materials, 2012. **22**(2): p. 282-293.
38. Badyal, S.F., D.O. Freytes, and T.W. Gilbert, *Extracellular matrix as a biological scaffold material: structure and function*. Acta Biomater., 2009. **5**(1): p. 1-13.
39. Cheema, U., M. Ananta, and V. Mudera, *Collagen: applications of a natural polymer in regenerative medicine*. Regenerative Medicine and Tissue Engineering—Cells and Biomaterials. Eberli D, Ed. In Tech, 2011: p. 287-300.
40. H. Lodish, A.B., S.L. Zipursky, P. Matsudaira, D. Baltimore, J. Darnell, *Molecular Cell Biology*, ed. N.Y.W.H. Freeman. 2000.
41. Erickson, B., et al., *Nanoscale structure of type I collagen fibrils: Quantitative measurement of D-spacing*. Biotech. J., 2013. **8**(1): p. 117-126.
42. Barker, T.H., *The role of ECM proteins and protein fragments in guiding cell behavior in regenerative medicine*. Biomaterials, 2011. **32**(18): p. 4211-4214.
43. Payne, K. and A. Veis, *Fourier transform IR spectroscopy of collagen and gelatin solutions: deconvolution of the amide I band for conformational studies*. Biopolymers, 1988. **27**(11): p. 1749-1760.
44. Camacho, N.P., et al., *FTIR microscopic imaging of collagen and proteoglycan in bovine cartilage*. Biopolymers, 2001. **62**(1): p. 1-8.
45. Courtney, T., et al., *Design and analysis of tissue engineering scaffolds that mimic soft tissue mechanical anisotropy*. Biomaterials, 2006. **27**(19): p. 3631-3638.
46. O'Brien, F.J., et al., *Influence of freezing rate on pore structure in freeze-dried collagen-GAG scaffolds*. Biomaterials, 2004. **25**(6): p. 1077-1086.
47. Gavenis, K., et al., *BMP-7-loaded PGLA microspheres as a new delivery system for the cultivation of human chondrocytes in a collagen type I gel: the common nude mouse model*. Int. J. Art. Org., 2010. **33**(1): p. 45-53.
48. Srouji, S., et al., *Slow-release human recombinant bone morphogenetic protein-2 embedded within electrospun scaffolds for regeneration of bone defect: in vitro and in vivo evaluation*. Tissue Eng. Pt. A, 2010. **17**(3-4): p. 269-277.
49. Seidi, A., et al., *Gradient biomaterials for soft-to-hard interface tissue engineering*. Acta Biomater., 2011. **7**(4): p. 1441-1451.

# CAMOUFLAGING OF DELIVERY SYSTEMS IN 3D BIOMIMETIC SCAFFOLDS

## 5.1. Introduction:

Biomaterials mimicking the structure and composition of the extracellular matrix (ECM) are capable of acting as inductive templates for the formation of site-specific functional tissues [7]. Collagen, the basic structural element for most connective tissues, plays a prominent role in maintaining the structural integrity of tissue architecture, and it has been successfully used in several applications of tissue engineering [1-3]. Collagen is a highly dynamic component of the ECM which contributes basic information for cell attachment [4], migration [5], organization [6] and macrophages have shown to favorably respond to it, contributing to collagen-based materials' integration [7]. This reciprocal interaction between cells and matrix is key for tissue regeneration and the consequent tissue homeostasis [8]. However, collagen alone lacks the ability to recapitulate the complexity of tissues' milieu, therefore the addition of bioactive factors is needed for the specific application [9]. The functionalization of biomimetic scaffolds with delivery systems [10] has become an attractive option for many approaches of regenerative medicine that require the in situ delivery of drugs and growth factors [11, 12]. Encapsulating therapeutic molecules in polymer particles offers considerable advantages, including tailoring of well controlled release kinetics, protection from degradation and temporo-spatial targeting [11, 13]. Unfortunately, these drug

delivery systems, in vivo, usually trigger the recruitment of cells of the immune system (e.g. neutrophils and macrophages)[14, 15] which may lead to an unwanted sequence of events, including acute and/or chronic response, foreign body reaction and fibrous tissue formation [16]. It has been established that macrophages appear in the site of the injury, in the early stages (1-3 days) [17-19]. Tissue remodeling following implantation is also associated with an increased macrophage activity [20]. The size [21], shape [22] and physico-chemical properties (rigidity, charge)[23, 24] of the material affect the

activation of internalization by macrophages and ultimately the intensity and duration of the inflammatory process. Avoiding early detection and phagocytosis of the delivery systems from engineered scaffolds is crucial to ensure the proper temporal and spatial control over the release of their payload. In fact, in order to obtain the desired outcome, it is fundamental that the therapeutic molecule is released with the proper kinetic and in the target tissue compartment to be effective. Poly(dl-lactide-co-glycolide acid (PLGA) microspheres are FDA approved delivery systems [25], that can be synthesized through simple and easily scalable processes [26]. They have also been integrated in scaffolds for tissue engineering to provide a further level of control in the release of the payload of interest [27]. However, when their diameter is below 10-15  $\mu\text{m}$  in size, they are efficiently

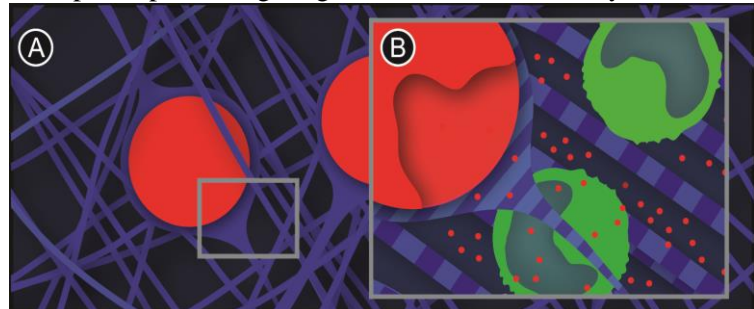


**Figure 5.1 - Schematic showing how the biomimetic scaffold functionalized with stealth microspheres for the release of proteins (A). Panel B shows how the collagen coating (blue) could prevent macrophages (green) from detecting the delivery systems (red) for the controlled release of proteins (red dots).**

internalized by phagocytic cells [18]. Recently, injectable polymer-based delivery systems have been coated with components of the ECM (i.e gelatin and collagen) [28], aiming at reducing the immune response and clearance from the body, while increasing payload stability [29]. According to these findings, we recently developed an innovative approach for the functionalization of 3D biomimetic scaffolds, by integrating MS in the pores' walls of a type I collagen scaffold, thus enabling spatial and temporal control over MS and their payload [11]. The hypothesis of this study is that by fully embedding MS below 5  $\mu\text{m}$  in a highly structured and fibrous collagen-based scaffold (camouflaging), it is also possible to prevent their early detection and clearance by macrophages. We also investigated whether such camouflage could efficiently reduce the production of key inflammatory molecules, while preserving the release kinetics of MS payload. Schematic in Figure 5.1 depicts the rationale of this study, showing how the collagen coating (blue) could act screening MS (red) to macrophages (green).

## 5.2. Materials and Methods:

### 5.2.1. MS synthesis:

PLGA 50:50 (LACTEL) was dissolved in dichloromethane (DCM) (Sigma-Aldrich) at a concentration of 100 mg/ml. Tetramethylrhodamine (TRITC) (Sigma-Aldrich) was added to 1 ml of PLGA in DCM, and mix at the PLGA solution at a concentration of 10  $\mu\text{g}/\text{ml}$ . The organic phase was homogenization at 6000 rpm with the aqueous solution of poly (vinyl alcohol) (PVA) (Fisher Scientific) (10 ml, 5 mg/ml) to synthesize MS with a diameter inferior to 5 $\mu\text{m}$ . The emulsions were dropped into an aqueous solution (50 mL) containing PVA (2.5 mg/ml). The resulting suspension was stirred for 6 h to allow the evaporation of the organic solvent. For the release study we fabricated MS loaded with Fluorescein isothiocyanate (FITC) – Bovine Serum Albumin (FITC-BSA) (Sigma Aldrich). FITC-BSA was mixed (1mg/ml) to the solution of PLGA in DCM, and the synthesis was carried out as reported above.

### 5.2.2. Scaffolds fabrication:

Type I collagen (Sigma-Aldrich) was dissolved in acetate buffer (pH 3.5). The resulting collagen gel (containing 1g of dry collagen) was precipitated by the addition of a solution of sodium hydroxide 0.1 M, to pH 5.5. The collagen slurry was washed three times with DI water. The collagen was cross-linked through dispersion for 48 h in a 1,4-butanediol diglycidyl ether (BDDGE) (Sigma-Aldrich) aqueous solution (2.5 mM) [14]. The cross-linked collagen was washed 3 times in DI water. The cross-linked collagen was suspended in DI water (5 mL), and 2 groups of collagen scaffolds were fabricated: integrated with MS (MS INT) or with MS simply adsorbed into the scaffold (MS ADS). MS INT scaffolds were fabricated blending MS (2 wt%) with cross-linked collagen. A dispersion of MS (3 mg/mL) in DI water was added during the fabrication of the scaffolds, at its slurry state. The material was freeze-dried with a controlled freezing ramp from 25  $^{\circ}\text{C}$  to -25  $^{\circ}\text{C}$  and a heating ramp from -25  $^{\circ}\text{C}$  to 25  $^{\circ}\text{C}$  in 50 min under vacuum conditions ( $P = 0.20$  mbar), and porous collagen scaffolds (20mm<sup>3</sup>) were produced. The same amount of MS was adsorbed on an unmodified collagen scaffolds, by soaking a collagen sponge in the particle suspension. These scaffolds were ultimately freeze-dried, as described. Cylindrical scaffolds of 8 mm in diameter and 1 mm thick were produced and characterized.

### 5.2.3. Macrophage seeding on MS INT and MS ADS:

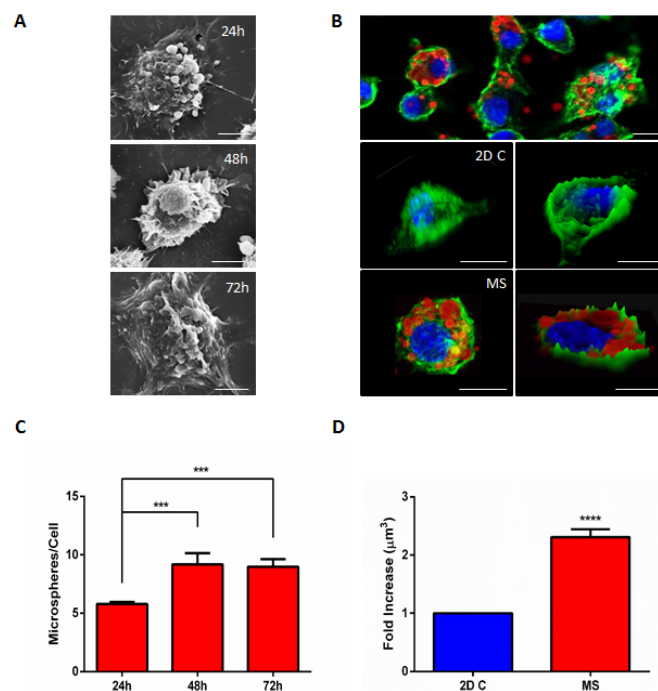


**Figure 5.2 - SEM images at 24, 48h and 72h of J774 incubated with MS (A); Scale bar 2  $\mu\text{m}$ . 3D rendering of Z-stacks acquired by confocal laser microscopy images of 2D C, incubated with MS at 72h, to identify the single particles internalized (B); Scale bars 5  $\mu\text{m}$ . Quantification of the average number of particles/cell (C) and fold increase in cellular volume, at 72h, after internalization of MS (D).**

Internalization of MS in the scaffolds was assessed both with J774, and bone marrow-derived macrophages (BMDM). BMDM were isolated as previously described, and in accordance with institutional animal usage guidelines [27]. Briefly, after sacrificing BALB/c mice femurs were cleaned of surrounding tissues and cut at both ends. The cavity was flushed with complete media, using a 5 mL syringe and a 25-gauge needle. Bone marrow cells were mechanically separated into single-cell suspension, filtered and plated in media supplemented with macrophage colony-stimulating factor (10ng/ml).  $3 \cdot 10^5$  cells were seeded onto MS INT and MS ADS. Cells were deposited in a concentrated drop of 50  $\mu$ l on top of the dry scaffolds and let adhere for 20 minutes, before media (up to 2 ml) was added. In the 2D simplified MS ADS model, the same cell density used in the scaffold was maintained.

#### 5.2.4. Flow cytometry:

To quantify the percentage of cells (J774 and BMDM) internalizing MS at 24, 48 and 72h from seeding, scaffolds were digested with collagenase I (2mg/ml) (Life Technologies). Both cells and MS were recovered. Cell suspensions were filtered through 70  $\mu$ m nylon mesh (BD Biosciences) to remove cell clumps and scaffold debris, and spun at 500 g for 5 min. Supernatants were removed and cell/particles pellets re-suspended in 1 mL of 70% EtOH. After fixation, cells were washed with FACS buffer (BSA 0.1%). Cells were stained with F4/80 antibody conjugated with Alexa Fluor®488, according to vendor's protocol (BioLegend) and resuspended in PBS. TRIC-labeled MS were used for this experiment. A minimum of 10,000 events per sample was analyzed using a BD LSR Fortessa™ cell analyzer (BD Biosciences, San Jose, CA). Data analysis was performed by FCS-Express (De Novo Software).

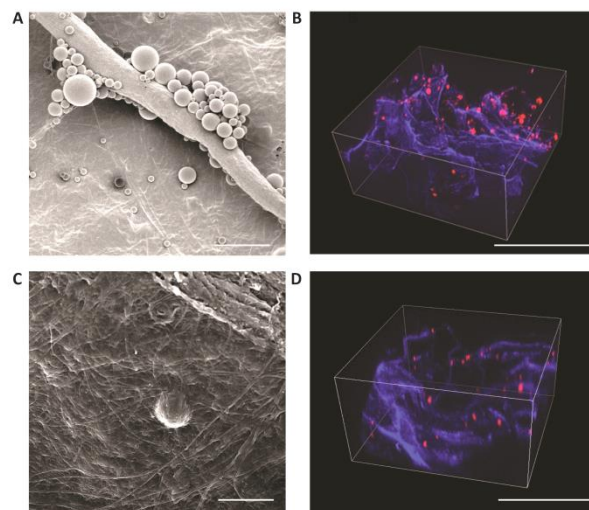


**Figure 5.3 - SEM micrograph and 3D rendering of Z-stacks by confocal laser microscopy of MS ADS (A, B), compared to MS INT (C, D); Scale bars 5  $\mu$ m and 100  $\mu$ m respectively.**

#### 5.2.5. Evaluation of the release kinetics from exposed and camouflaged MS:

The release of the reporter protein FITC-BSA from MS, MS ADS, MS INT and MS INT seeded with macrophages J774 was assessed to evaluate whether the eventual internalization by macrophages would affect the release kinetics. The release was followed, as a proof of concept, up to 1 week. FITC-BSA release was quantified via Plate Reader (Perkin Elmer) at a wavelength of 488 nm. For the recovery of MS internalized by J774, cells were lysed by adding deionized water and freezing, to not affect MS and their payload [28].

#### 5.2.6. Statistical analysis:

Statistical analysis was performed using Tukey's multiple comparison test, with Graph Pad v6.02 for Windows. A value of  $p < 0.05$  was considered statistically significant: \*  $p < 0.05$ ; \*\*  $p < 0.01$ ; \*\*\*  $p < 0.001$ ; \*\*\*\*  $p < 0.0001$ . Experiments have been performed in, at least, triplicates. Data are presented showing individual groups and respective  $\pm$  SD.

### 5.3. Results:

#### 5.3.1. MS internalization in 2D culture:

MS were successfully prepared with an average diameter of  $2 \mu\text{m} \pm 0.38$ , and a Z potential of  $-8.04$  (mobility  $-0.8363$ ). Initially, MS internalization was assessed in 2D conditions. SEM images of MS with J774 macrophages at 24h, 48h and 72h show how MS are massively engulfed already after 24h (Fig. 5.2A). Z-stacks acquired by confocal laser microscopy allowed to count the number of MS internalized per single cell at 72h (when saturation occurred), respect to 2D C (Fig. 5.2B). 3D intensity surface plot were obtained post-acquisition, to verify the internalization of the target MS (Fig. 5.2b). It resulted that J774 cells internalized an average of  $9 (\pm 1.31)$  MS per cell (Fig. 5.2C). After 48h, the number of particles that have been internalized remained unvaried. No significant increase in toxicity was found. Cells internalizing MS appeared to duplicate in their volume, with an average fold increase of  $2.3 (\pm 0.13)$  respect to their control (Fig. 5.2D).

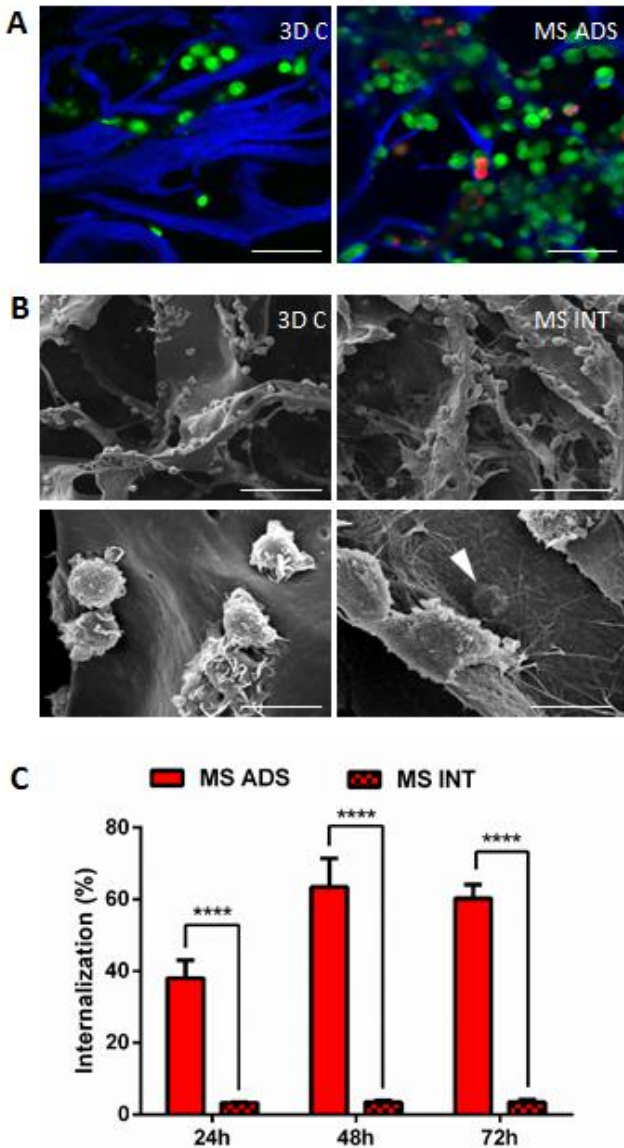


Figure 5.4 - Confocal laser microscopy images of 3D C and MS ADS scaffolds (A); scale bar 50  $\mu\text{m}$ . SEM micrographs of 3D C and MS INT (camouflaged MS indicated with white arrow) (B); scale bars 100 and 10  $\mu\text{m}$ . Percentage of cells internalizing MS in MS ADS and MS INT by flow cytometry (C).

#### 5.3.2. Biomimetic scaffold functionalization with camouflaged microspheres:

Scaffolds were optimized to be functionalized with approximately 10 MS/cell seeded. Fig. 5.3A shows a detail of the surface of MS ADS, in which MS are simply adsorbed and appear to be agglomerated. The 3D rendering obtained by confocal laser microscopy confirmed the observation (Fig. 5.3B). On the contrary, as shown in Fig. 5.3C the MS were fully integrated and homogeneously distributed in MS INT and were found in correspondence of the pore' walls of the scaffold (Fig. 5.3D).

#### 5.3.3. Evaluation of the internalization of camouflaged MS

MS internalization by macrophages in MS ADS was firstly evaluated by confocal laser microscopy. Fig. 5.4A shows the comparison between 3D C and MS ADS scaffold, in which J774 (green) appear to have identified the MS (red) adsorbed on the scaffold pores' walls (blue). On the contrary, MS INT were observed by SEM microscopy to better evaluate any change in J774's morphology and to identify eventual MS hidden within the collagen matrix of the scaffold. Fig. 5.4B shows the comparison between 3D C and MS INT at different magnifications. At low magnification cells in MS INT appeared spread throughout the whole field of view similarly to the control, whereas those seeded onto MS ADS clustered around the MS. As shown in Fig. 5.4A, the most exposed MS were internalized by macrophages, suggesting the ability of these cells to detect them. On the contrary, MS embedded into the scaffolds (indicated by white arrows) were not detected, as pore's walls are thicker than their diameter. These findings were further confirmed when the cut was cut transversally and the exposed MS were immediately identified by macrophages.

Internalization was then assessed by flow cytometry and we found that at 24h the percentage of FITC/TRIC positive J774 in MS INT was 10-times lower than their

control MS ADS. It became up to 15 times lower after 48h (Fig. 5.4C). SEM micrographs of MS INT BMDM showed no internalization (Fig. 5.5A) nor differences in cell morphology induced by their interaction with MS. BMDM appeared randomly distributed, similarly to the control group (3D C BMDM). Confocal laser microscopy further confirmed these observations. Images show cells attached to the surface of the collagen scaffold and MS lying underneath them (Fig. 5.5B). Interestingly, the percentage of cell that internalized MS correlated with that obtained with the J774 cell line. A 10-folds decrease in internalization between MS ADS and MS INT was observed also with this cell line (Fig. 5.5C).

#### 5.3.4. Pro-inflammatory cytokine production:

We further evaluated whether the collagen coating to avoid macrophage detection could also reduce the levels of some key pro-inflammatory cytokines (NO and TNF- $\alpha$ ). Interestingly, the production of NO was found increased of one-fold when MS were not camouflaged (MS ADS) (Fig. 5.6A). In MS ADS, NO production reached its maximum at 48h ( $15.7 \pm 2.01 \mu\text{M}$ ), correlating with data obtained by flow cytometry, as J774 resulted to reach the maximum of MS internalization at the same time point. On the contrary, in MS INT NO levels were comparable to the control values ( $9.7 \pm 0.71$  and  $10.7 \pm 0.91 \mu\text{M}$  respectively) (Fig. 5.6A). At 72h, the levels of TNF- $\alpha$  released by macrophages following the exposure to MS ADS were found significantly increased (3 and 2.5 fold, respectively) compared to their controls.

Finally, after assessing the validity of our approach with J774 and to further validate the model in 3D, we tested the efficiency of MS INT to reduce macrophage detection of MS also with BMDM (Fig. 5.6B). Exposure of BMDM to the scaffolds did not show significant differences in the levels of cytokines produced when compared to J774 cells or to their controls (3D C BMDM).

#### 5.3.5. Effect of MS camouflage on the release kinetics of a reporter protein:

To test whether MS INT could preserve the release kinetics of the payload respect to MS ADS the release of a reported protein (FITC-BSA) loaded in MS was monitored up to a week. The ratio cell/microspheres was optimized at 1:10 in all the experimental conditions, to be able to compare the cumulative releases obtained in the different conditions. At day 7 the cumulative release from MS INT resulted 45%, about half than that of MS ADS (100%) (Fig. 5.7A). MS INT and MS INT seeded with J774 (MS INT J774) showed comparable cumulative release and kinetics over time (45% and 41% respectively at 7 days). While from MS ADS seeded with J774 (MS ADS J774) only 16% of the protein was released, corresponding to a 6 fold decrease respect to MS ADS (Fig. 5.7A). We further characterized that at day 7 in MS ADS J774 70% of the FITC BSA was found in the fraction of the macrophages, whereas only 5% of the protein was internalized by the cells in MS INT J774 (Fig. 5.7B). Interestingly, in MS ADS only the 14% of MS were not internalized at 7 days, and this number was approximately 4-times increase in MS INT (54%).

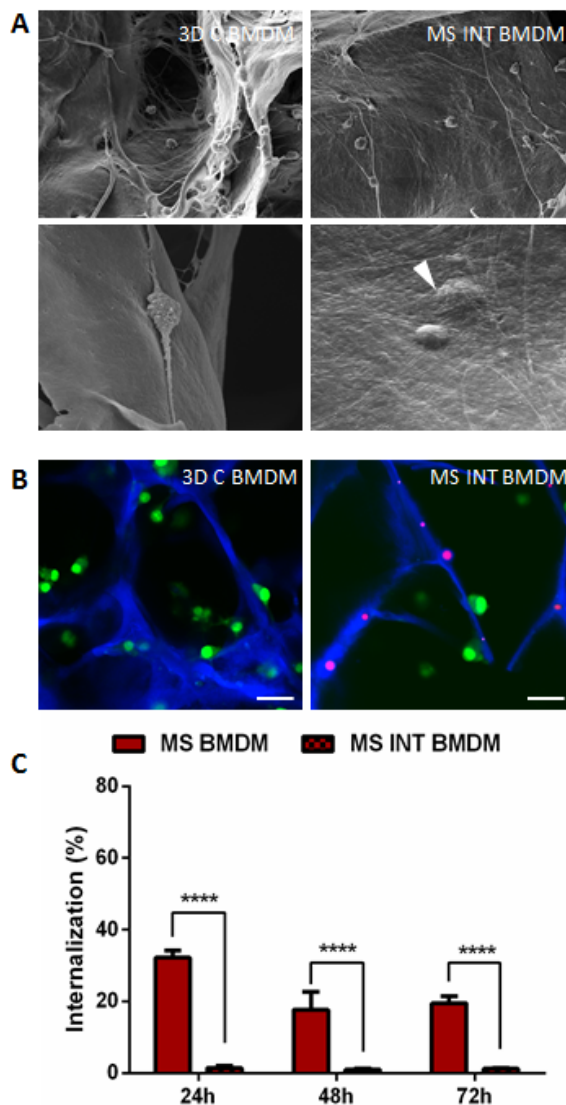


Figure 5.3 - SEM images of MS INT seeded with BMDM (A); Scale bar 20 and 10  $\mu\text{m}$ . Confocal laser microscopy images of 3D C BMDM and MS INT BMDM (B); scale bar 10 $\mu\text{m}$ . Percentage of BMDM internalizing MS in MS ADS BMDM and MS INT BMDM, quantified by flow cytometry.

## 5.4. Discussion:

The ideal scaffold to achieve tissue regeneration should be able to mimic the chemical and biochemical composition of the extracellular environment [29], to support cell recruitment, proliferation and differentiation [30]. Biomimetic scaffolds engineered with reservoirs of growth factors, chemokines or cytokines represent a promising strategy, and a plethora of delivery systems is now available for the storage and release of such proteins

[31]. However, platforms able to overcome the clearance mediated by macrophages are crucial to ensure proper release kinetics of the bioactive molecules and guarantee the desired therapeutic effects [32]. In fact, since growth factors explicit their function in the extracellular environment, the internalization of the delivery systems mediated by the macrophages is responsible for the disruption of their functional mechanisms [33].

In this study, we investigated whether camouflaging MS into a 3D collagen-based scaffold could offer an efficient method to prevent their internalization by macrophages and their consequent clearance from the implant.

MS internalization by macrophages has been shown to depend on several physicochemical properties, such as size, charge and shape [19, 26]. For example, MS with diameter below 5  $\mu\text{m}$  are known to be easily internalized by these cells [34]. Thus, as a prove of concept we tested MS with a diameter of  $2 \mu\text{m} \pm 0.38$ , and recapitulated in *in vitro* conditions the process of clearance occurring *in vivo*. Firstly, by using different

concentrations of MS, we evaluated the maximum number of MS which could be internalized per J774. No significant differences were found neither in cell viability at increasing concentrations of MS, nor in the number of MS internalized, confirming previously published data [35, 36]. Each cell was able to internalize an average of 9 MS. For this reason scaffolds were functionalized with approximately 10 MS per cell seeded, to potentially allow for the cells to clear all of them out from the scaffolds.

To assess the validity of our approach, we initially analyzed the morphology of the J774 seeded onto MS INT and MS ADS and we found a cell cluster in MS ADS, which was mainly due to the presence of agglomerated MS on the surface of the scaffolds. This observation was further confirmed by the confocal microscopy images, which show the perfect co-localization of the clusters of MS (red) and J774 (green). These findings enforced our hypothesis that the collagen layer covering MS in MS INT could screen them, resulting in a more homogeneous cell distribution, comparable to that of 3D C. Flow cytometry quantitatively confirmed these results revealing a 10 to 15 fold decrease in MS internalization in MS INT respect to MS ADS. Further corroborating these data, the uptake of MS by J774 from MS INT remained constant over time (2.5%) and not significantly differing from the control (MS ADS), while in MS ADS a burst MS uptake was quantified. This is particularly remarkable as it demonstrates the ability of the MS INT scaffold to camouflage MS for the window of time in which macrophages normally respond to the implant *in vivo* [37]. It is conceivable that macrophages did not detect the delivery systems when camouflaged in the scaffold, as they were just able to sense collagen's chemical composition and topography, which is recognized as a component of the ECM.

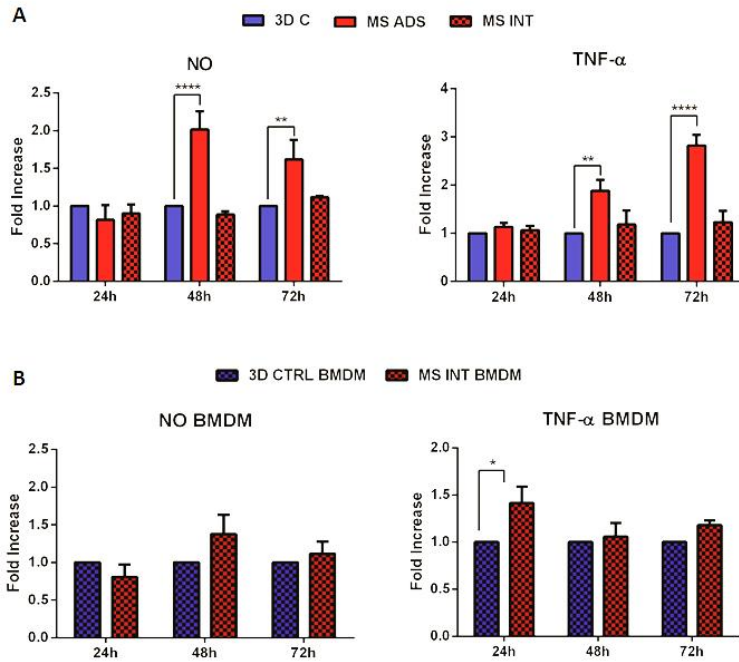


**Figure 5.4 - Production of NO and TNF- $\alpha$  by J774 macrophages in response to MS ADS and MS INT respect to their control (3D C) up to 72h (A); NO and TNF- $\alpha$  production by BMDM on MS INT respect to the control, up to 72h (B).**

In the biomedical research field, primary cell lines remain the cells of election for the *in vitro* test of any material or technology, as they present unique features which are inevitably lost in immortalized cells. Although J774 display differences in behavior with respect to the native cell type, they represent a valuable tool for *in vitro* study of cell-material interfaces of this study. For these reasons the first part of our study was conducted with J774 macrophages.

Since tissue resident macrophages have been recently found to be the one responsible for the response to implants [38, 39], we confirmed our findings with BMDM. The use of this cell type allowed us to closely recapitulate, in *in vitro* conditions, the *in vivo* response of macrophages to our MS INT scaffold. Interestingly, a slightly lower phagocytic activity was observed in BMDM respect to J774. This is possibly due to the intrinsic differences

between the two cell lines, including their size. In fact, analyzing the Z-stack acquisitions of single J774 and BMDM by confocal microscopy, BMDM resulted 15% smaller than J774 in volume (data not shown). This might explain the reduced number of MS that BMDM could internalize. In addition to this it is possible that this phenomenon reflects the different nature of the two cell lines (the immortalized J774 and the primary BMDM) [40], thus affecting their phagocytic activity [41].

An important consequence of MS internalization by macrophages is the triggering of the inflammatory cascade, which involves production of pro-inflammatory cytokines and can lead to implants' failure [32]. However, the new paradigm based on the anti-inflammatory role of macrophages [42] also highlighted the relevance of macrophage response to biomaterials to initiate the remodeling of the scaffold, ultimately leading to tissue repair [5]. Therefore, we evaluated the potential of this camouflaging approach to diminish the production of pro-inflammatory cytokines by macrophages following the interaction with the scaffold. In particular, among the pro-inflammatory molecules, we selected NO and TNF- $\alpha$  that are important drivers of fibrosis, being involved in fibroblast proliferation and collagen deposition [43]. Data obtained supported our hypothesis, as the camouflage of MS by the scaffold prevented the release of pro-inflammatory molecules by both the cell lines.

To finally prove the validity of our approach, we followed the release of a reporter protein (FITC-BSA) over a week, to understand whether the release kinetics was maintained or affected by macrophages.

According to our previous findings, the secondary coating created by the collagen matrix on the MS, became a further level of control over the release of proteins, allowing for a zero-order release kinetic [14]. Instead, due to the massive initial burst release in MS ADS, FITC-BSA was completely released within a week. When MS ADS were exposed to J774, the overall release at 7 days drastically decreased possibly due to the fact that MS were up-taken by the cells. On the contrary, the release from MS INT with or without J774 showed comparable kinetics.

In summary, this study demonstrated the potential of our platform to prevent the clearance mediated by macrophages of proteins or drugs' reservoirs from a 3D biomimetic scaffold, while reducing the production of key pro-inflammatory cytokines.

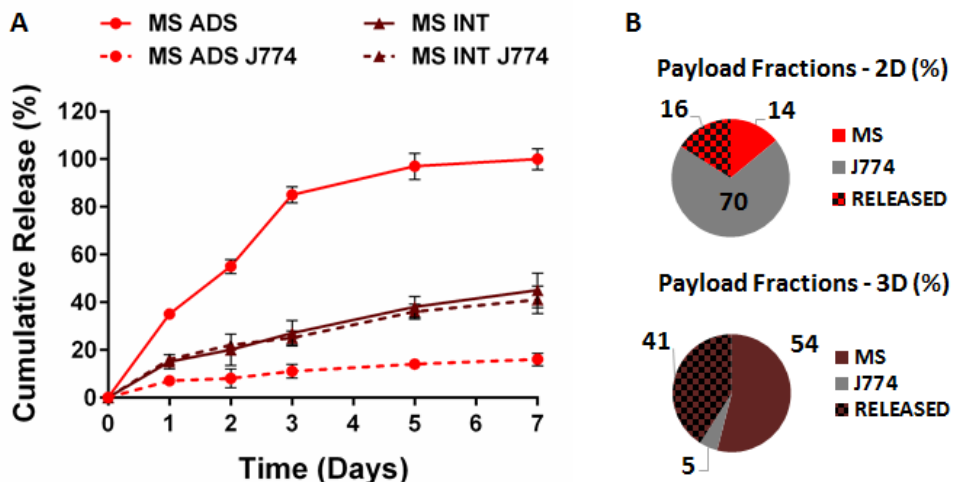


Figure 5.5 - Cumulative release of BSA up to 1 week, from MS ADS, MS INT, compared to the corresponding samples incubated with J774 macrophages (MS ADS J774 AND MS INT J774 respectively) (A); corresponding quantifications of BSA in the particles not internalized (MS), found inside macrophages (J774) or Released for MS ADS J774 and MS INT J774 samples (B).

### **5.5. Conclusions:**

In the present study we evaluated whether the integration of MS in type I collagen scaffold could provide an efficient and simple method for particle camouflage to prevent their internalization by macrophages and consequently reduce the production of pro-inflammatory cytokines, and to preserve the release kinetics of the payload. Herein, we provide striking evidences regarding the potential of this platform to: (i) escape the internalization by macrophages, (ii) enable the reduction of pro-inflammatory cytokines production by macrophages, and (iii) preserve the expected release kinetics engineered with the delivery platform. The reported findings can guide the rational design of functionalized scaffolds achieving the desired level of internalization of MS by immune cells. This study could significantly impact tissue engineering approaches, in which a tightly controlled confinement of the bioactive molecules is required, to achieve tissue healing without triggering the inflammatory response.

## 5.6. References:

1. Franz, S., et al., *Immune responses to implants – A review of the implications for the design of immunomodulatory biomaterials*. Biomaterials, 2011. **32**(28): p. 6692-6709.
2. Mitragotri, S. and J. Lahann, *Physical approaches to biomaterial design*. Nature materials, 2009. **8**(1): p. 15-23.
3. Valentin, J.E., et al., *Extracellular matrix bioscaffolds for orthopaedic applications A comparative histologic study*. The Journal of Bone & Joint Surgery, 2006. **88**(12): p. 2673-2686.
4. Brown, B.N., et al., *Macrophage phenotype as a predictor of constructive remodeling following the implantation of biologically derived surgical mesh materials*. Acta Biomaterialia, 2012. **8**(3): p. 978-987.
5. Brown, B.N., et al., *Macrophage polarization: an opportunity for improved outcomes in biomaterials and regenerative medicine*. Biomaterials, 2012. **33**(15): p. 3792-3802.
6. Mantovani, A., et al., *Macrophage plasticity and polarization in tissue repair and remodelling*. The Journal of pathology, 2013. **229**(2): p. 176-185.
7. Badylak, S.F., et al., *Macrophage phenotype as a determinant of biologic scaffold remodeling*. Tissue Engineering Part A, 2008. **14**(11): p. 1835-1842.
8. Pierschbacher, M.D., E.G. Hayman, and E. Ruoslahti, *Location of the cell-attachment site in fibronectin with monoclonal antibodies and proteolytic fragments of the molecule*. Cell, 1981. **26**(2): p. 259-267.
9. Graf, J., et al., *Identification of an amino acid sequence in laminin mediating cell attachment, chemotaxis, and receptor binding*. Cell, 1987. **48**(6): p. 989-996.
10. Badylak, S.F., D.O. Freytes, and T.W. Gilbert, *Extracellular matrix as a biological scaffold material: structure and function*. Acta biomaterialia, 2009. **5**(1): p. 1-13.
11. Brown, B.N. and S.F. Badylak, *Extracellular matrix as an inductive scaffold for functional tissue reconstruction*. Translational Research. **163**(4): p. 268-285.
12. Lu, H., et al., *Spatial immobilization of bone morphogenetic protein-4 in a collagen-PLGA hybrid scaffold for enhanced osteoinductivity*. Biomaterials, 2012. **33**(26): p. 6140-6146.
13. Tan, H., et al., *Gelatin/chitosan/hyaluronan scaffold integrated with PLGA microspheres for cartilage tissue engineering*. Acta Biomaterialia, 2009. **5**(1): p. 328-337.
14. Minardi, S., et al., *Multiscale Patterning of a Biomimetic Scaffold Integrated with Composite Microspheres*. Small, 2014.
15. Borselli, C., et al., *Bioactivation of collagen matrices through sustained VEGF release from PLGA microspheres*. Journal of Biomedical Materials Research Part A, 2010. **92**(1): p. 94-102.
16. Champion, J.A. and S. Mitragotri, *Shape induced inhibition of phagocytosis of polymer particles*. Pharmaceutical research, 2009. **26**(1): p. 244-249.
17. Anderson, J.M. and M.S. Shive, *Biodegradation and biocompatibility of PLA and PLGA microspheres*. Advanced Drug Delivery Reviews, 2012. **64**, **Supplement**(0): p. 72-82.
18. Doshi, N. and S. Mitragotri, *Macrophages recognize size and shape of their targets*. PLoS One, 2010. **5**(4): p. e10051.
19. Sharma, G., et al., *Polymer particle shape independently influences binding and internalization by macrophages*. Journal of controlled release, 2010. **147**(3): p. 408-412.
20. Best, J.P., Y. Yan, and F. Caruso, *The Role of Particle Geometry and Mechanics in the Biological Domain*. Advanced healthcare materials, 2012. **1**(1): p. 35-47.
21. Yue, H., et al., *Particle size affects the cellular response in macrophages*. European Journal of Pharmaceutical Sciences, 2010. **41**(5): p. 650-657.
22. Dhar, S., et al., *Targeted delivery of cisplatin to prostate cancer cells by aptamer functionalized Pt (IV) prodrug-PLGA-PEG nanoparticles*. Proceedings of the National Academy of Sciences, 2008. **105**(45): p. 17356-17361.
23. Freitas, S., H.P. Merkle, and B. Gander, *Microencapsulation by solvent extraction/evaporation: reviewing the state of the art of microsphere preparation process technology*. Journal of controlled release, 2005. **102**(2): p. 313-332.
24. Yang, Y.-Y., T.-S. Chung, and N. Ping Ng, *Morphology, drug distribution, and in vitro release profiles of biodegradable polymeric microspheres containing protein fabricated by double-emulsion solvent extraction/evaporation method*. Biomaterials, 2001. **22**(3): p. 231-241.
25. Young, S., et al., *Gelatin as a delivery vehicle for the controlled release of bioactive molecules*. Journal of controlled release, 2005. **109**(1-3): p. 256-274.

26. Natarajan, V., P. Saravanakumar, and B. Madhan, *Collagen adsorption on quercetin loaded polycaprolactone microspheres: Approach for "stealth" implant*. International Journal of Biological Macromolecules, 2012. **50**(4): p. 1091-1094.
27. Weischenfeldt, J. and B. Porse, *Bone marrow-derived macrophages (BMM): isolation and applications*. Cold Spring Harbor Protocols, 2008. **2008**(12): p. pdb. prot5080.
28. Rage, R., J. Mitchen, and G. Wilding, *DNA fluorometric assay in 96-well tissue culture plates using Hoechst 33258 after cell lysis by freezing in distilled water*. Analytical biochemistry, 1990. **191**(1): p. 31-34.
29. Bose, S., M. Roy, and A. Bandyopadhyay, *Recent advances in bone tissue engineering scaffolds*. Trends in biotechnology, 2012. **30**(10): p. 546-554.
30. O'Brien, F.J., *Biomaterials & scaffolds for tissue engineering*. Materials Today, 2011. **14**(3): p. 88-95.
31. Chen, F.-M., M. Zhang, and Z.-F. Wu, *Toward delivery of multiple growth factors in tissue engineering*. Biomaterials, 2010. **31**(24): p. 6279-6308.
32. Taraballi, F., et al., *Potential Avoidance of Adverse Analgesic Effects Using a Biologically "Smart" Hydrogel Capable of Controlled Bupivacaine Release*. Journal of pharmaceutical sciences, 2014.
33. Kolambkar, Y.M., et al., *An alginate-based hybrid system for growth factor delivery in the functional repair of large bone defects*. Biomaterials, 2011. **32**(1): p. 65-74.
34. Champion, J.A., A. Walker, and S. Mitragotri, *Role of particle size in phagocytosis of polymeric microspheres*. Pharmaceutical research, 2008. **25**(8): p. 1815-1821.
35. Hirota, K., et al., *Optimum conditions for efficient phagocytosis of rifampicin-loaded PLGA microspheres by alveolar macrophages*. Journal of controlled release, 2007. **119**(1): p. 69-76.
36. Walter, E., et al., *Hydrophilic poly(dl-lactide-co-glycolide) microspheres for the delivery of DNA to human-derived macrophages and dendritic cells*. Journal of controlled release, 2001. **76**(1-2): p. 149-168.
37. van Putten, S.M., et al., *Macrophage phenotypes in the collagen-induced foreign body reaction in rats*. Acta biomaterialia, 2013. **9**(5): p. 6502-6510.
38. Davies, L.C., et al., *Tissue-resident macrophages*. Nature immunology, 2013. **14**(10): p. 986-995.
39. Hashimoto, D., et al., *Tissue-Resident Macrophages Self-Maintain Locally throughout Adult Life with Minimal Contribution from Circulating Monocytes*. Immunity, 2013. **38**(4): p. 792-804.
40. Ralph P, N.I., *Phagocytosis and cytolysis by a macrophage tumor and its cloned cell line*. . Nature immunology, 1975: p. 257: 393-394.
41. O'Riordan, M., et al., *Innate recognition of bacteria by a macrophage cytosolic surveillance pathway*. Proceedings of the National Academy of Sciences, 2002. **99**(21): p. 13861-13866.
42. Lawrence, T. and G. Natoli, *Transcriptional regulation of macrophage polarization: enabling diversity with identity*. Nature reviews immunology, 2011. **11**(11): p. 750-761.
43. Medzhitov, R., *Inflammation 2010: new adventures of an old flame*. Cell, 2010. **140**(6): p. 771-6.

# CONCLUSIONS

In summary, firstly, the nanostructured composite microspheres PLGA-pSi were developed. Their full tunability was demonstrated. This kind of composite carrier combined the advantages of mesoporous structures to be loaded with high amount of proteins, due to their high surface area, and the plasticity and tailorability of polymers. As a proof of concept, the formulation which accomplished the most controlled and sustained release was tested *in vivo*, to demonstrate the temporal and spatial control over the release of the payload. However, depending on the application, it is possible to envision the use of other formulations, and also the combined use of multiple formulations of PLGA-pSi. They also resulted greatly advantageous by being injectable, which would allow for an easy administration of a molecule of interest, once a month, while showing low toxicity. These results assessed *in vivo* that PLGA-pSi represents a robust, reproducible and scalable carrier for applications of tissue regeneration.

Secondly, a novel approach for the creation of multiscale biomimetic scaffold, capable of generating spatial and temporal protein patterns was designed. The result was achieved by leveraging the natural ability of the collagen matrix to interact with PLGA-pSi microspheres, effectively constructing a simple and tunable system for various tissue engineering applications. Optimizing the synthesis of monolithic multilayered collagen scaffolds, we stably integrated PLGA-pSi within the collagen matrix without altering collagen's nano- and microstructure. The results demonstrated that this modular approach to fabricate multi-compartment scaffolds allow tissue mimicry at a multiscale level. At the nanoscale, the type I collagen conserved its fibrillar structure and typical D-bands appearance, while the pSi nanostructure allowed the loading and release of reporter proteins. At the microscale, the PLGA coating of pSi created a composite delivery platform for the tunable release of the reporter proteins, while the collagen coating on PLGA-pSi enabled for their spatial confinement in the scaffold. Finally, at the macroscale, all these elements combined, without altering the feature of the material, such as pore size, porosity and swelling upon PLGA-pSi integration. pSi, PLGA and collagen contributed to accomplishing the temporal patterning of the proteins in the multi-layered scaffold, through a triple controlled release, enabling for zero-order release kinetics of reporter proteins up to 50 days. The release of controlled amounts of drugs over long periods of time would favor on-scaffold regeneration while avoiding adverse effects due to the diffusion of high doses of therapeutic molecules in the tissues surrounding the scaffold. By grafting distinct sets of PLGA-pSi composites, one can envision the creation of multiple unique biochemical niches within a 3D biomimetic scaffold, while protecting the payload and the delivery system from the cellular and enzymatic attack and from the surgical procedures (washing, debridement, bleeding, fluid aspiration) applied during the implantation of the scaffold which challenge the integrity of the material.

Lastly, it was investigated whether the integration of PLGA-pSi microspheres in type I collagen scaffold could provide an efficient and simple method for particle camouflage to prevent their internalization by macrophages and consequently reduce the production of pro-inflammatory cytokines, and to preserve the release kinetics of the payload. It was provided striking evidences regarding the potential of this platform to: (i) escape internalization by macrophages, (ii) enable the reduction of pro-inflammatory cytokine production by macrophages, and (iii) preserve the expected release kinetics engineered with the delivery platform. The reported findings can guide the rational design of functionalized scaffolds achieving the desired level of internalization of PLGA-pSi microspheres by immune cells.

All together, this study could significantly impact tissue engineering approaches, in which a tightly controlled confinement of the bioactive molecules is required, to achieve tissue healing without triggering the inflammatory response.

